UNIVERSITY OF CALIFORNIA, SAN DIEGO

Multi-wavelength Analysis of Active Galactic Nuclei and Host Galaxies Physical Properties

A dissertation submitted in partial satisfaction of the
requirements for the degree of Doctor of Philosophy

in

Physics

by

Mojegan Azadi

Committee in charge:

Professor Alison Coil, Chair
Professor William Coles
Professor Dusan Keres
Professor Jeremie Palacci
Professor Shelley Wright

2017

The Dissertation of Mojegan Azadi is approved and is acceptable in quality and form for publication on microfilm and electronically:

Chair

University of California, San Diego

2017

DEDICATION

To
my husband for his love and support,
my mom for her selfless affection and dedication,
and
my dad for encouraging me to pursue my dreams.

EPIGRAPH

The stars that dwell on celestial vault
are to spark the path of wisdom,
Take heed and don't lose the source of wisdom,
or you will be an aimless wanderer who goes astray.

Omar Khayyam

TABLE OF CONTENTS

LIST OF FIGURES

LIST OF TABLES

ACKNOWLEDGEMENTS

First, I would like to express my deep gratitude to my advisor, Alison Coil for her help and guidance throughout my graduate studies. Alison is a brilliant scientist and a dedicated leader for her research group. Her technical and editorial advice was essential to the completion of this dissertation and has taught me innumerable lessons. Also I would like to thank James Aird for all the insightful discussions about my research projects. James has been a patient and approachable mentor and an outstanding role model who has inspired me to be a better scientist. I am also grateful for the advice, cooperation and teamwork of the former and current members of our research group, Ramin Skibba, Brooke Simmons, Aleks Diamond-Stanic, Alexander Mendez, and Gene Leung. I would like to extend my appreciation to the members of my thesis committee, William Coles, Dusan Keres, Jeremie Palacci and Shelley Wright for their feedback on my research projects and reading of this dissertation.

Chapter 2, in full, is a reprint of the material as it appears in The Astrophysical Journal 2015. Azadi, M., Aird, J., Coil, A., Moustakas J., Mendez, A., Blanton, M., Cool, R., Eisenstein, D., Wong, K., Zhu G. 2015. The dissertation author was the primary investigator and author of this paper.

Chapter 3, in full, is a reprint of the material as it appears in The Astrophysical Journal 2017. Azadi, M., Coil, A., Aird, J., Reddy, N., Shapley, A., Freeman, W., Kriek, M., Leung, GCK., Mobasher, B., Price, S., Sanders, R., Shivaei, I., Siana, B. 2017. The dissertation author was the primary investigator and author of this paper.

Chapter 4 is a draft of material that will be submitted to The Astrophysical Journal, Azadi, M., Coil, A., Aird, J., Reddy, N., Shivaei, I., Shapley, A., Freeman, W., Kriek, M., Leung, GCK., Mobasher, B., Price, S., Sanders, R., Siana, B., Zick, T. 2017. The dissertation author is the primary investigator and author of this paper.

VITA

2006	Bachelor of Science, Khajeh Nassir Toosi University of Technology, Iran
2010	Master of Science, University of Tehran, Iran
2017	Doctor of Philosophy, University of California, San Diego

PUBLICATIONS

"The MOSDEF survey: The nature of Mid-infrared excess galaxies at z 2 "Azadi, M., Coil, A., Aird, J., Reddy, N., Shivaei, I., Shapley, A., Freeman, W., Kriek, M., Leung, GCK., Mobasher, B., Price, S., Sanders, R., Siana, B.,Zick, T. 2017, in prep

"The MOSDEF survey: AGN multi-wavelength identification, selection biases and host galaxy properties"Azadi, M., Coil, A., Aird, J., Reddy, N., Shapley, A., Freeman, W., Kriek, M., Leung, GCK., Mobasher, B., Price, S., Sanders, R., Shivaei, I., Siana, B., 2017, ApJ, 835,27

"PRIMUS: The relationship between Star formation and AGN accretion" Azadi, M., Aird, J., Coil, A., Moustakas J., Mendez, A., Blanton, M., Cool, R., Eisenstein, D., Wong, K., Zhu G., 2015, ApJ 806.187

"The MOSDEF survey: The prevalence and properties of galaxy-wide AGN-driven outflows at $z \sim 2$" Leung, GCK, Coil, A., Azadi, M., Aird, J., Shapley, A., Kriek, M. , Mobasher, B., Reddy, N., Siana, B. , Freeman, W., Price, S., Sanders, R., Shivaei, I., arXiv:1703.10255

"The MOSFIRE Deep Evolution Field (MOSDEF) Survey: Rest-Frame optical spectroscopy for 1500 H-selected galaxies at $1.37 < z < 3.8$" Kriek, M., Shapley, A., Reddy, N., Siana, B., Coil, A., Mobasher, B., Freeman, W., de Groot, L., Price, S., Sanders, R., Shivaei, I., Brammer, G., Momcheva, I., Skelton, R., van Dokkum, P., Whitaker, K., Aird, J., Azadi, M., Kassis, M., Bullock, J., Conroy, C., Dav,R., Keres, D., Krumholz, M., 2015, ApJS, 218, 15

"The MOSDEF Survey: Dynamical and baryonic masses and kinematic structures of star-forming galaxies at $1.4 \leq z \leq 2.6$" Price,S., Kriek,M., Shapley,A., Reddy,N., Freeman,W., Coil,A., deGroot,L., Shivaei,I., Siana,B., Azadi,M., Barro, G., Mobasher, B., Sanders, R., Zick, T., 2016, ApJ, 819, 80

"The MOSDEF Survey: Dissecting the star formation rate versus stellar mass relation using $H\alpha$ and $H\beta$ emission lines at $z \sim 2$" Shivaei,I., Reddy,N., Shapley,A., Kriek,M.,

Siana,B., Mobasher,B., Coil,A., Freeman, W., Sanders,R., Price,S., de Groot, L, Azadi, M., 2015, ApJ,815, 98

ABSTRACT OF THE DISSERTATION

Multi-wavelength Analysis of Active Galactic Nuclei and Host Galaxies Physical Properties

by

Mojegan Azadi

Doctor of Philosophy in Physics

University of California, San Diego, 2017

Professor Alison Coil, Chair

In this dissertation we study the properties of active galactic nuclei (AGN), which are powered by the accretion activity of supermassive black holes residing at the centers of galaxies. While observations propose that growth of AGN and galaxies are globally tied, we investigate whether this connection exists in individual galaxies. We also investigate various AGN selection techniques and star formation rate (SFR) estimates using multi-wavelength data from *Chandra*, *Spitzer* and rest-frame optical spectra from the Keck telescope.

We find that combining multi-wavelength identification techniques provides a

more complete AGN sample, as each selection method suffers from selection biases. In particular, all selection techniques are biased against identifying AGN in lower mass galaxies. Once stellar mass selection biases are taken into account, we find that AGN reside in galaxies with similar physical properties (i.e., SFR) as inactive galaxies.

We find that while AGN are prevalent in both star-forming and quiescent galaxies, AGN of a given accretion rate are more likely to reside in star-forming galaxies. The probability of fueling an AGN does not strongly depend on SFR for a star-forming galaxy, though it decreases when star formation is shut down in quiescent galaxies. We also find no evidence for a strong correlation between SFR or stellar mass of the host galaxy and AGN luminosity. These results indicate that while both AGN and galaxy growth are reliant on the same fuel, enhanced star formation activity does not necessarily go hand-in-hand with increased AGN activity.

While the star formation activity of galaxies can be traced with various indicators, our investigations indicate that extrapolations from mid-infrared data using calibrations based on local galaxies overestimates SFRs at higher redshift. We show that a combination of mid-infrared and far-infrared data provide a more reliable SFR estimation than the mid-infrared data alone. We also find that the robustness of UV-based SFRs depends on the extinction correction method used. We find a relatively small fraction of $z \sim 2$ galaxies have SFRs from infrared observations that are elevated relative to other SFR tracers, and we do not find any contribution from AGN in this excess.

Chapter 1

Introduction

The Universe that we observe can be described in a cosmological framework. The standard model of cosmology is based on the cosmological principle according to which the Universe is spatially homogeneous and isotropic, and Einstein's theory of general relativity, which states that the structure of space-time in the Universe is determined from its mass distribution. However, this uniform and isotropic picture can not justify formation of the structures (e.g. galaxies). To address this and other fundamental problems in the standard picture of Big Bang cosmology the fundamental problems of the standard Big Bang cosmology, the inflation theory (Guth 1981; Linde 1982) was invoked. Since the Big Bang the Universe has been continuously expanding; the inflation theory proposes that between 10^{-33} to 10^{-32} seconds after after the Big Bang the Universe underwent an exponential expansion for 10^{-36} seconds which increased its size by a factor of 10^{26}.

This rapid expansion resulted in temperature fluctuations and perturbations that grew with time and created regions with higher densities. The gravity from dense regions pulled more matter and created larger over dense regions. Eventually, the density enhancements led to the formation of the first hydrogen nuclei, which by attracting electrons turned into the first neutral atoms a few minutes after the Big Bang. After that the Universe entered a critical period in its evolution known as the "Reionization Era"

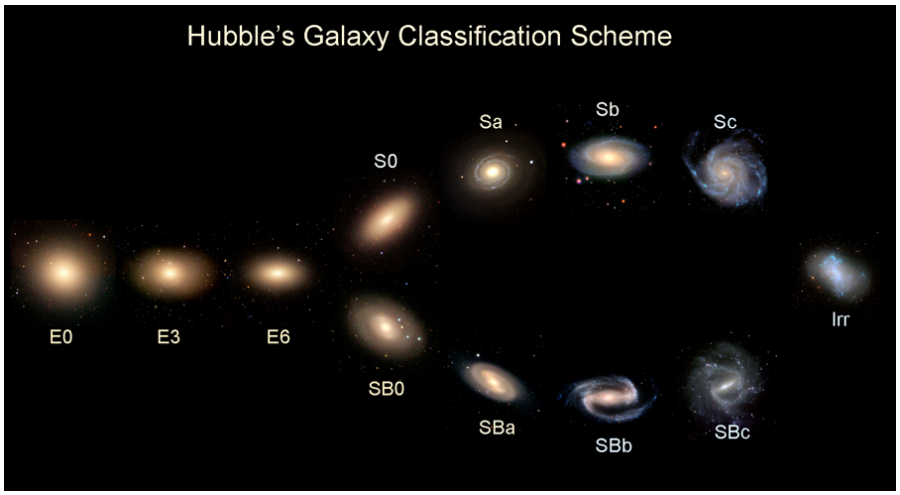

Figure 1.1. The Hubble sequence composed of the Sloan Digital Sky Survey images taken from the Galaxy Zoo project. According to Hubble's classification galaxies come in two main types of spirals and ellipticals; S0 objects are lenticular galaxies with intermediate properties of the two classes, and Irr are irregular galaxies that do not fit in either of the two types. Spirals also can be divided into subclasses with and without bars depending on the presence of an elongated narrow structure at their centers.

that lasted a few hundred million years. During this epoch, the first galaxies and stars were born within the halo-like structures of dark matter.

Our Universe is geometrically flat and is best described with ΛCDM model. In this framework, 68.3% of the Universe is made of dark energy (Λ, which is the cosmological constant in the theory of general relativity), and 26.8% is made of "cold" dark matter (CDM); the remaining 4.9% is the baryonic matter that includes the entire visible structure (e.g. galaxies and stars) in the Universe (Planck Collaboration et al. 2014).

The structure formation theories and observations favor a so-called "bottom-up" scenario in which low mass dark matter halos collapse due to their own gravitational attraction and create smaller clumps. The orbits of the small clumps decay due to their mutual gravity and dynamical friction until they merge and form larger dark matter halos. Galaxies form at the centers of dark matter halos. The interactions and mergers of

dark matter halos make their galaxies grow hierarchically (e.g. Rees & Ostriker 1977), and create galaxy groups with a few galaxies to galaxy clusters and super clusters with hundreds to thousands of galaxies. Galaxies interactions and mergers have substantial effects on their physical properties from changing galaxies structure and morphology to triggering bursts of star formation.

Galaxies are made of stars, gas and dust that are held together by gravity. The studies from the past two decades have established that almost all galaxies host a central massive black hole with $M_{BH} \sim 10^5 - 10^{10} M_{\odot}$ (Kormendy & Richstone 1995; Kormendy et al. 2011). As the observational data from the space-based and ground-based telescopes has been enhanced, investigating physics of supermassive black holes (SMBHs) has become the subject many recent studies (e.g. Hickox et al. 2009; Mullaney et al. 2012b; Cowley et al. 2016). In this dissertation we aim to use observational datasets at various wavelengths to identify active SMBHs in order to address fundamental questions such as what types of galaxies host active SMBHs, what physical mechanisms trigger SMBHs activity, and what impact do SMBHs have on their host galaxies?

1.1 Galaxies Classification and Properties

Galaxies are very diverse objects that can be characterized be a large number of parameters including their stellar population mass or age, size, morphology, color or nuclear activity. The environment that each galaxy lives in has an important influence on its physical properties, for instance a galaxy-galaxy interaction or merger causes a flow of gas and dust between the two components and disturbs their morphologies. In the 1930's Edward Hubble proposed a classification of galaxies according to their morphologies (Hubble & Humason 1931) that has been used by astronomers since then (for a recent review on galaxies morphology see Conselice 2014). In Hubble's classification as shown in Figure 1.1, galaxies are divided into two groups of spiral (or late-type) and ellipticals

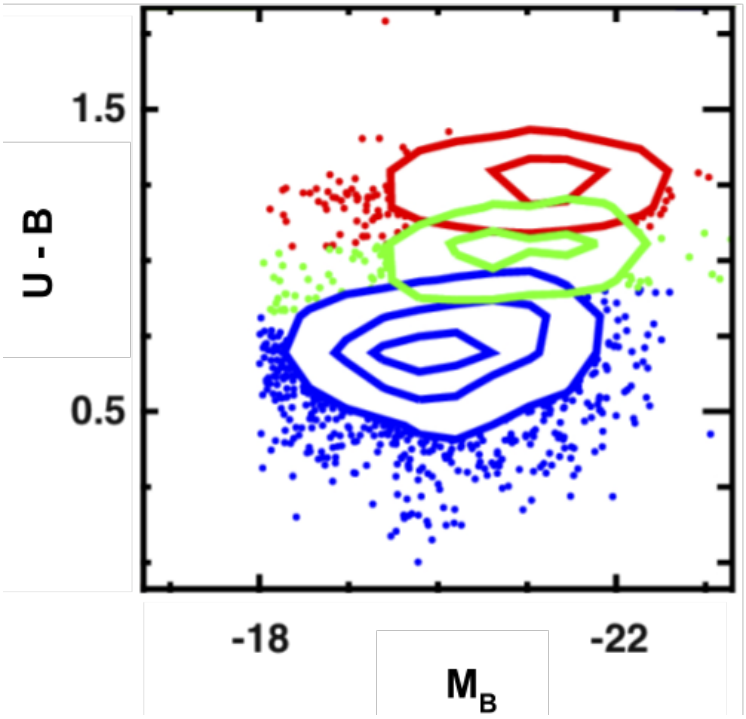

Figure 1.2. The (U-B) color versus magnitude in the B band; Galaxies occupy two distinct regions of the blue cloud (star-forming) and red sequence (quiescent) in this space. Galaxies that are in transition between two population reside in the green valley. The Figure is taken from Mendez et al. (2011) with permission.

(or early-type). The galaxies exhibiting features between these two classes are called lenticular galaxies, and those that can not be fitted in either of these classes are considered as irregular galaxies. The spiral galaxies have a flat rotating disk while ellipticals are round in shape and have random stellar orbits around the center. Hubble's sequence shows classes of galaxies from entirely bulge dominated galaxies to entirely disk dominated galaxies. However, most galaxies have a combination of a rotating disk with a spheroidal component.

The bimodal behavior of galaxies can be seen in their other characteristics as well. The rate at which galaxies form new stars is known as its star formation rate or SFR; studying galaxies in SFR-stellar population mass space shows that they fall into

two classes of star-forming galaxies with SFR as high as 100 $M_{\odot}/yr$ and beyond, and quiescent galaxies with very low or no star formation activity. Investigation of galaxies in color-magnitude space also reveals this bimodality. As shown in Figure 1.2, in the color-magnitude diagram galaxies are categorized as blue cloud consisting of young star-forming galaxies, and red sequence predominantly consisting of old quiescent galaxies (Bell et al. 2003; Blanton et al. 2003). There is also a third population know as the green valley that includes galaxies in transition between the two populations(e.g. Mendez et al. 2011). We note that the dust content of galaxies is an important factor in their location in the color-magnitude space, as young dust rich galaxies may exhibit green or red colors as well (Cardamone et al. 2010).

Altogether, observations indicate that galaxies transform from a disk dominated, young, star-forming population to a bulge dominated, old, quiescent population. It is critical to understand how these two populations come into existence and evolve with redshift. Although this bimodal behavior exist beyond the local Universe, about 10 billion years ago ($z \sim 2$) the number density of star-forming galaxies was higher than quiescent galaxies at all stellar masses (e.g. Whitaker et al. 2010). As the Universe aged, the number density of quiescent galaxies increased in a fashion that the majority of low-mass galaxies at $z \sim 1$ are star-forming while at high-mass end quiescent galaxies outnumber (Bundy et al. 2006). This trend continues until the current epoch where the quiescent population outnumbers the star-forming population at stellar masses above $\sim 10^{10} M_{\odot}$ (e.g. Bell et al. 2003; Baldry et al. 2004).

The rate at which star formation is quenched in galaxies varies with stellar mass and redshift (Moustakas et al. 2013). A wide variety of processes from intense star formation feedback in major-mergers to (e.g. Di-Matteo et al. 2005) to virial shock heating (Keres et al. 2005) have been proposed by studies as a determining factor in the quenching rate of galaxies. Many studies propose that the feedback from SMBHs can

determine the quenching rate of galaxies, since the energy released from the accretion activity of SMBHs can be high enough to push the gas outside the host galaxy and shut down the star formation activity (e.g. Page et al. 2012). However, SMBHs are also a diverse class of objects and their activity may not always produce strong feedback on the host galaxies (Leung et al. 2017). The impact of SMBHs' activity on the physical properties of their host galaxies is one of the main subjects that we aim to address in this dissertation.

1.2 Active Galactic Nuclei

Almost every galaxy hosts a supermassive black hole (SMBH; $10^5 < M_{BH} < 10^{10} M_{\odot}$) at its center (Kormendy & Richstone 1995). The SMBHs grow by consuming the nearby gas and dust that fall into the gravitational well of the black hole. It is not yet clear how exactly these massive objects are seeded in galaxies. Studies propose different scenarios such that they are remnants of the first generation (Pop III) of stars or that they form due to a collapse of primordial gas clouds or via collapse of stellar clusters. However, a single scenario can not provide a complete picture of SMBHs formation and each scenario could be limited to a specific mass or redshift (for more details on SMBHs formation see Volonteri 2010).

As the nearby mass moves towards the black hole it forms a rotating disk known as the accretion disk. The SMBHs and their accretion disks are surrounded by a dusty obscuring structure that geometrically depends on the central engine. The inner radius of the obscuring structure is determined by the sublimation temperature of the dust grains and its outer radius could be extended up to 1 pc. The compact central region of galaxies consisting of SMBHs, accretion disk and the obscuring structure is called "Active Galactic Nuclei" (AGN), and the galaxies hosting them are considered as active galaxies.

Recent studies find that AGN activity is an episodic phenomena and each galaxy may go through some periods of nuclear activity (Hickox et al. 2014). In order to understand AGN triggering, it is critical to know what physical mechanisms deliver gas from galactic scales ($\sim$ 10 kpc) down to the black holes' vicinity at $\sim$ 0.1 pc. In order for gas to fuel the SMBH it must lose angular momentum (Jogee 2006), and the dense gas cloud may collapse and form new stars before reaching to the nuclear regions.

The luminosity of AGN can be quantified by the rate at which it accretes nearby mass:

$$L = \varepsilon c^2 dM/dt \tag{1.1}$$

where M is the accreting mass and ε is the mass-energy efficiency conversion and is typically 0.1 (e.g. Hunt 2003); AGN bolometric luminosity (the luminosity over all wavelengths) usually varies between $10^{40} - 10^{46}$ erg/s. AGN activity can also be parametrized by the Eddington ratio (λ) shown below.

$$\lambda = \frac{L_{bol}}{L_{Edd}} \tag{1.2}$$

L_{Edd} is the bolometric luminosity, and L_{Edd} is the luminosity at the Eddington limit at which there is balance between the radiation pressure and the gravitational force

$$F_{grav} \sim \frac{4GM_{BH}m_p}{r^2} \tag{1.3}$$

$$F_{rad} = \frac{L_{Edd}\sigma_T}{4\pi r^2 c} \tag{1.4}$$

where G is the gravitational constant, m_p is the proton mass, and σ_T is the

Thompson scattering cross-section. Therefore the Eddington luminosity is

$$L_{Edd} = \frac{4\pi G M_{BH} m_p c}{\sigma_T} \tag{1.5}$$

Below in Section 1.2.1 we briefly review AGN classification. In order to categorize AGN it is important to know that in the geometry of AGN there are two distinct areas around the SMBHs: the immediate vicinity of the SMBH known as the Broad Line Region (BLR) where the physical extent depends on the central engine, and the region outside the obscuring structure known as the Narrow Line Region (NLR), which may be extended up to 1 kpc. The number density of electrons in the BLR is $\sim 10^8$ cm^{-3}, which is high enough to prevent a spontaneous decay of electrons to metastable energy levels and release of the forbidden emission lines (e.g. [O III] λ5008, [NII]λ6585). The velocity dispersion of the gas clouds in the BLR can be up to 10000 km s^{-1} (Osterbrock 1989; Netzer 1990). In the NLR the number density of the electron is $10^3 < n_e < 10^6$ cm^{-3}, which allows emission of both permitted and forbidden lines with the Doppler broadening less than 1000 km s^{-1} (e.g. Osterbrock 1989; Netzer 1990).

1.2.1 AGN Classification

AGN can be divided into various groups according to their geometry, type of feedback and the observer's viewing angle. By observing an AGN though a line of sight close to its polar axis one can detect the BLR and radiation from the immediate vicinity of the SMBH, while by observing through the equatorial plane of the obscuring structure only the NRL can be detected. In AGN classification according to the viewing angle, the first group are considered as Type 1 or unobscured AGN and the second group as Type 2 or obscured AGN. The standard Unified Theory of AGN (Antonucci 1993) states that Type 1 and 2 AGN have similar incidence rates in similar host galaxies, and their only difference is in the viewing angle. However, more recent studies are at odds with this

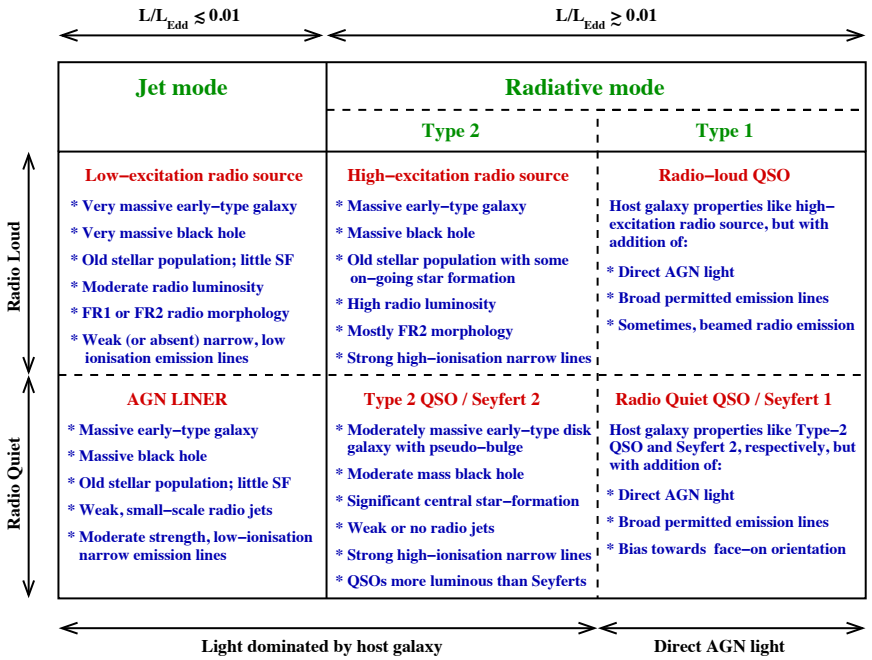

Figure 1.3. The AGN classification taken from Heckman & Best (2014). The AGN that we consider in this study are Type 2 Syfert/QSO.

standard picture and find that the host galaxies of Type 1 and 2 AGN exhibit different physical proprieties (Di-Matteo et al. 2005; Hopkins et al. 2008).

The nature of AGN feedback varies in different types of AGN. The radiative (or quasar) mode AGN release energy mainly in the form of electromagnetic radiation, while in jet (or radio) mode AGN the main output is through two-sided radio outflows called jets. Figure 1.3 presents a complete classification of AGN and their physical properties taken from Heckman & Best (2014). The AGN that we focus on in this dissertation are Type 2 Seyfert/QSO.

1.2.2 Multi-wavelength Analysis of AGN

AGN produce substantial radiation over a wide range of wavelengths; however the surrounding obscuring structure and the host galaxy block some of this radiation. Using multi-wavelength observations like putting pieces of puzzles together provide a

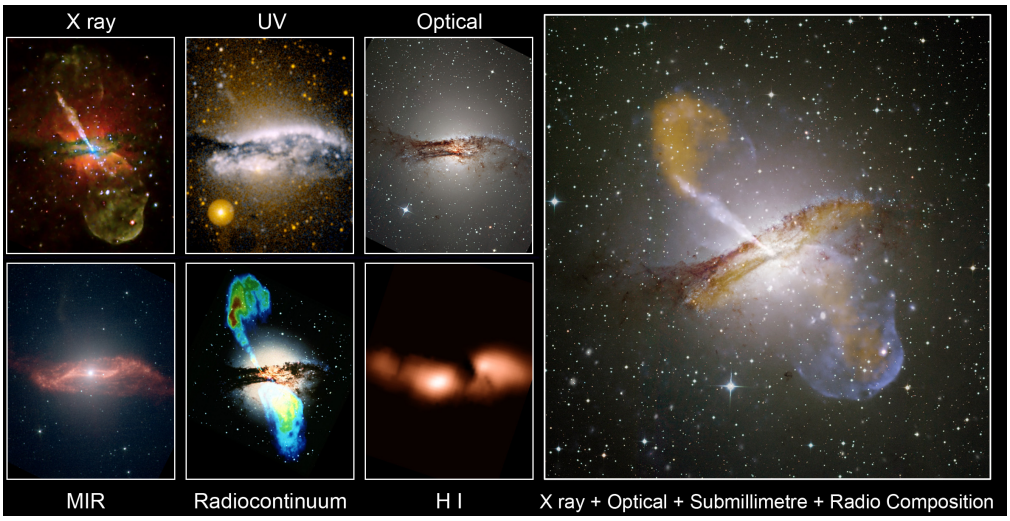

Figure 1.4. A multi-wavelength image of NGC 5128, which is a jet-mode radio-loud AGN living in the nearest giant elliptical galaxy to the Milky Way. This shows how we can benefit from a multi-wavelength analysis in studying AGN.

clearer picture of AGN physics. Figure 1.4 illustrates multi-wavelength images of NGC 5128 which is one of the best examples of a jet-mode radio-loud AGN. This figure clearly reveals how a single band observation could be insufficient in the analysis of AGN.

The radiative mode Type 2 AGN emit electromagnetic radiation from X-ray and UV to infrared wavelengths. The X-ray emission from AGN arises from the accretion disk and corona and is powerful enough to penetrate the obscuring structure (e.g. Brandt & Alexander 2015). However, the obscuring structure blocks the X-ray photons when the hydrogen column density (N_H) is higher than 1.5×10^{24} cm^{-2} (e.g. Alexander et al. 2011; Comastri et al. 2011). The images taken at UV and optical wavelengths are not always successful in AGN identification (see Figure 1.4 for instance). The dusty structure around the AGN absorbs the UV and optical continuum from the accretion disk, and the emission from the star formation activity of the host galaxies dominates at these wavelengths. The obscuring structure reprocesses the energy from the UV and optical photons and reradiate at mid-infrared wavelengths. AGN can also be distinguished from galaxies through their mid-infrared spectral shape and properties (e.g. Stern et al.

2005; Donley et al. 2012). In addition, the radiation from AGN can ionize the gas in the BLR and NLR regions which makes rest-frame optical spectroscopy a powerful method for AGN identification (e.g. Kauffmann et al. 2003a; Kauffmann & Heckman 2009a, also see Section 1.3). However, each of these identification methods suffers from incompletenesses and selection biases(e.g. Mendez et al. 2013; Ellison et al. 2016). In this dissertation we investigate the physical properties of AGN identified at various wavelengths, the selection biases from each method and the physical properties of the host galaxies.

1.3 The Rest-frame Optical Spectroscopy

Obtaining a detailed description of the gas, dust content, metallicty, and SMBH properties requires high quality optical spectroscopy. In the local Universe the Sloan Digital Sky Survey (SDSS, York et al. 2000) enabled astronomers to analyze AGN and the stellar populations in more than 10^6 galaxies. The completeness of the SDSS sample is ideal for statistical analysis of galaxies. However, to understand the co-evolution of SMBHs and galaxies we require observational datasets across cosmic time, and obtaining high resolution spectroscopic data for statistically large samples at higher redshifts is very challenging.

Several spectroscopic surveys such as PRIMUS (Coil et al. 2011) and DEEP2 (Newman et al. 2013) have provided spectroscopic redshift measurements for $10^4 - 10^5$ galaxies up to $z \sim 1$, but until recently astronomers had to rely primarily on photometric redshift measurements for studying AGN at higher redshifts (e.g. Xue et al. 2010; Bongiorno et al. 2012)

The cosmic peak of star formation and AGN accretion both occurred at $z \sim 2$ (the Universe was ~ 3 billion years old) which makes $z \sim 2$ a critical epoch in galaxies' evolution. With the commissioning of multi-object near-infrared (NIR) spectrographs

such as KMOS (Sharples et al. 2013) on the Very Large Telescope (VLT) and and MOSFIRE (McLean et al. 2012) on the Keck I telescope, obtaining the rest-frame optical spectra of large samples of galaxies at $z \sim 2$ has now become possible (the rest-frame optical spectra for $z \sim 2$ sources shifts to the observed near-IR wavelengths). In this dissertation we present the results from high resolution rest-frame optical spectroscopic data obtained with the MOSFIRE spectrograph in the MOSDEF survey.

1.4 Thesis Outline

The outline of this dissertation is as follows. Chapter 2 presents the evidence for a connection between AGN fueling and star formation by investigating the relationship between the luminosities of AGN and SFR of the host galaxies at $0.2 < z < 1.2$ using data from the PRIMUS survey. In this chapter we also quantify the probability of a galaxy hosting an AGN for both the star-forming and quiescent galaxy populations. In Chapter 3 we present the results from the MOSDEF survey on the identification, selection biases, and host galaxy properties of X-ray, IR, and optically selected AGN at $1.4 < z < 3.8$. In Chapter 4 we investigate the nature of so-called "mid-infrared excess" galaxies, that have a SFR inferred from mid-infrared data elevated relative to that measured from other multi-wavelength data. We probe various parameters that could result in such elevation including AGN contribution using the multi-wavelength datasets of the MOSDEF survey. In Chapter 5 we summarize the main findings of this dissertation and describe the future research directions.

Chapter 2

PRIMUS: The relationship between Star formation and AGN accretion

2.1 abstract

We study the evidence for a connection between active galactic nuclei (AGN) fueling and star formation by investigating the relationship between the X-ray luminosities of AGN and the star formation rates (SFRs) of their host galaxies. We identify a sample of 309 AGN with $10^{41} < L_{\rm X} < 10^{44}$ erg s^{-1} at $0.2 < z < 1.2$ in the PRIMUS redshift survey. We find AGN in galaxies with a wide range of SFR at a given L_X. We do not find a significant correlation between SFR and the observed instantaneous L_X for star forming AGN host galaxies. However, there is a weak but significant correlation between the mean $L_{\rm X}$ and SFR of detected AGN in star forming galaxies, which likely reflects that $L_{\rm X}$ varies on shorter timescales than SFR. We find no correlation between stellar mass and $L_{\rm X}$ within the AGN population. Within both populations of star forming and quiescent galaxies, we find a similar power-law distribution in the probability of hosting an AGN as a function of specific accretion rate. Furthermore, at a given stellar mass, we find a star forming galaxy $\sim 2-3$ more likely than a quiescent galaxy to host an AGN of a given specific accretion rate. The probability of a galaxy hosting an AGN is constant across the main sequence of star formation. These results indicate that there is an underlying

connection between star formation and the presence of AGN, but AGN are often hosted by quiescent galaxies.

2.2 Introduction

It has been several decades since the first observations of galaxies with strong emission lines in their central regions (Seyfert 1943) and the classification of such sources as Active Galactic Nuclei (AGN). Since then, the range of observational phenomena associated with AGN has expanded to include sources classified based on a variety of X-ray, optical, infrared and radio criteria (e.g. Antonucci 1993) and there have been numerous investigations into the physical nature of these AGN (for a recent review see Alexander & Hickox 2012). It is now widely accepted that AGN activity is due to the presence of a supermassive black hole (SMBH) accreting gas and dust in the circumnuclear region, forming an accretion disk that ultimately powers the AGN activity. Studies from recent decades have established that SMBHs reside in almost all galaxies with a bulge or spheroid component (e.g. Kormendy & Richstone 1995; Kormendy et al. 2011), but what triggers AGN activity in some galaxies and not others is still a matter of debate. During the accretion process a tremendous amount of energy is released, a fraction of which can be injected into the circumnuclear region, the host galaxy or even the wider galactic environment in the form of electromagnetic or mechanical output. However, it is still unclear to what extent the injection of energy takes place and whether it has a strong effect on evolution of the host galaxy.

Various observational investigations support the idea that there is a close connection between the growth of SMBHs and the growth of their host galaxies. These studies find **correlations** between the SMBH mass and the bulge stellar mass (Magorrian et al. 1998) or velocity dispersion (e.g. Ferrarese & Merritt 2000; Gebhardt et al. 2000; Kormendy et al. 2011) of the host galaxy. This indicates that SMBHs and galaxies

must, on average, grow together, but whether this indicates a causal connection between these processes remains unclear (e.g. Peng 2007; Jahnke & Macciò 2011). Furthermore, the global star formation rate (SFR) density of galaxies and the SMBH accretion rate density evolve similarly with redshift (e.g. Boyle & Terlevich 1998; Silverman et al. 2008; Aird et al. 2010; Assef et al. 2011), indicating that the growth of galaxies and their central SMBHs are related in a global sense. However, it is unclear whether the level of AGN activity itself and host galaxy properties such as SFR are linked within individual galaxies.

A number of theoretical models and simulations suggest that AGN activity and star formation in galaxies are linked through a common cold gas inflow from galaxy mergers (e.g. Di-Matteo et al. 2005; Hopkins et al. 2006; Somerville et al. 2008). Some observational studies find that galaxies with the highest SFRs are associated with merger events (e.g. Shi et al. 2009; Kartaltepe et al. 2010, 2012). Due to the high fraction of quasars in merging systems, several authors have proposed that nuclear activity is also tightly connected to merger events (e.g. Sanders & Mirabel 1996; Canalizo & Stockton 2001; Ivison et al. 2010). However, recent studies find little to no connection between AGN activity and the incidence of merger events in galaxies with moderate luminosity AGN (e.g. Schawinski et al. 2011; Kocevski et al. 2012), suggesting that secular processes such as turbulence and disk instabilities are more effective in enhancing nuclear accretion activity for AGN with moderate luminosities (e.g. Mullaney et al. 2012b; Rosario et al. 2012).

Studies of the locations of AGN host galaxies in the optical color-magnitude diagram are useful to investigate the role of AGN in the evolution of their host galaxies. Galaxies can be divided into two general populations in this diagram: the blue cloud, consisting of predominantly star forming galaxies, and the red sequence, comprised mainly of quiescent, passively evolving galaxies (e.g. Blanton et al. 2003; Bell et al.

2003; Baldry et al. 2004). There is also a third population, known as the green valley, that includes galaxies in transition between the other two populations (e.g. Mendez et al. 2011). Many studies have demonstrated that X-ray detected AGN from $0 < z < 1$ are not preferentially found in galaxies with the highest levels of star formation. Instead, they appear to be in the reddest part of the blue cloud, in the green valley, or on the red sequence (e.g. Nandra et al. 2007; Coil et al. 2009; Hickox et al. 2009; Georgakakis & Nandra 2011). There is also evidence that high-luminosity AGN preferentially reside in luminous, massive, bulge-dominated galaxies (e.g. Schade et al. 2000; Pagani et al. 2003; Dunlop et al. 2003; Floyd et al. 2004). Taken at face value, these results seem to indicate that AGN may, via feedback to their host galaxy, extinguish star formation and could be responsible for the transition of their hosts from the blue cloud to the red sequence.

However, Silverman et al. (2009) and Xue et al. (2010) showed that stellar mass selection biases have strong effects on these results and that the preference for green and red host galaxies is due to AGN generally being found in massive galaxies. Xue et al. (2010) showed that while the fraction of AGN increases in a population with more massive galaxies, in a sample with matched stellar mass host galaxies, AGN are equally likely to be found in any host population. Aird et al. (2012) further showed that the observed prevalence of massive host galaxies is due to a selection effect related to the underlying distribution of specific accretion rates (AGN luminosity scaled relative to host stellar mass). Essentially, a more massive galaxy tends to host a more massive BH, which is easier to detect for a given specific accretion rate. Therefore, while AGN will preferentially be detected in massive galaxies, they actually reside in galaxies with a wide range of stellar mass.

Whether there is a preference for AGN to be found in star forming galaxies, once stellar mass-dependent biases are accounted for, remains an open question. Aird et al. (2012) measured the distribution of accretion rates within AGN hosts in the blue

cloud, green valley, and red sequence and found a similar accretion rate distribution in all populations. They further found that there was a mild (factor ~ 2) enhancement in the probability of a galaxy of a given stellar mass hosting an AGN for galaxies with blue or green rest-frame optical colors. Bongiorno et al. (2012) used specific SFR (estimated from fits to the optical–to–near-infrared spectral energy distributions) to split their galaxy sample into star forming and quiescent galaxies, finding no significant differences in the probability of hosting an AGN for galaxies in either population. More recently, Hernán-Caballero et al. (2014a) found that AGN hosts have similar distributions of rest frame optical colors to inactive galaxies of the same stellar mass but are more likely to be hosted by galaxies with younger stellar populations. Georgakakis et al. (2014a) also split AGN hosts into star forming and quiescent populations based on their $U-V$ versus $V-J$ colors (which should be more robust to dust extinction than rest-frame optical colors) and found that the space density of star forming hosts is higher than for quiescent hosts, with some weak evidence for differences in the shape of the accretion rate distributions.

A number of recent studies have used *Herschel* far infrared data, which provides a more robust tracer of the total SFR and is not impacted by dust extinction, to compare AGN hosts to the wider galaxy population. In *Herschel*-detected populations, Mullaney et al. (2012b), Santini et al. (2012) and Rosario et al. (2013) all found evidence for enhanced SFR in AGN hosts, compared to non-active galaxies of the same stellar mass, and argued that the bulk of moderate-luminosity AGN are hosted by normal star forming galaxies. However, *Herschel* is only able to detect galaxies that are bright at far-infrared wavelengths and thus generally have high SFRs, making it difficult to measure the fraction of quiescent hosts and compare the SFRs of all AGN hosts to the full population of star forming galaxies. However, given that the presence of dust can redden UV-optical colors, results that rely solely on optical colors may be biased. Cardamone et al. (2010) found that dust reddening affects the colors of some star forming AGN host galaxies, pushing

them to the green valley.

In addition to determining whether AGN are more likely to reside in star forming or quiescent host galaxies, several authors have studied whether there is an overall correlation between the level of star formation and the level of nuclear activity, as traced by the X-ray luminosity, in individual galaxies. Rovilos et al. (2012) found no evidence for a correlation in AGN with $L_{\rm X} < 10^{43.5}$ erg s^{-1} at $z < 1$ but a significant correlation at higher X-ray luminosity at $z > 1$, using a sample of X-ray detected AGN in the *Chandra* Deep Field–South (CDFS). Mullaney et al. (2012b) use *Herschel*-detected moderate luminosity ($L_{\rm X} = 10^{42-44}$ erg s^{-1}) X-ray AGN in the CDFS and *Chandra* Deep Field–North (CDFN) fields at $0 < z < 3$ and found no evidence of a correlation between SFR and X-ray luminosity, once the overall evolution of the average SFR with redshift is accounted for. Rosario et al. (2012) find similar results, using even larger AGN samples, including the COSMOS field. However, Rosario et al. (2012) did find a correlation in the most luminous AGN with $L_{AGN} \gtrsim 10^{45}$ erg s^{-1} at $z < 1$, which they interpret as due to major merger events. In addition, Mullaney et al. (2012a) found that the ratio of SMBH growth to SFR does not change with the stellar mass and redshifts at $z < 2.5$. Therefore, they suggest that rather than violent mergers, secular processes are responsible for both star formation and SMBH growth in majority of the galaxies with moderate nuclear activity.

There is some evidence that optically luminous AGN are found in galaxies with enhanced SFRs (e.g. Floyd et al. 2013). However, Page et al. (2012) found that star formation was suppressed in their sample of luminous X-ray detected AGN at $1 < z < 3$ with spectroscopic redshifts and *Herschel*/SPIRE 250 μm detections in the CDFN. More recently, Harrison et al. (2012) found no sign of star formation suppression in powerful AGN hosts using a larger sample. Moreover, Harrison et al. (2012) found that the average SFR in galaxies hosting AGN with luminosities in range of $10^{43} < L_{\rm X} < 10^{45}$ erg s^{-1}

at $1 < z < 3$ is constant as a function of L_X, consistent with results from Mullaney et al. (2012b) and Rosario et al. (2012).

Studies of lower luminosity AGN have been carried out in the local Universe. Using a sample of nearby Seyfert galaxies Diamond-Stanic & Rieke (2012) found a strong correlation between the AGN luminosity and the SFR in the circumnuclear regions (**$r < 1$ kpc**); however they found no correlation with the galaxy-wide SFR. Kauffmann et al. (2003b) studied optically-selected AGN in SDSS and found that strong nuclear activity is associated with younger stellar populations, indicative of higher levels of recent star formation.

All of the above studies use instantaneous accretion rate to investigate correlations with SFR. However, a number of recent studies have instead focused on the *average* accretion rate, averaging over both active and non-active galaxies, and SFR. Chen et al. (2013) studied star forming galaxies detected by *Herschel* in the Boötes field at $z < 1$, including 34 X-ray and 87 MIR-detected AGN, and found that the average accretion rate is correlated with SFR. They also compared their result with a small sample of 20 X-ray detected AGN in FIR bright galaxies from Symeonidis et al. (2011a) at $z \sim 1$ and found a consistent trend in both samples. However, when they corrected for the effects of flux limits on their results, along with the evolution of the X-ray luminosity function and average SFR with redshift, the correlation becomes weaker. Hickox et al. (2014) presented a model where all star forming galaxies host an AGN and the average AGN luminosity is correlated with the SFR. This model explains the correlation between the average AGN luminosity and SFR seen by Chen et al. (2013). They also use their model to investigate the correlation between the instantaneous accretion rate and star formation. Their results indicate that SFR and X-ray luminosity are mostly decoupled, with a correlation only at $z < 1$ in galaxies with powerful AGN. This correlation disappears at higher redshifts, consistent with Mullaney et al. (2012b) and Rosario et al. (2012).

Hickox et al. (2014) state that star formation and accretion activity are linked over long timescales but in low to moderate luminosity AGN the underlying correlation is hidden due to the AGN variability. Thus, we may not observe any direct correlation between SFR and the *instantaneous* AGN luminosity in flux-limited AGN samples.

In this paper, we investigate the correlation between the SFR and stellar mass of AGN host galaxies with the nuclear activity of their SMBHs, using a large sample of galaxies with spectroscopic redshifts from the PRIsm MUlti-object Survey, PRIMUS, (Coil et al. 2011; Cool et al. 2013). We use X-ray data from *Chandra* and *XMM-Newton* surveys that cover ~ 3 deg^2 of the PRIMUS area to identify a large sample of moderate-luminosity ($10^{41} < L_{\rm X} < 10^{44}$ erg s^{-1}) AGN within our galaxy sample. We use X-ray luminosity as the tracer of AGN activity and estimate SFRs and stellar masses by fitting the observed galaxy spectral energy distribution (SED) using UV and optical photometry of our sources. With this data, we are able to probe down to relatively low SFRs and robustly separate our sample into quiescent and star forming populations. We also measure the fraction of AGN with star forming versus quiescent host galaxies (compared to a stellar mass-matched galaxy samples) and quantify how this fraction is changing with redshift, which could potentially drive any observed correlations in the overall sample. Finally, we measure the probability of a galaxy hosting an AGN and the distribution of specific accretion rates for both the star forming and quiescent galaxy populations, updating the study from Aird et al. (2012) using our more robust galaxy classifications. We also further sub-divide the galaxy population to study the specific accretion rate distribution as a function of the specific SFR.

Section 2.3 briefly describes our data and the stellar mass completeness limits that we use to minimize observational biases. In Section 2.4 we describe our results on the correlation between SFR and AGN X-ray luminosity in our full sample. We also investigate this correlation within sub-populations of star forming and quiescent galaxies.

In addition, we consider the connection between galaxy star formation and AGN specific accretion rate and quantify the probability of a galaxy hosting an AGN as a function of specific SFR. We interpret our results in Section 2.5 and investigate the variation of the average X-ray luminosity of AGN with the star formation activity of their host galaxies. We summarize our results in Section 2.6. Throughout the paper we adopt a flat cosmology with Ω_Λ =0.7 and H_0=72 km s^{-1}Mpc^{-1} and all magnitudes are on AB system.

2.3 Data

In this study, we use multi-wavelength data from the PRIMUS survey covering four fields on the sky, including the *Chandra* Deep Field South (CDFS), COSMOS, ELAIS S1, and XMM-LSS fields. All of these fields have deep UV, optical, and IR imaging as well as spectroscopic redshifts from PRIMUS. We also use X-ray imaging from *Chandra* and *XMM-Newton* to identify AGNs within the PRIMUS samples. We describe these datasets below, as well as our method of estimating stellar masses and SFRs for our sources by fitting their spectral energy distributions (SEDs).

2.3.1 PRIMUS

We use data from PRIMUS, the largest faint galaxy, intermediate-redshift survey completed to date. The PRIMUS survey used the IMACS spectrograph on Magellan I Baade 6.5 m telescope at Las Campanas observatory, with a slitmask and a low-dispersion prism. The survey has a spectroscopic resolution of R $\sim$ 40 and covers a total of 9.1 deg^2 of sky, spread over seven extragalactic fields with deep multiwavelength data. Objects were targeted to $i \sim 23$ using well-understood targeting weights. Four additional fields were targeted that had a large number of prior, high-resolution spectroscopic redshifts; these data were used for calibration purposes. In these calibration fields higher priority

was given to targets with prior spectroscopic redshifts. The full details of the survey, targeting and data summary are presented in Coil et al. (2011).

In PRIMUS, objects are classified as stars, broad-line AGNs (BLAGNs) and galaxies based on their spectra. In each class, low-resolution spectra and multi-wavelength photometry of the objects are simultaneously fit with an empirical library of templates. For this study we restrict our sample to the sources with robust redshifts ($Q \geq 3$, see Coil et al. 2011). The total PRIMUS catalog contains $\sim 120,000$ robust redshifts at $z \sim 0-1.2$, with a redshift precision of $\sigma_z/(1+z) \sim 0.005$. For further details of the data reduction, survey completeness, redshift fitting and precision see Cool et al. (2013).

PRIMUS targeted fields with existing deep multi-wavelength imaging. These data include X-ray imaging from *Chandra* and *XMM-Newton*, UV imaging from GALEX, deep optical imaging from a range of telescopes, and infrared imaging from the Infrared Array Camera (IRAC) and the Multiband Imaging Photometer (MIPS) on *Spitzer*. In this paper, we restrict our analysis to spectroscopic sources targeted within the area with joint GALEX UV, optical, and *Spitzer* IRAC imaging. We thus restrict our sample to the COSMOS, ELAIS-S1 and XMM-LSS science fields in PRIMUS. In Sections 2.4.1–2.4.4 we also use the PRIMUS calibration field CDFS-CALIB (hereafter CDFS), which overlaps with the deep *Chandra* X-ray coverage. Taken together, these four fields cover 4.96 deg^2 of the sky. We exclude the X-ray AGN and galaxy samples in the CDFS field below in the analysis of Section 2.4.5, as it does not provide a uniformly targeted sample of galaxies, which is required for the analysis in that section.

2.3.2 X-ray data

We use X-ray data to identify AGN within the PRIMUS galaxy sample. We have compiled X-ray catalogs in the CDFS, COSMOS, ELAIS S1, and XMM-LSS fields based on published *Chandra* and *XMM-Newton* surveys. In the CDFS field, we use the

Lehmer et al. (2005) and Luo et al. (2008) X-ray catalogs corresponding to the 2 Ms observations of the central region (reaching depths of $f_{2-8\mathrm{keV}} \sim 5.5 \times 10^{-17}$ erg s^{-1} cm^{-2}) and the flanking 250 ks observations (reaching depths of $f_{2-8\mathrm{keV}} \sim 6.7 \times 10^{-17}$ erg s^{-1} cm^{-2}). The entire COSMOS field was observed with *XMM-Newton* to depths of $f_{2-10\mathrm{keV}} \sim 3 \times 10^{-15}$ erg s^{-1} cm^{-2} (Hasinger et al. 2007); additionally the central ~ 0.9 deg^2 was observed with *Chandra* to depths of $f_{2-10\mathrm{keV}} \sim 8 \times 10^{-16}$ erg s^{-1} cm^{-2} (Elvis et al. 2009). In the ELAIS-S1 field we use the catalog of Puccetti et al. (2006), based on the *XMM-Newton* observations that reach $f_{2-10\mathrm{keV}} \sim 3 \times 10^{-15}$ erg s^{-1} cm^{-2}. Finally, in XMM-LSS we use X-ray data available from the both the Pierre et al. (2007) catalog and from the *XMM-Newton* Deep Survey (Ueda et al. 2008) down to the $f_{2-10\mathrm{keV}} \sim 2 \times 10^{-15}$ erg s^{-1} cm^{-2}. We use the likelihood ratio technique (e.g. Sutherland & Saunders 1992a; Ciliegi et al. 2003a; Brusa et al. 2007a; Laird et al. 2009) to identify reliable optical counterparts (in the *i* or *R* band) to the X-ray sources; for objects with multiple counterparts, the match with the highest ratio is chosen. For full details of the construction of our X-ray catalogs and matching procedure see Aird et al. (2012) and Mendez et al. (2013).

In this study, we consider a sample of obscured AGN detected in the hard (2–10 keV) X-ray band, where we have excluded objects that were classified as BLAGN in the PRIMUS spectra. These BLAGN constitute about 12% of our AGN sample. As their optical emission can dominate over the optical light of the host galaxy, for such sources we are unable to estimate the stellar mass and SFR of the host. Restricting to hard X-ray (2–10 keV) detections ensures that we can estimate the X-ray luminosity with reasonable accuracy and are not strongly biased against the selection of moderately obscured sources. Although hard X-ray emission passes through regions with moderate hydrogen column densities, it can not penetrate Compton-thick regions with heavy obscuration; thus our sample lacks this potentially important population.

We also restrict our analysis to sources with moderate X-ray luminosities in the range $10^{41} < L_X < 10^{44}$ erg s^{-1} resulting in a final sample of 309 AGN. The lower limit of 10^{41} erg s^{-1} ensures that the observed X-ray luminosity is dominated by light from an AGN rather than from star formation activity in the host galaxy. The upper limit ensures that the optical light of the host is not strongly contaminated by the presence of an AGN, such that we can estimate stellar masses and SFRs. It also ensures that our sample is not strongly biased by our exclusion of BLAGN, which constitute a higher fraction of the X-ray selected AGN population at high luminosities. To summarize, our AGN sample consists of 309 sources with hard-band X-ray detections and robust redshifts from PRIMUS (in the range $0.2 < z < 1.2$) that are not classified as BLAGN (thus the host galaxy dominates the optical light) and have X-ray luminosities within the range $10^{41} < L_X < 10^{44}$ erg s^{-1}.

2.3.3 Stellar Mass and SFR Estimates

SED fitting is a widely adopted method for estimating the physical properties of galaxies. We estimate stellar masses and SFRs of the galaxies by fitting the observed SED based on the UV and optical photometry of our sources. As we exclude BLAGN and do not include IRAC photometry in our SED fits, we do not include an AGN contribution in the SED fitting. We fit the SEDs using the `iSEDfit` code (Moustakas et al. 2013), which is a Bayesian fitting code that compares the observed photometry for each source to a large Monte Carlo grid of SED models which span a wide range of stellar population parameters (e.g. age, metallicity, dust, and star formation history) to estimate the stellar mass and SFR of a galaxy.

With `iSEDfit` we find the posterior probability distribution of stellar mass and SFR of a galaxy by marginalizing over all of the other parameters. We then take the median of the probability distribution functions as the best estimate of the stellar mass or

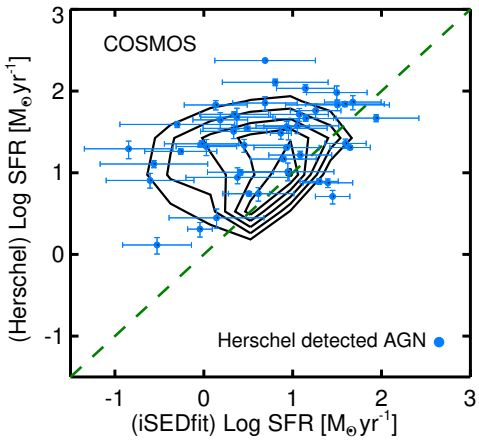

Figure 2.1. The SFR derived from *Herschel* versus from `iSEDfit` for sources in the COSMOS field. We use *Herschel* deep 100 μm observations and convert the FIR luminosity to a SFR using Equation (2.1). Contours show the distribution of PRIMUS galaxies detected by *Herschel*, while filled blue circles indicate AGN detected by *Herschel*. The bulk of the AGN sample is not *Herschel*-detected. The green dashed line indicates the 1:1 relation. While the majority of *Herschel*-detected galaxies lie close to this 1:1 line, there is a clear population that scatters above the line indicating that we underestimate the SFR using `iSEDfit`, although the shape of this distribution will be due to *Herschel* only detecting dusty star-forming galaxies with high SFRs. The *Herschel*-detected X-ray sources span a similar space to the galaxies; upper limits on the *Herschel* SFRs for X-ray sources without *Herschel* detections place them in a similar space, confirming that the shape of the distribution is primarily driven by the limited depths of the *Herschel* data.

SFR of each galaxy. The uncertainty on each parameter is calculated as one quarter of the 2.3–97.7 percentile range of the probability distributions, which would be equivalent to a 1σ uncertainty in the case of a Gaussian distribution. For details on `iSEDfit` see Moustakas et al. (2013).

For the SED fitting used in this paper, we adopt the Flexible Stellar Population Synthesis (FSPS) models (Conroy et al. 2009; Conroy & Gunn 2010) with Chabrier (2003) initial mass function (IMF) from 0.1 to 100 $M_\odot$ and stellar metallicity in the range of $0.004 < Z < 0.05$. We consider exponentially declining star formation histories $\Psi \propto \frac{1}{\tau} \exp\left(\frac{-t}{\tau}\right)$, allowing for τ within the range of $0.01 < \tau < 1$ Gyr. We also allow for stochastic bursts of star formation on top of the smoothly decaying star formation

histories. In addition, we include Charlot & Fall (2000) time dependent dust attenuation where attenuation in stellar population older than 10 Myr is less than younger populations (Charlot & Fall 2000; Wild et al. 2011).

In this work, we estimate stellar masses and SFRs using `iSEDfit` on our UV and optical photometry. To test the accuracy of our SFRs, we compare them with *Herschel* Space Observatory deep far infrared observations of the COSMOS field. We use deep 100 μm observations of the PACS Evolutionary Probe, PEP12 (Lutz et al. 2011), reaching a 3σ limit of 5 mJy at 100 μm (Berta et al. 2011). We then use the Kennicutt (1998) relation, given here as Equation (2.1), using Chabrier IMF to convert the FIR luminosity to SFR:

$$\frac{SFR}{M_{\odot} yr^{-1}} = 1.09 \times 10^{-10} \frac{L_{IR}}{L_{\odot}} \tag{2.1}$$

Figure 2.1 compares the *Herschel* derived SFR with our estimate from `iSEDfit` for PRIMUS sources in the COSMOS field. Contours show the distribution of PRIMUS galaxies that are detected by *Herschel*, while blue circles show PRIMUS X-ray AGN that are detected by *Herschel*. The dashed line represents the 1:1 relation. As can be seen in the figure, the error bars on the *Herschel* estimated SFRs are much smaller than those from `iSEDfit` and are likely underestimated, as a single template is used to calculate the total IR luminosity.

While many AGN and galaxies lie near the 1:1 relation, there is a sizable portion of the sample well above the line, with the SFR estimated from *Herschel* much higher than the SFR from `iSEDfit`. This is not surprising, as the IR luminosity is a more accurate probe of the SFR in dusty galaxies, while the inferred SFR from fitting the UV and optical SED primarily reflects unobscured star formation (though `iSEDfit` does fit and account for dust obscuration). Most PRIMUS X-ray AGN in COSMOS are

not detected by *Herschel*, and for these sources we calculate the 3σ upper limits on SFR as estimated from the *Herschel* imaging. These AGN not detected by *Herschel* show a similar overall offset as the detected AGN in this figure, though we only have upper limits, such that the true values may lie close to the 1:1 line. A histogram of the *Herschel* to `iSEDfit` SFR differences in the *Herschel*-detected galaxy sample peaks at $\Delta(\log SFR) = 0$ but has a median offset of 0.6 dex. Within this sample, 42% of the sources have a *Herschel* SFR that is more than a factor of three higher than the `iSEDfit` SFR, although the shape of this distribution will be strongly skewed due to the limited depths of the *Herschel* data.

We note that, based on the KS test, the distributions of $\Delta(\log SFR)$ for the *Herschel*-detected AGN and *Herschel*-detected galaxies are not significantly different. Thus, the overall SFR estimated by `iSEDfit` for dusty galaxies may be systematically low, which appears to be due to `iSEDfit` underestimating the dust extinction in some of the *Herschel*-detected galaxies (and thus underestimating the SFR). However, what we are interested in here is whether there is a correlation between SFR and L_X. A systematic offset will not affect our results, although additional scatter in our SFR estimates could wash out any underlying correlations. Additionally, as *Herschel* detects warm dust heated by star formation, the *Herschel*-detected sample includes only the most dusty star forming galaxies, such that the SFR differences in the full PRIMUS galaxy and AGN sample will be less pronounced.

Below in Section 2.4.2 we split the PRIMUS sample into star forming versus quiescent galaxies using the `iSEDfit` stellar mass and SFR values of each source. Here we estimate the contamination of our quiescent sample by star forming galaxies, by finding that in the COSMOS field 7% of our quiescent sample (defined using `iSEDfit` outputs) is detected by *Herschel*; these galaxies are therefore star forming galaxies and are misclassified.

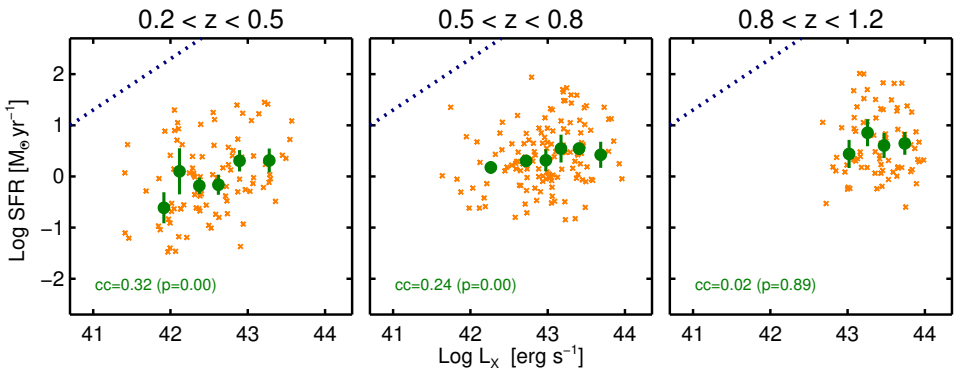

Figure 2.2. The SFR versus L_X for a sample of non-broad line AGN in four PRIMUS fields, including CDFS, COSMOS, ELAIS S1 and XMM-LSS, for three redshift bins spanning $0.2 < z < 1.2$. Orange crosses show individual AGN, while green circles illustrate the median SFR in bins of L_X. The error bars show the uncertainty on our calculation of the median points, measured from bootstrap resampling. The blue dotted line shows the SFR expected if the X-ray emission is from HMXBs; the fact that our sources are all well below this line indicates that the X-ray emission is from AGN. The correlation coefficients and correlation significance of the individual points in each panel are calculated from Spearman's rank correlation. A small p value denotes it is unlikely for a correlation to have been occurred by accident and the correlation is considered significant if the p value is less than 0.05. The lower two redshift panels show a weak trend between SFR and L_X, which is not apparent in the highest redshift panel, where our data probe a narrower range of L_X.

2.3.4 Stellar mass completeness limits

As PRIMUS is a flux-limited survey, targeting objects to $i \sim 23$, this introduces a bias into our sample where we are unable to detect low-mass galaxies at higher redshifts, unless they have high SFRs (increasing the amount of blue light from the galaxy). To minimize this bias we define a stellar mass limit above which we can detect all galaxies, regardless of their SFR. This stellar mass limit is a smooth function of redshift and is slightly different in each field, depending on the band used for target selection (see also Aird et al. 2012). Briefly, we define a template for a maximally old simple stellar population at $z \sim 5$ and calculate the mass-to-light ratio as a function of redshift, allowing the template population to evolve passively with time. Then in each field we convert the

targeting magnitude limit to a stellar mass limit as a function of redshift, as we keep only those galaxies with stellar masses above this limit. This restricts our sample to include only more massive galaxies at higher redshifts, but it ensures that we are not biased towards the star forming galaxy population and that we have a sample that is complete to a given stellar mass at all redshifts. After applying these stellar mass limits, our final sample across the four fields used here consists of 32,865 galaxies at $0.2 < z < 1.2$, of which 283 are AGN detected in the hard X-ray band with $10^{41} < L_{\rm X} < 10^{44}$ erg s^{-1}.

2.4 Results

In this section, we investigate the relationship between SFR and X-ray luminosity, $L_{\rm X}$, in our AGN sample. In order to uncover whether stellar mass could be an underlying variable, we also investigate the stellar mass dependence of $L_{\rm X}$. We further divide our full AGN sample into those with star forming and quiescent host galaxies, to consider how SFR and stellar mass vary with $L_{\rm X}$ within each host population. We also measure the probability that a galaxy of a given stellar mass and redshift hosts an AGN, as a function of the specific SFR of the galaxy.

2.4.1 The relationship between SFR and stellar mass with $L_{\rm X}$

Figure 2.2 shows the SFR of AGN host galaxies plotted as a function of $L_{\rm X}$, in three redshift bins spanning $0.2 < z < 1.2$. Orange crosses show individual AGN, while green circles show the median SFR in bins of $L_{\rm X}$, where each bin contains at least 15 sources, to visually highlight any correlations. X-ray emission at these luminosities can arise not only from AGN but potentially from high mass X-ray binaries (HMXBs), which are tracers of star formation activity and generally have lower luminosities, $L_{\rm X} \sim 10^{35-40}$ erg s^{-1}. The dotted blue line in Figure 2.2 is from Ranalli et al. (2003) and shows the

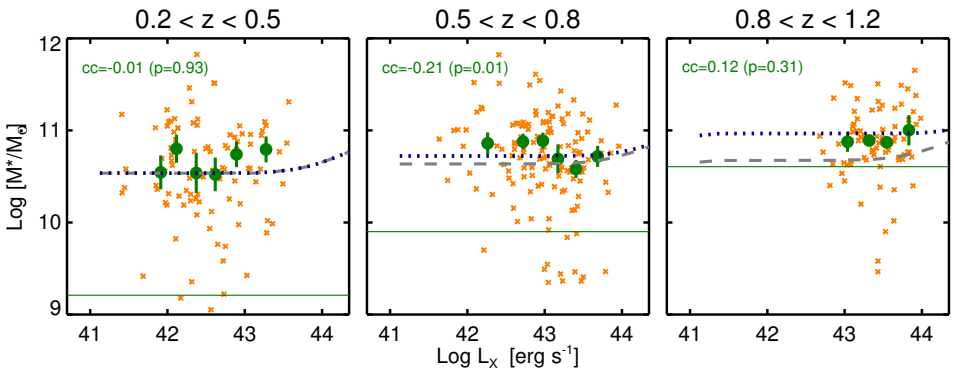

Figure 2.3. Stellar mass versus L_X for our sample of non-broad AGN in three redshift bins spanning $0.2 < z < 1.2$. Orange crosses show individual AGN while green circles illustrate the median stellar mass in bins of L_X. The error bars show the uncertainty on median points, measured from bootstrap resampling. The solid dark green line indicates the PRIMUS stellar mass completeness limit. The grey dashed line is a prediction from a model presented in Aird et al. (2013) and shows the predicted median stellar mass as a function of L_X in each redshift range. The blue dotted line shows the prediction of this model for sources above the PRIMUS mass completeness limit. There is no significant trend between stellar mass and L_X in the first and last panel but there is a negative correlation in the middle panel that is mainly due the sources below the mass completeness limit.

relation between SFR and L_X for HMXB:

$$\frac{SFR}{M_{\odot} yr^{-1}} = 2.0 \times 10^{-40} L_{\mathrm{X(2-10\ Kev)}}\ erg\ s^{-1} \tag{2.2}$$

As this line is well above our sources, it indicates that the X-ray emission seen for our sample is from AGN and does not suffer from contamination by HMXBs.

For the median points shown in Figure 2.2, we estimate error bars using bootstrap resampling. The uncertainty shown reflects the variance among the median SFR in each of 1000 bootstrap samples. These errors are similar to the standard errors calculated in each L_X bin. This figure clearly shows that there is a wide spread in SFR at any given value of L_X, such that the standard deviation of the points is typically 3–4 times greater

than the error shown.

We use the *r_correlate* routine in IDL to find the correlation coefficients and correlation significance of the individual points in Figure 2.2. This routine computes the Spearman's rank correlation coefficient and the significance of its deviation from zero, p. This value indicates the probability of obtaining a desired event under the null hypothesis that the event happened purely by chance. A small p value denotes it is unlikely for the correlation to have been occurred by accident. A correlation is considered significant if the p value is less than 0.05. We quote p values to an accuracy of two decimal places, thus $p = 0.00$ indicates cases where we can reject the null hypothesis at a confidence level of $>$99.5%. The correlation coefficients for the individual points shown in Figure 2.2 are 0.32 (p=0.00), 0.24 (p=0.00), and 0.02 (p=0.89), respectively, from the lowest to the highest redshift bin.

In this figure, there is a large scatter in SFR in bins of L_X in all three redshift ranges. At a given L_X, the average SFR increases at higher redshifts, consistent with the overall increase in SFR seen in the galaxy population (e.g. Bell et al. 2005; Elbaz et al. 2007a; Noeske et al. 2007a). In the two lowest redshift ranges we see a weak positive correlation in the median points that is confirmed by the significance of the correlation coefficients measured above. We find no correlation between SFR and L_X in the highest redshift range, but we note that at higher redshifts we are probing a more limited range of X-ray luminosity.

To determine whether the observed trends in the first two panels are actually being driven by redshift-dependent selection effects, we measure the median redshift in the each bin of L_X. As the median redshift does not systematically vary with L_X, redshift is not driving any trends in Figure 2.2.

However, the weak correlation between SFR and L_X seen in the lower two redshift panels could be due to an underlying trend between stellar mass and L_X. Given that

within the galaxy population there is a positive correlation between SFR and stellar mass (e.g. Elbaz et al. 2007a; Karim et al. 2011), it is possible that the observed correlation between SFR and L_X could actually be due to an underlying correlation between stellar mass and L_X.

In Figure 2.3 we show the stellar mass of AGN host galaxies as a function of L_X. As in Figure 2.2, orange crosses indicate individual sources while green circles show median values in bins of L_X, and errors on the median points are calculated using bootstrap resampling. The standard deviation of the data points is larger than the error shown by a factor of 3–5. The correlation coefficients of the individual points in this figure are -0.01 (p=0.93), -0.21 (p=0.01) and 0.12 (p=0.31), respectively, for the three redshift ranges shown. We note that we have not applied the stellar mass completeness limits discussed above in Section 2.3.4 and we show our full X-ray AGN sample in both Figures 2.2 and 2.3. In Figure 2.3, we only find a significant correlation in the middle redshift range; however, the correlation is *negative* and appears to be driven by a small number of sources below the PRIMUS mass completeness limit shown with the solid dark green line. If we only consider sources above the stellar mass completeness limits, we do not find any significant correlation between stellar mass and L_X for X-ray AGN in any of the three redshift ranges. We thus conclude that the observed (weak, but significant) positive correlations between SFR and L_X in Figure 2.2 are *not* due to a positive correlation between stellar mass and L_X within our X-ray AGN sample.

The grey dashed line in Figure 2.3 is a prediction from a model presented in Aird et al. (2013). This model takes the stellar mass function of galaxies and populates the galaxies with AGN using a universal power-law distribution of specific accretion rates (the rate of accretion scaled relative the host stellar mass, see Section 2.4.3 below). The specific accretion rate distribution itself does not depend on stellar mass but has a normalization that evolves with redshift (motivated by the observational results of Aird

et al. 2012). The grey dashed line shows the predicted median stellar mass as a function of L_X, using this model, and in particular shows that the median stellar mass of AGN host galaxies should not vary significantly with L_X, over the luminosity range where we have data. The blue dotted line shows the prediction of this model for sources above the PRIMUS mass completeness limits, and the median points in our sample lie close to this line, confirming this lack of a correlation.

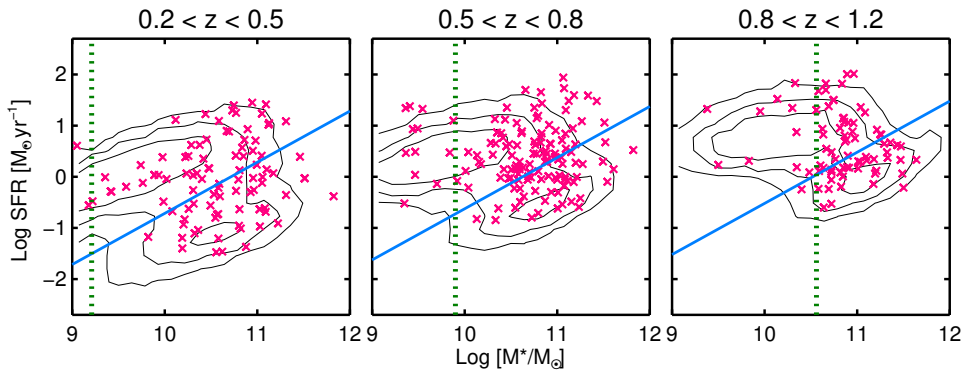

Figure 2.4. SFR versus stellar mass for PRIMUS galaxies and AGN, shown in three redshift ranges. Contours show the distribution of galaxies in this space; there are two distinct populations: star forming galaxies, with a relatively high SFR at a given stellar mass, and quiescent galaxies, with a low SFR at a given stellar mass. Red crosses show X-ray AGN, which reside in both star forming and quiescent host galaxies. The blue solid line is the classification used to define galaxies as being either star forming (above the line) or quiescent (below the line). This line evolves with redshift. The vertical dotted green line shows the PRIMUS stellar mass completeness limit, which is also a function of redshift. To create samples that are complete in stellar mass, we exclude sources to the left of this line.

There is a large scatter in the stellar mass at any given X-ray luminosity. We find that the average stellar mass of the AGN host galaxies in all three redshift ranges is higher than $10^{10}M_{\odot}$. This is consistent with prior literature, including Kauffmann et al. (2003b); Xue et al. (2010) and Aird et al. (2012), who find that observed AGN are predominantly hosted by moderately massive galaxies. While some recent studies have found evidence for AGN activity in much lower mass, dwarf galaxies, such sources represent a small

fraction of the X-ray selected population and have X-ray luminosities below our limit (e.g. Moran et al. 1999; Barth et al. 2004; Reines et al. 2011, 2013; Secrest et al. 2015). Nonetheless, we note that Aird et al. (2013) attribute the dominance of moderate-mass host galaxies in X-ray–selected AGN samples to the shape of the stellar mass function of galaxies, combined with the wide power-law distribution of AGN accretion rates, rather than an enhancement of AGN activity in galaxies of a particular stellar mass.

Overall, Figure 2.3 demonstrates that over the X-ray luminosity that we probe, $41 < \log L_{\rm X} < 44$, there is no correlation between AGN luminosity and host stellar mass within the AGN sample (although we note that our AGN sample is dominated by moderately massive galaxies, $M_* > 10^{10} M_\odot$ at all luminosities and redshifts). The weak correlation seen above between SFR and X-ray luminosity is therefore not due to an underlying correlation between $L_{\rm X}$ and stellar mass within the AGN sample.

2.4.2 The relationship between SFR and stellar mass with $L_{\rm X}$ for star forming and quiescent galaxies

Our results above indicate that there is a weak but significant correlation between SFR and $L_{\rm X}$ for AGN host galaxies for the lowest two redshift bins probed here, spanning $0.2 < z < 0.8$. We do not find a significant positive correlation between stellar mass and $L_{\rm X}$ for the same sample, indicating that stellar mass is not driving the observed SFR-$L_{\rm X}$ relation. We further investigate possible effects of the host population by splitting the AGN host galaxies into star forming and quiescent populations and determining whether a SFR-$L_{\rm X}$ relation exists within either of these populations alone.

We classify each AGN host galaxy as star forming or quiescent using its specific star formation rate, $sSFR$, which is defined as the SFR per unit stellar mass, $\frac{SFR}{M_*}$. Histograms of $\log sSFR$ of our full galaxy sample within relatively narrow redshift ranges show two prominent peaks: one corresponding to the "main sequence" of star forming

galaxies (Noeske et al. 2007a) and the other to quiescent galaxies. The locations of the peaks evolve with redshift, in that *sSFRs* are higher (on average) at higher redshift. To classify galaxies into star forming or quiescent, we wish to use the *sSFR* corresponding to the minimum between these two populations in the sSFR histogram. This minimum is not always clear in all of the (six) redshift bins used, but the peak of the star forming main sequence can be traced easily at all redshifts. We therefore first fit for the evolution of this peak, $sSFR_{max}$, as a linear function of redshift, which is given by:

$$\log(sSFR_{max}(z)) = 0.3 \times z - 9.62 \tag{2.3}$$

We then normalize the *sSFR* of each galaxy relative to this $sSFR_{max}(z)$, which we call the epoch normalized specific star formation rate, *ENsSFR* (see also Stott et al. (2012)) :

$$\log(ENsSFR) = \log(sSFR) - 0.3 \times z + 9.62 \tag{2.4}$$

Finally, we plot a histogram of $\log ENsSFR$ for all of galaxies, which exhibits a clear bimodality. We find the minimum between the two peaks of the bimodal distribution at $\log ENsSFR_{min} = -1.2$. We divide our sample into star forming and quiescent galaxies according to whether their *ENsSFR* is above or below $\log ENsSFR_{min}$, respectively. Ultimately, we apply the same classification scheme to our X-ray AGN sample.

Figure 2.4 shows the location of PRIMUS galaxies and AGN within the SFR-stellar mass plane, in the same three redshift ranges as used above. The contours indicate the location of PRIMUS galaxies, while red crosses show individual AGN host galaxies. The blue line shows the separation defined above between the star forming and quiescent populations (shown at the median redshift of each redshift range); galaxies above the line are considered to be star forming while galaxies below are classified as quiescent. The vertical dashed green line shows the stellar mass completeness limit for PRIMUS, at the

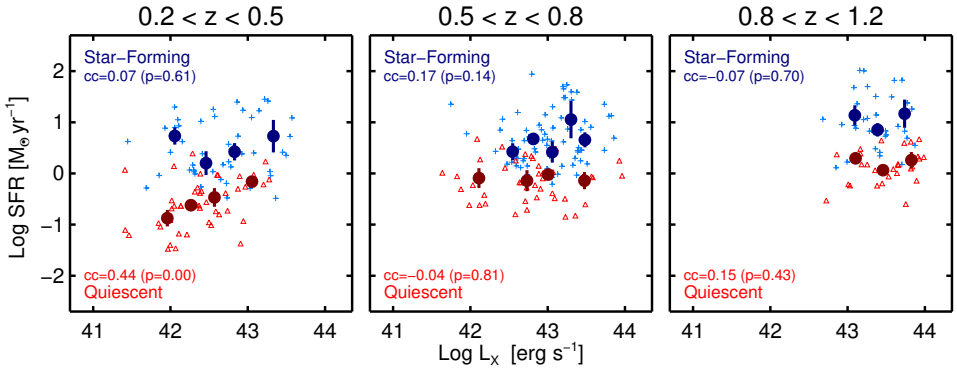

Figure 2.5. The SFR versus L_X of AGN host galaxies, in three redshift bins, where the host galaxies are split into star forming (blue plus) or quiescent (red triangle). Similar to Figure 2.2, the errors are measured using the bootstrap resampling. Blue and red circles show the median SFR in bins of L_X, for the star forming and quiescent host populations, respectively. There is a significant positive trend in quiescent host population in the lowest redshift panel that vanishes at higher redshifts. There is no significant correlation between SFR and L_X in star forming galaxies in any redshift bins.

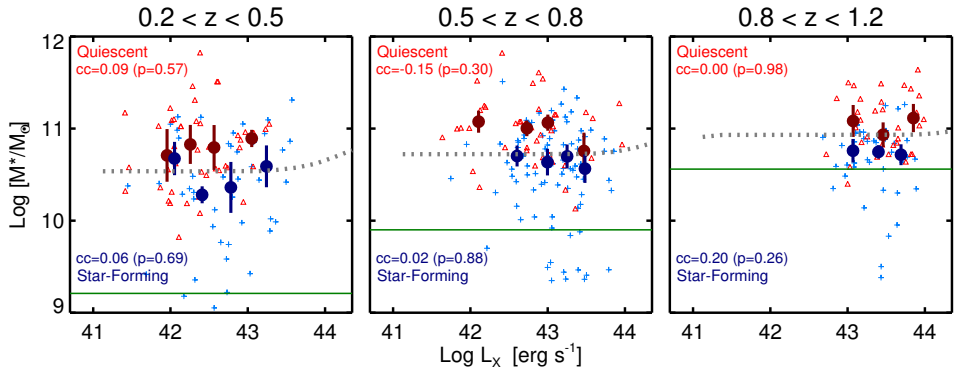

Figure 2.6. The average stellar mass versus L_X, in three redshift ranges. The host galaxies are split into star forming (blue plus) or quiescent (red triangle). The errors are measured using the bootstrap resampling. Similar to Figure 2.3, the grey dashed line is a prediction of stellar mass as a function of L_X from a model presented in Aird et al. (2013) for sources above PRIMUS mass completeness limit. The green solid line shows the PRIMUS stellar mass completeness limit, which is also a function of redshift. There is no significant correlation between stellar mass and L_X in either of populations above the mass completeness limit.

median redshift of that panel. Above this stellar mass limit we are complete for both star forming and quiescent galaxies (see Section 2.3.4 above). Figure 2.4 shows that AGN are present in both the star forming and quiescent galaxy populations. However, the most massive galaxies (and therefore AGN host galaxies) in the sample tend to be quiescent, especially at $z > 0.5$.

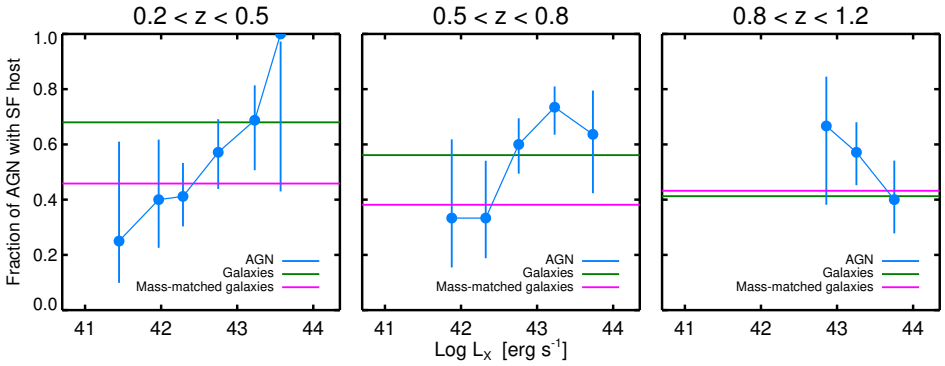

Figure 2.7. Variation of the fraction of AGN in star forming host galaxies with L_X, for stellar mass complete samples, shown with blue lines. The errors are calculated from the binomial distribution using the Bayesian method of Cameron (2011). The green lines show the fraction of all galaxies above the stellar mass completeness limits that are star forming, while the pink lines show this fraction for galaxy samples that have the same stellar mass distributions as the AGN host galaxies. While the star forming host fraction increases with increasing L_X in the lower two redshift ranges, given the error bars neither trend is significant. In the middle redshift range there is a 2σ difference between the total fraction of AGN host galaxies that are star forming and the fraction of stellar mass matched galaxies that are star forming.

We apply the above star forming versus quiescent classification to all PRIMUS galaxies, and we apply the stellar mass completeness limit as well, and show the SFR versus L_X of AGN host galaxies for each populations in Figure 2.5. The blue points show host galaxies on the star forming main sequence, while the red points show quiescent host galaxies. We find the median SFR in bins of X-ray luminosity, where we require a minimum of 12 and 10 AGN per bin for the star forming and quiescent populations, respectively. We note that these median points are for the purpose of illustrating the trends

in data and the numbers are chosen to have at least three L_X bins for each population in each panel. As above, error bars on the median points are from bootstrap resampling and the standard deviation in each population is larger than the errors shown by a factor of 3–4. We find a fairly high scatter in the SFR at a given L_X within each host galaxy population. However, due to the flux limit of the survey we probe a smaller range of L_X in the highest redshift panel.

Within the star forming population, the lack of a trend in the median points and the correlation coefficients (none of which are significant, as seen in the figure) confirm the absence of any significant correlation between SFR and L_X in all three redshift ranges probed here. Within the quiescent population there is a weak but significant trend in the lowest redshift range only; the correlation coefficients are 0.44 (p=0.00), -0.04 (p=0.81) and 0.15 (p=0.43), respectively from lowest to highest redshift.

We further show in Figure 2.6 the stellar mass versus L_X of the AGN host galaxies, split into the star forming and quiescent populations. As in Figure 2.5, the blue and red symbols represent star forming and quiescent galaxies, respectively, and the error bars are calculated using bootstrap resampling. The horizontal green solid line shows the PRIMUS stellar mass completeness limit at the median redshift of each panel, and the grey dotted line is from the model of Aird et al. (2013), as described in Section 2.4.1, for sources above this completeness limit.

Both galaxy populations have a range of stellar masses but on average the stellar masses of the quiescent galaxies are higher in all three redshift ranges. Applying the stellar mass completeness limit clearly narrows the dynamic range of our sample in stellar mass at higher redshifts, particularly for the star forming population. As with the full galaxy population, we do not find any significant correlation between stellar mass and L_X for either the star forming or quiescent host galaxy populations in any of the three redshift ranges. We also find that applying the stellar mass completeness limit and splitting our

sample to star forming and quiescent, the weak trend found above in Figure 2.3 for the middle redshift range now vanishes.

Overall, it appears that the weak positive trend in the first panel of Figure 2.2 is due to a correlation between SFR and L_X in the quiescent host population. Figure 2.6 further shows that this trend is not due to the stellar mass. For the other redshift ranges, we no longer find a significant correlation between SFR and L_X after after applying the stellar mass completeness limit and splitting the sample into the star forming and quiescent host galaxies (although we note that splitting up our sample, in itself, could eliminate any weakly significant trends seen in the full sample).

2.4.3 The fraction of star forming AGN host galaxies

In Section 2.4.1 we found that in the two lowest redshift panels of Figure 2.2 there is a weak but significant positive correlation between SFR and L_X in AGN host galaxies. In Section 2.4.2 we demonstrated that when splitting the sample of these host galaxies into star forming and quiescent, this trend disappeared except for quiescent AGN hosts in the lowest redshift bin. We now investigate whether a change in the fraction of star forming host galaxies, as a function of L_X, could be driving the observed correlation between SFR and L_X for the full AGN host sample. For example, a higher fraction of star forming host galaxies at the most luminous end in Figure 2.2 could create a positive trend in the full sample, as is seen.

We calculate the fraction of X-ray selected AGN with a star forming host galaxy as a function of L_X, where we consider only galaxies above the stellar mass completeness limits. The results are shown in Figure 2.7 in bins of 0.5 dex in L_X, in three redshift ranges. The errors on the fractions are calculated assuming a binomial distribution using the Bayesian method of Cameron (2011) and are equivalent to 1σ uncertainties (68.3% equal-tail confidence intervals). To compare the AGN host galaxies with inactive

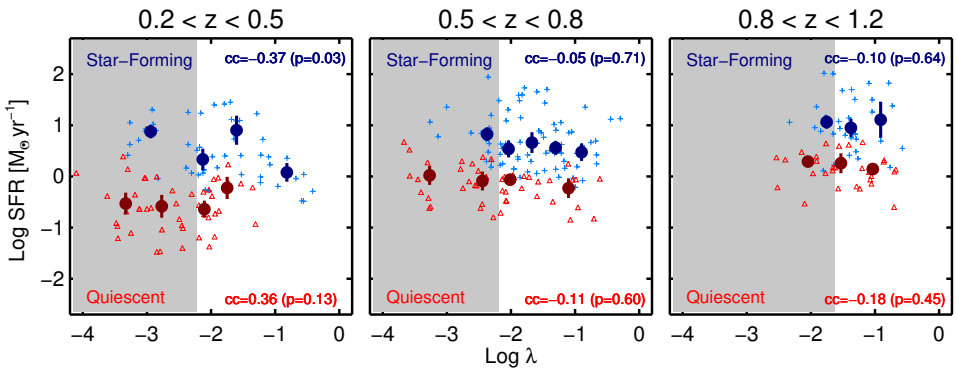

Figure 2.8. The average SFR versus specific accretion rate, in three redshift bins, where the host galaxies are split into star forming (blue plus) or quiescent (red triangle). The errors are measured using bootstrap resampling. Blue and red circles show the median SFR in bins of λ, for the star forming and quiescent host populations, respectively. The grey regions show the area below the specific accretion rate limit; sources in these regions are excluded from the sample. There is no significant correlation between SFR and λ within the quiescent host population. There is a 2σ correlation in the star forming host population in the lowest redshift range that is not seen at higher redshifts.

galaxies in the same redshift range, we show the fraction of entire PRIMUS galaxies above the stellar mass completeness limit that are star forming with green solid lines. Although we find AGN in galaxies with a wide range of stellar mass, they are mainly found in relatively massive galaxies. Furthermore, the median stellar mass of the AGN host galaxies increases from $10^{10.6}$ to $10^{10.8}$ and $10^{10.9}$ $M_{\odot}$ respectively over the three redshift ranges shown in Figure 2.7, primarily due to the increasing stellar mass limit of the PRIMUS sample. For each redshift range we therefore make a sample of stellar mass-matched galaxies that has the same stellar mass distribution as the AGN host galaxies. Then we compare the fraction of AGN within star forming host galaxies with a sample of inactive galaxies with a similar stellar mass and redshift distribution. To construct this sample, we weight each galaxy in a redshift bin such that the weighted distribution of stellar masses matches the stellar mass distribution of the X-ray AGN host galaxies. The fraction of the stellar mass-matched galaxy sample that is star forming is shown with

pink lines in Figure 2.7.

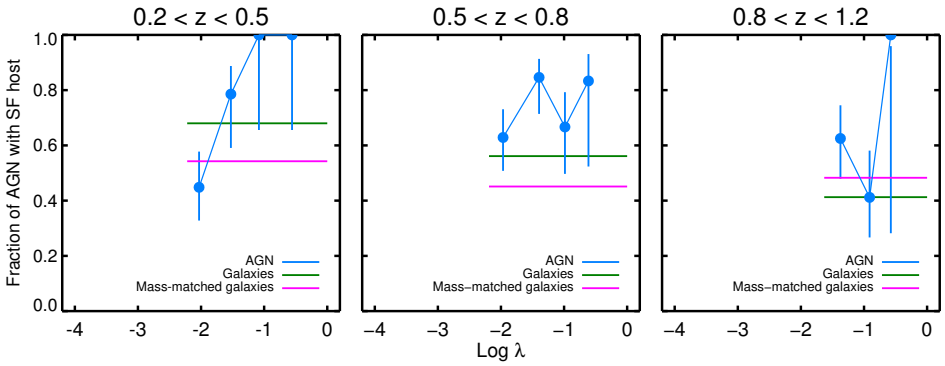

Figure 2.9. Variation of the fraction of AGN in star forming hosts with λ, for the specific accretion rate complete sample, shown with blue lines. The errors are calculated from the binomial distribution using the Bayesian method of Cameron (2011). The green lines show the fraction of all galaxies above the specific accretion rate limits that are star forming, while the pink lines show this fraction for galaxy samples that have the same stellar mass distributions as the AGN host galaxies. The fraction of star forming hosts increases with increasing λ in the lowest redshift. The difference between the fraction of star forming hosts and mass-matched galaxy sample is less than 1σ in the first and last panel and is less than 2σ in the middle panel, confirming that these fractions are not significantly different.

In the lowest redshift range, $0.2 < z < 0.5$, there is a strong apparent trend such that the fraction of X-ray AGN in star forming hosts increases with increasing X-ray luminosities, from $\sim$20% at $L_{\rm X} = 10^{41.5}$ erg s^{-1} to 100% at $L_{\rm X} = 10^{43.5}$ erg s^{-1}. This trend is generally consistent with other studies (e.g. Kauffmann et al. 2003b; Heckman & Kauffmann 2006) in a similar redshift regime that found that low luminosity AGN typically reside in early type galaxies with low star formation activity, while powerful AGN reside in galaxies with young stellar populations. In the middle redshift range, $0.5 < z < 0.8$, the fraction also increases with increasing X-ray luminosity, though not as strongly as at lower redshift. However, in the highest redshift range, $0.8 < z < 1.2$, the fraction declines with X-ray luminosity, over the more limited range spanned by the data at these higher redshifts. However, considering the large error bars, none of these trends

Table 2.1. The fraction of X-ray selected AGN with star forming host galaxies, and the fraction of stellar mass-matched galaxies that are star forming.

Redshift	AGN with SF hosts	SF mass-matched galaxies
$0.2 < z < 0.5$	51±14%	46%
$0.5 < z < 0.8$	62±12%	38%
$0.8 < z < 1.2$	52±17%	43%

are significant.

In an attempt to decrease the error bars, in each redshift range we split the AGN sample into just two equal-width bins in $L_{\rm X}$. In the lowest redshift range, for $41 < \log L_{\rm X} < 42.5$ this fraction is 40±19% and increases to 63±20% at higher luminosities of $42.5 < \log L_{\rm X} < 44$. In the middle redshift range, the fraction increaes from 33±30% to 67±13% in the two luminosity bins. Considering the error bars, neither of these increases is significant.

Table 2.1 lists the overall fraction of AGN host galaxies that are star forming, as well as the fraction of stellar mass-matched galaxies that are star forming, in each redshift range. The variation of the star forming fraction for the stellar mass-matched galaxy sample with redshift is due to the combination of the PRIMUS stellar mass limits (which restrict us to higher stellar masses at higher redshifts), the preference for observed X-ray AGN to be found in more massive galaxies (across all redshifts), and the intrinsic changes in the star forming fraction for galaxies of a given stellar mass with increasing redshift (e.g. Moustakas et al. 2013). The difference in the star forming fraction of AGN host galaxies compared to that of stellar mass-matched galaxies is less than 1σ and therefore is not significant in the lowest and highest redshift bins; however, these fractions are different at the 2σ level in the middle redshift range. The fraction of AGN with star forming host galaxies across our full redshift range of $0.2 < z < 1.2$ is 55±8%, and the fraction of star forming galaxies in the corresponding mass-matched galaxy sample is

44%. Therefore, across our full redshift range, there is not a significant difference in the the fraction of AGN hosted by star forming galaxies and the fraction of star forming galaxies with the same stellar mass distribution.

We find that the fraction of AGN with star forming host galaxies appears to increase with L_X in the two lowest redshift ranges, spanning $0.2 < z < 0.8$, but considering the large error bars the trends observed are not significant. However, the star forming host fraction does increase from $\sim 30\%$ to $\sim 100\%$ as L_X increases, at least in the lowest redshift range, such that the correlation between SFR and L_X observed at $0.2 < z < 0.8$ in Figure 2.2 could be due to the increasing fraction of star forming host galaxies with L_X.

2.4.4 The relationship between SFR and specific accretion rate

In Section 2.4.2 we showed that there is a wide range in the stellar masses of AGN host galaxies for both star forming and quiescent populations. This large scatter could potentially hide an underlying correlation between SFR and specific accretion rate. Therefore we further investigate the dependence of SFR and the star forming host fraction as a function of specific accretion rate, in order to remove any stellar mass dependence. The specific accretion rate, $\lambda \propto L_{bol}/M_*$, traces the rate of accretion scaled relative to the host stellar mass. We calculate the specific accretion rate as

$$\lambda = \frac{L_{bol}}{1.3 \times 10^{38} \mathrm{erg\ s^{-1}} \times 0.002 \frac{\mathrm{M_*}}{\mathrm{M_\odot}}}. \tag{2.5}$$

Thus, λ is a rough tracer of the Eddington ratio, under the assumption that $M_* \approx M_{bulge}$ and $M_{BH} \approx 0.002 M_{bulge}$ (Hunt 2003).

Figure 2.8 shows the SFR versus specific accretion rate of our sample, split into star forming and quiescent host galaxies. Both populations host AGN with a wide range

of specific accretion rate, though the average specific accretion rate in star forming host galaxies is higher than in quiescent host galaxies in all three redshift panels of Figure 2.8. However, the average stellar mass of the star forming galaxies is lower than that of the quiescent galaxies, and we can not detect lower specific accretion rate sources in lower stellar mass host galaxies, because of the X-ray flux limit. To minimize this bias, we first estimate an approximate X-ray luminosity limit in each redshift bin by taking the X-ray luminosity that 90% of the sources exceed (L_{90}). This luminosity limit gives a rough indication of the luminosity below which we are no longer sampling the X-ray AGN population (for a given redshift) and is primarily determined by our deepest field (i.e. the CDFS)[1]. This luminosity limit corresponds to a different limit in specific accretion rate, depending on the mass of the host. To convert to a specific accretion rate limit, we find the stellar mass above which 90% of our X-ray sources lie (M_{90}) in each redshift bin. We convert L_{90} and M_{90} to a limit in specific accretion rate, λ_{90}, using Equation (2.5). We note that M_{90} is higher than our nominal stellar-mass-completeness limits (see Section 2.3.4) due to the fact that our X-ray sources are predominantly found in moderately massive hosts; thus our specific accretion rate limits are *lower* than if our sample all had hosts with masses at the nominal stellar-mass-completeness limit. Above our specific accretion rate limit, we should have a sample that is representative of the X-ray AGN sample. However, we will miss any *lower mass* galaxies with the same accretion rate.

The shaded region in Figure 2.8 illustrates the range of specific accretion rates below this limit, where we will not have a representative sample. Above this limit we calculate the correlation coefficients of individual AGN, both the star forming and quiescent host populations separately, and find that the correlation coefficients are negligible for quiescent host galaxies in all three redshift ranges. Within the star forming host popula-

[1]We note this does *not* correspond to the X-ray completeness corrections calculated with the full X-ray sensitivity curves that are described and applied in Section 2.4.5 to accurately recover the fraction of galaxies that host an AGN of a given specific accretion rate

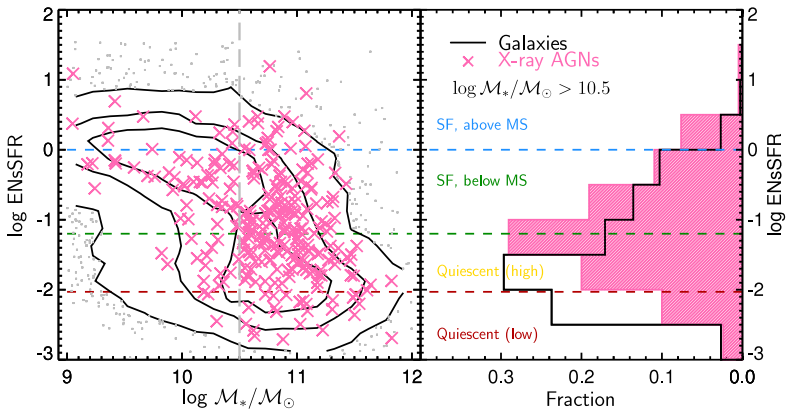

Figure 2.10. *Left:* Epoch-normalized specific star formation rate (*ENsSFR*) versus stellar mass (M_*) for the galaxy sample (black contours) and X-ray AGN (pink crosses) samples considered in Section 2.4.5. The horizontal dashed lines indicate the dividing lines between our four *ENsSFR* bins, as labeled. *Right:* Normalized distributions of *ENsSFR* for the galaxy and X-ray AGN samples, restricted to a stellar mass limit of $\log M_*/M_\odot > 10.5$ (indicated by the vertical dashed grey line in the left panel), where the majority of our X-ray AGN sample are detected and we are complete across our entire redshift range. At these stellar masses the galaxy population is dominated by quiescent galaxies, but the X-ray AGN population is biased towards higher *ENsSFR* sources.

tion, in the lowest redshift range there is a weak negative correlation with a coefficient of -0.37 (p=0.03), such that an increase in the specific accretion rate corresponds to a decrease in the SFR. This trend disappears in the two higher redshift panels.

Figure 2.9 shows the fraction of AGN with a star forming host galaxy as a function of AGN specific accretion rate. Similar to Figure 2.7, this fraction is compared for X-ray AGN host galaxies, all galaxies above the stellar mass limit of the PRIMUS survey, and

Table 2.2. The fraction of X-ray selected AGN with star forming host galaxies, and the fraction of stellar mass-matched galaxies that are star forming, above the specific accretion rate limit.

Redshift	AGN with SF hosts	SF mass-matched galaxies
$0.2 < z < 0.5$	64±18%	54%
$0.5 < z < 0.8$	72±14%	45%
$0.8 < z < 1.2$	55±21%	48%

for galaxy samples with the same stellar mass distribution as the AGN host galaxies. The comparison is done only above the specific accretion rate limit at a given redshift where we will have a representative sample. As before, the error bars on the fractions are from the binomial distribution and are equivalent to 1σ uncertainties. Table 2.2 lists the fraction of AGN host galaxies that are star forming (over all values of $L_{\rm X}$), as well as the fraction of stellar mass-matched galaxies that are star forming, in each redshift range, above our specific accretion rate limit.

We find that the fraction of AGN with star forming host galaxies at $0.2 < z < 0.5$ and $0.8 < z < 1.2$ above our specific accretion rate limits are not significantly different ($< 1\sigma$) to the fraction of star forming galaxies in the mass-matched galaxy sample. In the middle redshift range ($0.5 < z < 0.8$), there is a 1.9σ difference. Figure 2.9 shows that the fraction of AGN in star forming host galaxies may increase with specific accretion rate in the lower redshift range. In the higher two redshift ranges this fraction appears to be roughly constant. These trends are generally consistent with what was found in Figure 2.7, as a function of $L_{\rm X}$, but our limited sample size means we do not have a high significance result and thus these trends should be treated with caution.

To summarize, when we re-examine trends with SFR and the specific accretion rate (rather than $L_{\rm X}$) within our X-ray AGN sample, we do not find any highly significant ($> 3\sigma$) correlations that were previously missed. Furthermore, the 3σ correlation between SFR and $L_{\rm X}$ for quiescent host galaxies that was seen in the first panel of Figure 2.5 is no longer found when we renormalize $L_{\rm X}$ by the stellar mass (Figure 2.8). We note that applying the specific accretion rate limits has reduced our sample size and thus could be why we no longer find a significant correlation. However, overall we conclude that there is no evidence for a correlation between SFR and specific accretion rate for either star forming or quiescent host galaxies within the X-ray AGN population.

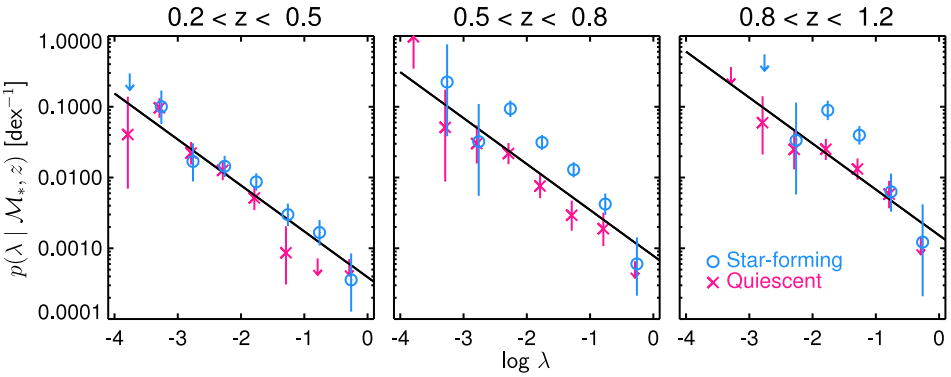

Figure 2.11. The probability density for a galaxy of given stellar mass, M_*, and redshift, z, to host an AGN of specific accretion rate, λ, here dividing the galaxy sample into star forming and quiescent populations according to Equation (2.4). The thick black line corresponds to the best-fit power-law relationship measured by A12 for the overall galaxy population, evaluated at the center of the given redshift bin. Blue (red) points are estimated using the $N_{\rm obs}/N_{\rm mdl}$ method considering the star forming (quiescent) galaxy populations only, but with reference to this overall model that allows us to account for the underlying redshift evolution, stellar-mass-dependent selection effects, and the X-ray completeness. We see that at all redshifts the probability of a galaxy hosting an AGN depends strongly on specific accretion for both star forming and quiescent galaxy populations (rising towards low values of λ) but is a factor $\sim 2-3$ higher in star forming galaxies than in quiescent galaxies at any given λ.

2.4.5 The probability of a galaxy hosting an AGN as a function of star formation rate

In the above analysis we consider a sample of AGNs selected based on their X-ray emission, investigate the correlation between the SFR of the host galaxy and the AGN luminosity, and measure the fraction of these X-ray AGNs with hosts that are star forming versus quiescent. In this section we take an alternative approach (based on the approach of Aird et al. 2012, hereafter A12): we select samples of galaxies with a specified range of properties (in our case, a particular range of SFR) and determine the probability of finding an AGN in such galaxies. Our galaxy sample consists of all PRIMUS galaxies with stellar masses above the (redshift-dependent) completeness limits defined in Section 2.3.4. For this analysis we do not include galaxies or X-ray AGNs from the CDFS field; this field was a PRIMUS calibration field and the targeted galaxy sample is not defined in the same, consistent manner as the PRIMUS science fields. Thus, we are unable to accurately determine the probability of a galaxy hosting an AGN for the CDFS field.

We divide the galaxy sample according to the epoch-normalized specific SFR (ENsSFR), or the ratio of the sSFR to that of the main-sequence of star formation at the redshift of the galaxy, that we defined in Section 2.4.2 (see Equation (2.4)). By working with the $ENsSFR$ we can remove both the dependence of SFR on stellar mass and the overall evolution of the star forming main sequence over our redshift range. Figure 2.10 (left panel) shows the distribution of $ENsSFR$ (as a function of stellar mass) for the galaxy and X-ray AGN samples we consider here, along with dividing lines between our populations. The horizontal green dashed line divides the quiescent and star forming galaxy populations, corresponding to the same $ENsSFR$ cuts used in Section 2.4.2 (logENsSFR$= -1.2$). We also define two further divisions, corresponding to the peak of the star forming main sequence (at $\log ENsSFR = 0$, by definition) and the peak of the quiescent galaxy population (at $\log ENsSFR = -2.01$). These lines allow us to

further sub-divide our galaxy sample into four populations: quiescent galaxies with low SFRs, quiescent galaxies with higher SFR, star forming galaxies below the star forming main sequence, and star forming galaxies above the star forming main sequence.

The right panel of Figure 2.10 shows the distribution of *ENsSFR* for the galaxy and X-ray AGN samples, above a mass limit of $\log \mathrm{M}_{*}/\mathrm{M}_{\odot} > 10.5$ where the bulk of our X-ray detections lie and our galaxy sample is complete over the majority of the $0.2 < z < 1.2$ redshift range. We note that at these masses there is no clear bimodality in the galaxy population. Nonetheless, the X-ray AGNs show a distribution that is skewed towards higher *ENsSFR* than that of the galaxies. This appears consistent with the findings of Section 2.4.2, where we found weak evidence for a higher fraction of X-ray AGNs to be found in star forming galaxies (i.e. at higher ENsSFR) compared to galaxies of equivalent stellar mass.

To accurately determine the probability of a galaxy hosting an AGN we must correct for a number of sources of incompleteness in our X-ray selected AGN population. These effects are ultimately due to the (varying) flux limit of the X-ray observations. The X-ray flux limit means that lower luminosity sources will not be identified at higher redshifts over the entire survey area, thus we must upweight any sources we *do* detect. A12 also showed that probability of a galaxy hosting AGN is given by a power-law distribution of specific accretion rate (λ), where lower λ sources are more common than high λ sources in galaxies of all stellar masses (see also Bongiorno et al. 2012). However, as λ scales with the host stellar mass, AGNs with the same λ in a lower stellar mass host would have a lower observed X-ray luminosity, and thus may fall below our flux limits and be under-represented in our X-ray selected sample.

To account for these effects, we take the global relation from A12 for the probability density of a galaxy of given M_{*}, and redshift, z, hosting an AGN of specific accretion

rate, λ, per unit logarithmic λ, given by

$$p(\lambda \mid \mathrm{M}_*, \mathrm{z})\, \mathrm{d}\log \mathrm{L_X} = \mathrm{A}\lambda^{\gamma_\mathrm{E}} \left(\frac{1+\mathrm{z}}{1+\mathrm{z}_0}\right)^{\gamma_\mathrm{z}} \mathrm{d}\log\lambda \tag{2.6}$$

where $z_0 = 0.6$ and the other parameters are given in table 3 of A12. We use this relation, combined with the X-ray selection function, as a model to predict the observed number of X-ray AGN within one of our sub-samples of the galaxy population. Thus, the predicted number of X-ray AGN within one of our sub-samples of the galaxy population is

$$N_\mathrm{mdl} = \sum_{k=1}^{N_\mathrm{samp}} \int p(\lambda \mid \mathrm{M_k}, \mathrm{z_k})\, \mathrm{p_{det}}\left(\mathrm{f_X}(\lambda, \mathrm{M_k}, \mathrm{z_k})\right)\, \mathrm{d}\log\lambda \tag{2.7}$$

where the summation is performed over all N_samp galaxies in our sub-sample, $\mathrm{M_k}$ and z_k are the stellar masses and redshifts of each galaxy, and $p_\mathrm{det}\left(f_\mathrm{X}(\lambda, \mathrm{M_k}, \mathrm{z_k})\right)$ is the probability of detecting an X-ray source with flux f_X.

We calculate the X-ray flux, f_X, by converting λ into a bolometric luminosity (given the stellar mass, $\mathrm{M_k}$, of the galaxy under consideration), which we then convert into an X-ray luminosity (using the bolometric corrections of Hopkins et al. 2007), and finally convert to an X-ray flux given the redshift of the galaxy, z_k. The dependence of p_det on flux is determined by the X-ray sensitivity curves, calculated in Section 4.1 of A12. We use the ratio of this predicted number of X-ray AGNs to the actual observed number, N_obs, in a given galaxy sub-sample to rescale the prediction for $p(\lambda \mid \mathrm{M}_*, \mathrm{z})$ from the A12 model at the centre of bin of given redshift and λ (based on the method of Miyaji et al. 2001). Errors on the binned estimates are based on the Poisson error given the observed number of X-ray AGNs (taken from Gehrels 1986). This method allows us to account for underlying variations of the model, the X-ray completeness, and the stellar mass and redshift distribution of the galaxy sample within a given bin.

In Figure 2.11 we present binned estimates of $p(\lambda \mid \mathrm{M}_*, \mathrm{z})$ using the method described above for three redshift bins, dividing the galaxy sample into the quiescent (red crosses) and star forming (blue circles) populations based on our *ENsSFR* cut. The black line indicates the underlying power-law model of A12. We see a clear difference between the estimates for the star forming and quiescent populations at all redshifts, whereby the probability of finding an AGN (of fixed λ) is higher in a star forming galaxy than for a quiescent galaxy. This difference is more significant at higher redshifts ($z > 0.5$), where the star forming population lies above the global relation of A12. Both populations, however, appear to be consistent with the overall power-law shape of the distribution measured by A12; one type of galaxy population is not primarily associated with the most rapidly accreting sources. The overall increase in the probability of finding an AGN as redshift increases is also seen for both populations.

In Figure 2.12 we combine our data over the entire $0.2 < z < 1.2$ redshift range but further subdivide our galaxy population into the four bins of *ENsSFR* shown in Figure 2.10. The underlying redshift evolution across this wide bin is corrected for by our $N_{\mathrm{obs}}/N_{\mathrm{mdl}}$ using the A12 model. We again see that $p(\lambda \mid \mathrm{M}_*, \mathrm{z})$ has a fairly consistent power-law shape across the populations but the overall normalization increases moving across the quiescent population (from low to high SFR).

However, the normalization appears roughly constant across the star forming population. To investigate these trends in more detail, we use our $N_{\mathrm{obs}}/N_{\mathrm{mdl}}$ method to estimate $p(\lambda \mid \mathrm{M}_*, \mathrm{z})$ for a wide $-3 < \log\lambda < -1$ bin for each of the four populations (scaling relative to the A12 model evaluated at $\lambda = 0.01$). We show these estimates as a function of *ENsSFR* as the colored points in Figure 2.13. The light grey points also show estimates for 8 fixed width bins of log ENsSFR. We confirm an increase (at 4σ significance) in the normalization of $p(\lambda \mid \mathrm{M}_*, \mathrm{z})$ with *ENsSFR* across the quiescent population, which increases further (by a further factor 1.7 ± 0.3) to higher *ENsSFR* (into

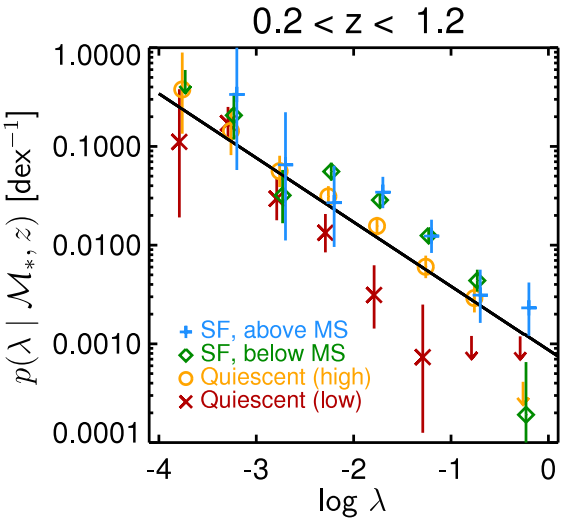

Figure 2.12. The probability density for a galaxy to host an AGN of specific accretion rate λ, dividing the galaxy sample into four populations according to their epoch-normalized specific star formation rates (ENsSFRs). We consider a sample spanning the entire $0.2 < z < 1.2$ redshift range but account for the overall evolution in $p(\lambda \mid \mathrm{M}_*, \mathrm{z})$ according to the best-fit model of A12. The solid black line shows this best fit model evaluated at the center of the redshift bin($z = 0.7$) and points are calculated using the $N_{\rm obs}/N_{\rm mdl}$ relative to this model, for each *ENsSFR* bin. The shape of $p(\lambda \mid \mathrm{M}_*, \mathrm{z})$ remains roughly the same but the normalization increases moving from the quiescent populations to galaxies below or above the star forming main sequence (see also Figure 2.13).

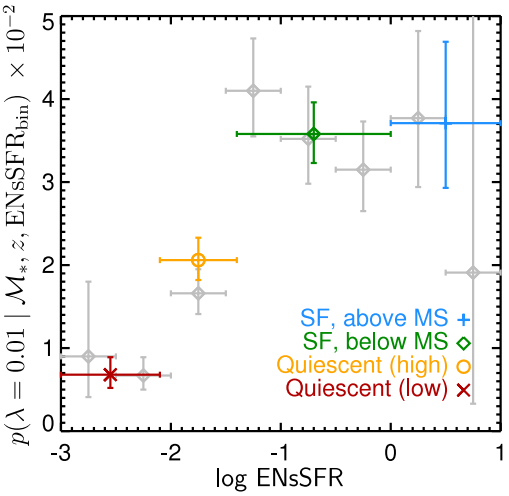

Figure 2.13. The probability density of a galaxy hosting an AGN, $p(\lambda \mid \mathrm{M}_*, \mathrm{z})$, evaluated at $\lambda = 0.01$ and $z = 0.7$, as a function of epoch-normalized specific star formation rate (*ENsSFR*). Colored points correspond to bins defined relative to the star forming main sequence (as used in Figure 2.12), whereas the light grey points are for evenly spaced, 0.5 dex wide bins of ENsSFR. The estimates use data from the entire $0.2 < z < 1.2$ redshift range and $-3 < \log\lambda < -1$, but the plotted values are estimated at $\lambda = 0.01$ and $z = 0.7$ using the $N_{\mathrm{obs}}/N_{\mathrm{mdl}}$ method (relative to the A12 model). We see that the probability of a galaxy hosting an AGN rises with *ENsSFR* over the quiescent galaxy population but appears to flatten off for galaxies around the star forming main sequence.

the star forming galaxy population), where it appears to reach a plateau.

Overall, our results show that the probability of a galaxy hosting an AGN is higher for galaxies on the star forming main sequence. The probability of hosting an AGN drops for galaxies below the main sequence, where the star formation rates are lower. Nonetheless, AGNs are found in all types of galaxies and appear to have a similar overall distribution of accretion rates. Our results indicate that about 1–2% of quiescent galaxies at $z \sim 0.6$ host an AGN with an accretion rate of at least 1% of Eddington. This rises in sources with higher SFRs and $\sim 3.5\%$ of star forming galaxies host an AGN with an accretion rate of at least 1% of Eddington.

2.5 Discussion

2.5.1 Is there a correlation between SFR and AGN luminosity?

In this paper we investigate the relationship between SFR and AGN luminosity, using L_X, and generally find that these two quantities are not strongly correlated within moderate-luminosity X-ray selected AGN samples. There is a large scatter in SFR at any given L_X and more powerful AGN are not necessarily in more highly star forming galaxies. We find evidence for a weak correlation between SFR and L_X in our full sample of both star forming and quiescent host galaxies at $z < 0.8$. However, under further investigation we conclude this is likely due to 1) a weak correlation between SFR and L_X in low redshift quiescent host galaxies; we do not find a similar trend in star forming host galaxies at these redshifts, and/or 2) the fact that AGN with higher L_X are more likely to have a star forming host galaxy (e.g. Kauffmann et al. 2003b; Heckman & Kauffmann 2006), though our error bars are too large to measure this with significance. We note that the SFR-L_X correlation observed in the full sample at $0.5 < z < 0.8$ vanishes when we investigate the correlation for star forming and quiescent host galaxies separately. This further indicates that correlations seen for the full sample may be due to the changing mix of star forming and quiescent hosts as a function of L_X, rather than a correlation between SFR itself and L_X. We confirm that none of the observed trends between SFR and L_X are driven by an underlying correlation between L_X and stellar mass within our AGN sample. While we find that the mean AGN host stellar mass is $\log \frac{M_*}{M_\odot} \sim 10.5$, there is a wide distribution in host galaxy stellar mass throughout our L_X range, consistent with (e.g. Aird et al. 2012; Bongiorno et al. 2012). We also find a large scatter in specific accretion rate for both star forming and quiescent host galaxies, which could explain the lack of a direct correlation between SFR and L_X. In fact, for the low redshift quiescent host galaxies where we do find a significant correlation between SFR and L_X, we do not

find a correlation between SFR and specific accretion rate.

Overall, within the sample of AGN with star forming host galaxies, we do not find significant correlations between SFR and AGN luminosity. This is consistent with an emerging picture where the instantaneous BH accretion rate (e.g. Chen et al. 2013; Hickox et al. 2014) is decoupled from the current rate of star formation, at least in galaxies hosting moderate luminosity AGN (e.g. Mullaney et al. 2012b; Rosario et al. 2012; Harrison et al. 2012; Rovilos et al. 2012). A possible scenario for BH fueling in low to moderate luminosity AGN is that it is driven by stochastic infall of cold gas from circumnuclear regions (e.g. Kauffmann & Heckman 2009b). In fact star formation in most "main sequence" star forming galaxies appears to be driven by internal processes, e.g. disk instabilities and turbulence (e.g. Elbaz et al. 2007a; Daddi et al. 2010). Therefore, rather than there being a direct connection between star formation and AGN activity, these two processes likely share a common gas supply. However, there are studies that find a correlation between SFR and L_X in star forming galaxies that host powerful AGN, both at at $z < 1$ (e.g. Rosario et al. 2012) and $z > 1$ (e.g. Rovilos et al. 2012; Netzer et al. 2013). There is also some evidence in LIRGS that indicates highly star forming galaxies are more likely to host AGN (e.g. Iwasawa et al. 2011). As major merger events likely play an important role in fueling the most luminous AGN and starburst galaxies, then the incidence of major mergers could lead to a more direct correlation between SFR and AGN luminosity at high L_X.

Our sample at $0.2 < z < 1.2$ also includes quiescent galaxies, for which we are able to estimate SFRs. This contrasts with studies that rely on far-IR data from *Herschel*, as quiescent galaxies are not detected at these redshifts. Interestingly, we find a significant correlation between SFR and L_X in quiescent host galaxies at $z < 0.5$. This correlation could be interpreted as evidence of a direct coupling between SFR and L_X in quiescent galaxies, for example due to a common cold gas supply. It could illustrate a different

triggering mechanism (e.g. minor mergers or other secular processes) than that in star forming galaxies, which channels cold gas into the central regions.

We note that as our results rely on UV-optical SED fits, we could underestimate the level of dust (and therefore SFR) in a fraction of our galaxies. This could potentially introduce a bias that might hide an underlying correlation. Additionally, our SED templates do not include an AGN component; however, we have removed sources with broad lines in their optical spectra, and for our sample the light is clearly dominated by the host galaxy. If there was any residual blue light from an AGN, this would decrease our estimated SFRs. Unaccounted for, this could potentially introduce an observed correlation between SFR and L_X that does not exist; this could be happening in our low redshift quiescent host galaxies. Finally, our sample is limited to some extent by statistics and a larger and deeper sample would be helpful.

2.5.2 Average X-ray luminosity versus SFR

While we do not find a direct correlation between SFR and instantaneous X-ray luminosity in star forming host galaxies, these processes could still be connected through a common triggering and fueling mechanism. Due to a stochastic fueling process, accretion activity onto the SMBH is time variable (e.g. Ulrich et al. 1997; Peterson 2001) and AGN luminosities may drop more than 10^2 in less than 10^5 years (Keel et al. 2012b). Additionally, recent studies found [OIII] emission from ionized clouds in the outskirt of galaxies with little or no evidence of on-going AGN activity (e.g. Schawinski et al. 2010; Keel et al. 2012a,b), confirming that AGN illuminating these clouds were much brighter in the past. In contrast, star formation remains stable for a longer period of time; even in starburst galaxies this process can last $\sim$100 Myrs (e.g. Wong 2009; Hickox et al. 2012). Due to the rapid variability of AGN, using an instantaneous AGN luminosity to compare with SFR may hide an underlying connection between AGN and

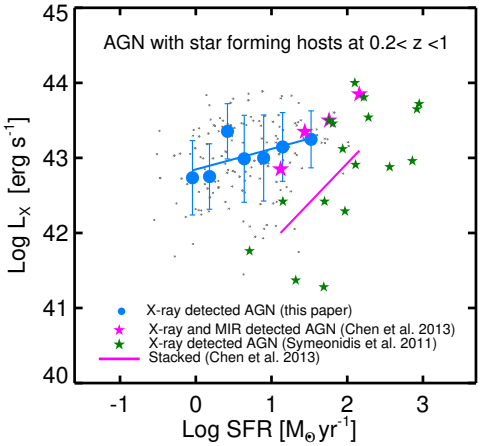

Figure 2.14. X-ray luminosity versus SFR in star forming host galaxies at redshift $0.2 < z < 1.0$. Gray points are PRIMUS individual X-ray detected AGN, while blue circles show the average L_X in bins of SFR. The error bars on each median point reflect the standard deviation. The blue solid line shows the best fitted line to the median points. We find a weak positive correlation with the coefficient of 0.24 (p= 0.00) between the average L_X and SFR in our AGN sample. The median redshift in each bin of SFR indicates our correlation is not due to evolution of SFR with redshift. The pink stars are the detected AGN in Chen et al. (2013), while the pink solid line indicates their average sample which also includes X-ray stacks of all galaxies. The green stars are X-ray detected AGN from Symeonidis et al. (2011a), showing LIRG and ULIRG galaxies at $z \sim 1$.

star formation. Instead, using an average AGN luminosity may be more appropriate to explore relationships between AGN and their host galaxies (e.g. Chen et al. 2013; Hickox et al. 2014). Recently, Chen et al. (2013) used the average AGN luminosity and found that the SMBH accretion rate is directly linked to the SFR in star forming galaxies at $z \sim 0.5$.

Here we use our sample of 167 X-ray detected AGN hosted by star forming galaxies at $0.2 < z < 1$ to consider the relation between the average L_X and SFR. We also compare our results with Chen et al. (2013) (hearafter C13). Since we use SED fits with UV and optical bands to estimate SFRs and C13 use *Herschel*/SPIRE 250 μm measurements, we use Equation (2.1) to convert their estimated IR luminosity to SFR for

comparison. Figure 2.14 shows L_X for our sample plotted as a function of SFR. Gray points indicate individual X-ray detected AGN, while blue circles show the average L_X of the gray points in bins of SFR. Error bars on each median point reflect the standard deviation in that bin. The blue solid line shows the best fitted line to our median points, using a non-linear least square fit. We emphasize that this line is for X-ray detected AGN only.

Pink stars show detected AGN in the C13 sample, which includes 34 X-ray detected AGN (using *Chandra* ACIS-I 5 ks observations with $L_{X0.5-7kev}$) and 87 MIR detected AGN (using $4.5\mu m$ observation from *Spitzer*) in star forming galaxies in the Boötes field at $0.25 < z < 0.8$. From AGN detected in both X-rays and the MIR, C13 used the median $\frac{L_X}{L_{IR}}$ to estimate the L_X for MIR detected AGN. The solid pink line shows the average L_X found for both detected and undetected AGN, where C13 stacked the X-ray emission around active and non-active galaxies, removing the contribution from XBs in the X-ray stack. The green stars show X-ray detected AGN in Symeonidis et al. (2011a), which includes 17 LIRG and ULIRG galaxies at $z \sim 1$, from the 2 Ms observations in the CDFN.

In our detected AGN sample, there is a slight but significant trend here with a correlation coefficient of 0.24 (p= 0.00) between the average L_X and SFR. This is somewhat shallower than the trend in the C13 detected AGN sample, but where the samples overlap there is good agreement. C13 are not able to detect AGN with $L_X \lesssim 10^{43}$ erg s^{-1} due to their shallower X-ray data, therefore their points do not probe to as low SFR as our sample. Since the total X-ray area of PRIMUS is smaller than the area probed by C13, and BLAGN are not included in this study, our sample lacks the highly star forming galaxies above $\log(\frac{SFR}{M_\odot yr^{-1}}) \sim 1.5$.

We note that the trends shown in C13 for both the detected and average samples are affected by redshift. Once corrected for the evolution of the X-ray luminosity function

and SFR with redshift, C13 find a shallower trend that is highly consistent with our result. To investigate whether evolution may have an effect on the trend observed in our sample, we find the median redshift in each bin of SFR. We do not have a significant redshift-dependence in our SFR bins, such that our correlation is not impacted by evolution. X-ray selected AGN from Symeonidis et al. (2011a) confirm the correlation between $L_{\rm X}$ and SFR found in C13, although this sample only includes AGN in higher SFR sources (LIRGs and ULIRGs). Furthermore deeper X-ray data may provide greater dynamic range in $L_{\rm X}$ revealing a steeper trend. Our sample includes lower SFR sources but it does not probe as deep in X-ray luminosity and therefore is difficult to compare directly with the Symeonidis et al. (2011a) sample.

Overall, our sample of X-ray detected AGN shows a large scatter in $L_{\rm X}$ at a given SFR, though we find a weak but significant correlation between them. This correlation indicates that the rate of black hole growth is related to the SFR in star forming galaxies, when effectively averaging black hole growth over long timescales, consistent with stochastic fueling of the AGN from the same ultimate fuel supply as that for star formation. While here we averaged only our X-ray detected sources, ideally we would want to take the average over the entire galaxy sample. To do this properly we would need to stack our galaxy sample, which is beyond the scope of this paper. We also note that the X-ray flux limit of our survey impacts the correlation that we find and that with deeper X-ray data we would be able to investigate this correlation more precisely.

2.5.3 Where do AGN live?

In our study, we find a large scatter between SFR and $L_{\rm X}$, with little evidence of a direct correlation, when considering X-ray selected AGN with either star forming or quiescent host galaxies. However, our results from Section 2.4.5 indicate that, when considering the entire galaxy population, one is more likely to find an AGN in a star

forming galaxy. Within either the star forming or quiescent galaxy populations, we find AGNs with a wide range of specific accretion rates, described by a roughly power-law distribution. However, for a given λ, the probability of a star forming galaxy hosting an AGN is higher than for a quiescent galaxy. Enhanced AGN activity in star forming galaxies has also been seen in several recent studies (e.g. Silverman et al. 2009; Mullaney et al. 2012b; Aird et al. 2012; Rovilos et al. 2012; Rosario et al. 2012). The differences in the distributions can either be interpreted as an increased probability of AGN activity being triggered in galaxies with large reservoirs of cold gas (that also fuel star formation), or that AGNs in such galaxies are accreting, *on average*, at higher rates (see also Georgakakis et al. 2014a).

These findings are consistent with the picture discussed above, where the level of AGN accretion in a given galaxy can vary substantially over short time periods (relative to the star formation timescales), and could explain that lack of a strong, direct correlation between SFR and $L_{\rm X}$: while the overall probability of hosting an AGN is higher for higher SFRs, the instantaneous accretion rate that we observe from a single galaxy can vary over many orders of magnitude, washing out any direct correlation between the SFR and $L_{\rm X}$.

While this is appealing, it is important to note where our results do not fit in with this simple picture. Firstly, we do find AGNs in quiescent galaxies that may have very low levels of star formation and the distribution has a similar power-law shape (albeit shifted to lower λ), indicating that the underlying physical processes that regulate AGNs may be similar in quiescent galaxies to those taking place in star forming galaxies (although ultimately the large scale fueling processes may be different). Secondly, we do not find a rise in the probability of hosting an AGN with SFR *within* the star forming galaxy population itself, indicating that increased star formation does not go hand-in-hand with increased (average) BH growth. Conversely, for quiescent galaxies with reduced SFRs

–placing them below the main sequence of star formation– we find that the probability of hosting an AGN is decreased by a factor $\sim 2-3$. Furthermore, as SFRs decrease *within* the quiescent population we find that the probability of hosting an AGN also decreases, indicating that as star formation is shut down there is also a reduction of AGN activity in quiescent galaxies. Nevertheless, as emphasized above, AGNs are still widespread within quiescent galaxies, with a wide range of specific accretion rates.

We note that the number of bins we used to classify our host galaxies is limited by our sample size, and with the current binning we do not have a sufficiently large sample to directly measure the shape of $p(\lambda \mid \mathrm{M}_*, \mathrm{z})$ within each bin. Larger samples would allow us to accurately track changes in the distribution of specific accretion rate as a function of the host galaxy properties and would shed light on any change in the underlying physical processes.

2.6 Summary

In this paper we study the relationship between AGN X-ray luminosity and their host galaxies' SFR and stellar mass. We use a sample of 309 X-ray selected AGN with spectroscopic redshifts from the PRIMUS survey at $0.2 < z < 1.2$. We exclude BLAGN to minimize the contribution of AGN light when estimating host galaxy properties, and we include AGN with $10^{41} < L_{\mathrm{X}} < 10^{44}$ erg s^{-1}. Our main conclusions are as follows:

- Star formation rate and AGN luminosity are not strongly correlated within our X-ray AGN sample at $0.2 < z < 1.2$. There is a wide range of SFRs at a given L_{X}, and a higher L_{X} does not necessarily imply a higher SFR. We do not find any significant correlation between SFR and L_{X} in star forming host galaxies, though we do find a weak but significant correlation between the mean L_{X} of detected AGN and SFR. This correlation implies an underlying connection that may exist

due to a common gas supply but the variability of AGN accretion on relatively short timescales makes it hard to observe.

- AGN with a wide range of L_X reside in both star forming and quiescent galaxies with a wide range of stellar masses, although are generally found in moderately massive ($\gtrsim 10^{10} M_\odot$) galaxies. However, we do not find any correlation between stellar mass and L_X within our X-ray AGN sample for either the star forming or quiescent host populations.

- We find a wide range of specific accretion rates, λ (L_X normalized by host stellar mass), across the star forming and quiescent host populations, which could explain the lack of a stronger correlation between SFR and L_X.

- The fraction of AGN residing in star forming host galaxies increases with increasing AGN X-ray luminosity, indicating that more powerful AGN are mainly hosted in star forming galaxies at $z < 1$.

- The probability that a galaxy of a given stellar mass, M_*, and redshift, z hosts an AGN as a function of specific accretion rate, $p(\lambda \mid M_*, z)$, is roughly a power law for both star forming and quiescent host galaxies. The probability of hosting an AGN at a given specific accretion rate is higher for star forming galaxies than quiescent galaxies. Furthermore, this probability increases with SFR within the quiescent galaxy population, though within the star forming population there is no change across the "main sequence" of star formation.

Within star forming galaxies, known to contain abundant cold gas, we find no direct correlation between SFR and instantaneous AGN activity, although the overall probability of hosting an AGN is higher than in quiescent galaxies. Conversely, in quiescent host galaxies, where the overall probability of finding an AGN is somewhat

lower, we do find evidence for a correlation between SFR and AGN instantaneous luminosity which may suggest different triggering and fueling processes (e.g. minor mergers, secular processes) drive both star formation and AGN activity in such galaxies. However, the distribution of accretion rates in both star forming and quiescent galaxies has a similar approximately power-law form, indicating that AGN accretion is ultimately a stochastic process and that the same physical processes may regulate AGN activity once gas is funneled to the central few parsecs.

2.7 Acknowledgements

We thank the referee for their positive comments and constructive advice which helped improving this paper. We also thank Ramin Skibba and Aleks Diamond-Stanic for helpful discussions and comments on the paper. We acknowledge Rebecca Bernstein, Adam Bolton, Douglas Finkbeiner, David W. Hogg, Timothy McKay, Sam Roweis, and Wiphu Rujopakarn for their contributions to the PRIMUS project.

We thank the CFHTLS, COSMOS, DLS, and SWIRE teams for their public data releases and/or access to early releases for the PRIMUS survey. This paper includes data gathered with the 6.5m Magellan Telescopes located at Las Campanas Observatory, Chile. We thank the support staff at LCO for their help during our observations, and we acknowledge the use of community access through NOAO observing time. Some of the data used for this project are from the CFHTLS public data release, which includes observations obtained with MegaPrime/MegaCam, a joint project of CFHT and CEA/DAPNIA, at the Canada- France-Hawaii Telescope (CFHT) which is operated by the National Research Council (NRC) of Canada, the Institut National des Science de l'Univers of the Centre National de la Recherche Scientifique (CNRS) of France, and the University of Hawaii. This work is based in part on data products produced at TERAPIX and the Canadian Astronomy Data Centre as part of the Canada- France-Hawaii Telescope Legacy Survey, a

collaborative project of NRC and CNRS. We also thank those who have built and operate the Chandra and XMM-Newton X-ray observatories. Funding for PRIMUS has been provided by NSF grants AST-0607701, 0908246, 0908442, and 0908354, and NASA grant 08-ADP08-0019. MA and ALC acknowledge support from NSF CAREER award AST-1055081. J.A. acknowledges support from a COFUND Junior Research Fellowship from the Institute of Advanced Study, Durham University.

Chapter 2, in full, is a reprint of the material as it appears in The Astrophysical Journal 2015. Azadi, M., Aird, J., Coil, A., Moustakas J., Mendez, A., Blanton, M., Cool, R., Eisenstein, D., Wong, K., Zhu G. 2015. The dissertation author was the primary investigator and author of this paper.

Chapter 3

The MOSDEF Survey: AGN Multi-Wavelength Identification, Selection Biases And Host Galaxy Properties

3.1 Abstract

We present results from the MOSFIRE Deep Evolution Field (MOSDEF) survey on the identification, selection biases, and host galaxy properties of 55 X-ray, IR and optically-selected active galactic nuclei (AGN) at $1.4 < z < 3.8$. We obtain rest-frame optical spectra of galaxies and AGN and use the BPT diagram to identify optical AGN. We examine the uniqueness and overlap of the AGN identified at different wavelengths. There is a strong bias against identifying AGN at any wavelength in low mass galaxies, and an additional bias against identifying IR AGN in the most massive galaxies. AGN hosts span a wide range of star formation rate (SFR), similar to inactive galaxies once stellar mass selection effects are accounted for. However, we find (at $\sim 2-3\sigma$ significance) that IR AGN are in less dusty galaxies with relatively higher SFR and optical AGN in dusty galaxies with relatively lower SFR. X-ray AGN selection does not display a bias with host galaxy SFR. These results are consistent with those from larger studies at lower redshifts. Within star-forming galaxies, once selection biases are accounted for, we find AGN in galaxies with similar physical properties as inactive galaxies, with no evidence

for AGN activity in particular types of galaxies. This is consistent with AGN being fueled stochastically in any star-forming host galaxy. We do not detect a significant correlation between SFR and AGN luminosity for individual AGN hosts, which may indicate the timescale difference between the growth of galaxies and their supermassive black holes.

3.2 Introduction

Active galactic nuclei (AGN) are the result of accretion of gas and dust onto the supermassive black holes (SMBHs) at the centers of galaxies and have been investigated in numerous studies during the past two decades (for a recent review of black hole growth see Alexander & Hickox 2012). Various observational results have shown evidence for a global connection between the growth of SMBHs and the galaxies in which they live. For example, the relatively tight correlation between the SMBH mass and the bulge stellar mass (e.g. Magorrian et al. 1998) or bulge velocity dispersion (e.g. Ferrarese & Merritt 2000; Gebhardt et al. 2000; Kormendy et al. 2011) supports the idea of a close connection between the growth of SMBHs and their host galaxies. In addition, the similar evolution of the SMBH accretion rate density and star formation rate (SFR) density with redshift indicates a global connection between AGN activity and the formation of stars in galaxies (e.g. Boyle & Terlevich 1998; Silverman et al. 2008; Aird et al. 2010; Assef et al. 2011). However, the details of the coeval growth of galaxies and their SMBHs are not well understood.

Accretion onto SMBHs releases a tremendous amount of energy, and thus AGN produce significant radiation at X-ray, ultraviolet (UV), optical, infrared (IR), and radio wavelengths. Different studies have used emission at one or more of these wavelengths to identify AGN and subsequently investigate the nature of their host galaxies (e.g. Kauffmann et al. 2003a; Goulding & Alexander 2009; Kauffmann & Heckman 2009a; Aird et al. 2012; Mendez et al. 2013; Azadi et al. 2015; Cowley et al. 2016; Harrison

et al. 2016).

One of the most reliable methods of identifying AGN is X-ray imaging from deep surveys carried out with the *XMM-Newton*, *Chandra* and, more recently, *NuSTAR* telescopes (for a recent review see Brandt & Alexander 2015). The X-ray emission from AGN is strong enough to outshine the X-ray light associated with intense star formation activity and penetrate regions with high hydrogen column density (up to $N_H \approx 10^{23-24}$ cm^{-2}). Thus, hard-band (2–10 keV) X-ray selection is sensitive to both unabsorbed and moderately absorbed AGN, and is relatively unaffected by host galaxy dilution.

However, X-ray emission is strongly absorbed by Compton thick regions with hydrogen column density of $N_H > 1.5 \times 10^{24}$ cm^{-2} (e.g. Della Ceca et al. 2008; Comastri et al. 2011; Brightman et al. 2014). Studies of local and non-local AGN samples estimate that 10–50% of the entire AGN population are Compton thick (e.g. Akylas & Georgantopoulos 2009; Vignali et al. 2010; Alexander et al. 2011; Lanzuisi et al. 2015; Buchner et al. 2015), demonstrating that such heavily obscured sources represent a sizable fraction of the full AGN population. Also X-ray identification is not successful in identifying less powerful AGN that are accreting at very low rates (e.g. Gilli et al. 2007; Aird et al. 2012) or AGN residing in less massive galaxies (e.g. Mendez et al. 2013).

For heavily obscured AGN that cannot be recovered by X-ray imaging, identification at other wavelengths may be used. The obscuring dust absorbs the UV and optical radiation from the central engine and re-emits thermal radiation at mid-IR (MIR) wavelengths (e.g Neugebauer et al. 1979; Rieke & Lebofsky 1981). AGN can thus show a red power-law at MIR wavelengths in their spectral energy distributions (SED) (e.g Alonso-Herrero et al. 2006; Donley et al. 2007, 2012; Mateos et al. 2012), which can be identified with imaging from the Infrared Array Camera (IRAC; Fazio et al. 2004) on *Spitzer* or with the *Wide-field Infrared Survey Explorer* (WISE; Wright et al. 2010). Dust heated by AGN is warmer than dust heated by star formation (e.g. Donley et al.

2012), which allows AGN to be distinguished from normal star-forming galaxies at these wavelengths.

Different selection techniques have been proposed to separate AGN from the galaxy population in MIR color-color space (e.g Lacy et al. 2004; Stern et al. 2005; Assef et al. 2010; Messias et al. 2012; Donley et al. 2012; Mateos et al. 2012). These methods can identify heavily obscured X-ray and optical AGN (e.g. Daddi et al. 2007b; Fiore et al. 2008) as well as luminous AGN, regardless of the obscuration and viewing angle (e.g. Hao et al. 2011). However, studies show that samples of AGN based on any of these IR selection techniques suffer from selection biases such that they mainly identify luminous AGN (e.g Mendez et al. 2013).

AGN also produce significant radiation at optical wavelengths. Broad optical emission lines (FWHM > 2000 km s^{-1}) in unobscured AGN and narrow optical emission lines in obscured AGN, which arise from gas located several hundred parsec away from the SMBH (therefore suffering only from moderate obscuration (e.g. Keel et al. 1994; Kauffmann et al. 2003a)), can provide detailed information about the central SMBH. At low redshifts, optical diagnostics such as the "BPT diagram" (e.g. Baldwin et al. 1981), which shows the optical emission line ratios of [N II]/Hα versus [O III]/Hβ , have been widely used to identify AGN. Various studies based on Sloan Digital Sky Survey (SDSS) data indicate that AGN and star-forming galaxies form distinct sequences on the BPT diagram with some overlap (e.g. Kauffmann et al. 2003a; Kewley et al. 2006; Kauffmann & Heckman 2009a, for a recent review see Heckman & Best 2014). One of the greatest advantages of this technique is that it can identify less powerful AGN with low accretion rates that might be obscured at other wavelengths.

Despite its advantages, there are various issues with the BPT diagnostics. The narrow optical emission lines can suffer from significant extinction due to the dust in the galaxy. Also at higher redshifts it is more difficult to detect the required lines for the BPT

diagram at high signal-to-noise ratio (as the optical emission lines shift to the near-IR wavelengths where the terrestrial background is higher). With AGN and star formation both being sources of optical emission lines, disentangling the contributions from each of these phenomena can be another challenge (e.g. Kauffmann & Heckman 2009a; Wild et al. 2010; Tanaka 2012). Furthermore, using the BPT diagram at higher redshifts may require re-calibration of the lines separating AGN from the star-forming sequence (e.g. Coil et al. 2015; Shapley et al. 2015).

The selection biases in each identification method indicate that using a single waveband cannot recover the full population of AGN (e.g Hickox et al. 2009; Juneau et al. 2011; Mendez et al. 2013; Trump et al. 2013; Goulding et al. 2014). Many studies have investigated properties of AGN host galaxies using multi-wavelength data at low and moderate redshifts (e.g Klesman & Sarajedini 2012; Mendez et al. 2013; Goulding et al. 2014; Sartori et al. 2015). To obtain a better understanding of the properties of AGN host galaxies requires detailed information at $z \sim 1-3$, the epoch of peak of AGN activity; however, current samples at these redshifts are relatively small.

Studying the host galaxies of AGN—revealing the types of galaxies that tend to host AGN—can provide important insights into the physical mechanisms that trigger AGN activity. Furthermore, we can assess whether AGN appear to have an impact on the galaxies that they live in, altering their properties compared to the overall galaxy population. Numerous studies have investigated the position of AGN in the color-magnitude diagram, as well as star formation activity, stellar mass, stellar age or colors of AGN host galaxies at different redshifts to investigate the impact of AGN activity on their host galaxies (e.g. Kauffmann & Heckman 2009a; Schawinski et al. 2011; Aird et al. 2012; Rosario et al. 2013; Georgakakis et al. 2014b; Hernán-Caballero et al. 2014b; Rosario et al. 2015). It is known that galaxies in the optical color-magnitude diagram show a strong bimodal behavior and can generally be divided into two populations: the

blue cloud of star-forming galaxies and the red sequence with mainly passive, quiescent galaxies (e.g. Blanton et al. 2003; Bell et al. 2003; Baldry et al. 2004). Early studies found that the majority of AGN lie on the red sequence (e.g Nandra et al. 2007; Hickox et al. 2009) and concluded that AGN feedback may be shutting down star formation in their host galaxies. More recent studies, however, highlight the importance of stellar-mass dependent selection effects (e.g Silverman et al. 2009; Xue et al. 2010; Cardamone et al. 2010; Aird et al. 2012; Hainline et al. 2012). In fact, most of these studies find that in a sample with matched stellar mass host galaxies, AGN are equally likely to be found in any host population.

Using far-IR (FIR) and sub-mm measurements from *Herschel* and *ALMA*, many recent studies find that AGN predominantly live in star-forming galaxies (e.g. Mullaney et al. 2012b; Santini et al. 2012; Harrison et al. 2012; Rosario et al. 2013; Mullaney et al. 2015). However, *Herschel* observations are biased towards FIR bright galaxies. Aird et al. (2012) and Azadi et al. (2015) use samples of moderate luminosity AGN and stellar mass complete galaxies from the PRIMUS redshift survey to show that AGN reside in both the quiescent and star-forming galaxy populations, although galaxies that are forming stars are 2-3 times more likely to host an AGN. While these studies find evidence of enhanced star formation activity in AGN hosts (compared to the inactive galaxies with a similar mass distribution), uncertainties in estimates of SFR (e.g. due to the depth of the observations, the effects of dust reddening, or corrections for AGN contamination), as well as the various selection biases inherent to AGN samples, limit our understanding of the connection between black hole growth and the growth of galaxies, especially at high redshifts.

A number of studies have investigated whether there is a correlation between the SFR and AGN activity in individual galaxies (see, e.g., Azadi et al. 2015, and references therein). Tracking star formation activity only in circumnuclear regions ($r < 1$kpc),

Diamond-Stanic & Rieke (2012) find evidence of a correlation between the luminosity of nearby Seyferts and their nuclear star formation and conclude that these process are related in the very central regions of galaxies (see also LaMassa et al. 2013). Tracking galaxy-wide star formation, studies of moderate luminosity AGN typically find no significant correlation between SFR and AGN activity (e.g. Rosario et al. 2012; Mullaney et al. 2012b; Stanley et al. 2015; Azadi et al. 2015), while studies of the most luminous AGN find a positive trend that could be driven by major mergers (e.g. Rosario et al. 2012; Dai et al. 2015; Bernhard et al. 2016). However, rapid variability in the AGN luminosity can result in scatter, consequently washing out the intrinsic correlation between AGN luminosity and SFR. Therefore considering the average AGN luminosity for samples of galaxies of a fixed SFR, instead of the luminosities of individual AGN, may be more appropriate for exploring the relationships between AGN activity and star formation (e.g. Hickox et al. 2014). In fact, studies investigating average AGN luminosity in bins of SFR find a positive correlation between AGN luminosity and SFR (e.g. Chen et al. 2013; Azadi et al. 2015; Dai et al. 2015).

Due to the reliability of X-ray AGN identification, the majority of the studies discussed above use only X-ray imaging to identify AGN and subsequently assess the properties of their host galaxies using multi-wavelength data. As noted above, MIR imaging and optical rest-frame spectroscopy can also identify AGN that may be obscured at other wavelengths. Optical spectra in particular can also provide detailed information about the gas, dust and stellar populations of the AGN host galaxies. Until recently such detailed information has been only available at low redshifts, but with the advent of multi-object near-infrared (NIR) spectrographs such as KMOS (Sharples et al. 2013) and MOSFIRE (McLean et al. 2012), this information can be obtained at high redshift as well (e.g. Trump et al. 2013; Genzel et al. 2014; Coil et al. 2015; Harrison et al. 2016).

In this paper we use rest-frame optical spectra from the MOSFIRE Deep Evolution Field (MOSDEF) survey (Kriek et al. 2015) taken with the MOSFIRE multi-object NIR spectrograph on the Keck I telescope to investigate AGN identification at multiple wavelengths and their host galaxy properties at $z \sim$1.37 – 3.80. Considering data from the first season of the MOSDEF survey, Coil et al. (2015) found that while the BPT diagram works well for identifying optical AGN at $z \sim 2$, it cannot provide a complete sample of AGN, as it suffers from biases against low mass and/or high specific star formation rate (sSFR) host galaxies. In this paper, with a larger dataset from the first two years of the MOSDEF survey, we identify optical AGN using the BPT diagram and use additional AGN samples selected *a priori* based on X-ray and IR imaging data to investigate the selection biases from each identification method. We explore the host galaxy properties of these AGN and investigate the relation between star formation and AGN luminosity in our sample at the epoch of the peak of both AGN and galaxy growth.

The outline of the paper is as follows: in Section 3.3 we describe the X-ray and IR data used to identify AGN in MOSDEF, along with the method used for measuring the optical emission line ratios that is used for identifying optical AGN. In this section we also provide information about stellar mass and SFR estimates in our sample. In Section 3.4 we present our results on the AGN host galaxy properties and the relation between AGN activity and SFR at $z \sim 2$. In Section 3.5 we discuss our results, and we conclude in Section 3.6. Throughout the paper we adopt a flat cosmology with Ω_Λ =0.7 and H_0=72 km s^{-1}Mpc^{-1}.

3.3 Sample and Measurements

In this study, we use multi-wavelength data from the MOSDEF survey to investigate AGN host galaxy properties at $z \sim 2$. We use X-ray imaging data from *Chandra*, IR imaging data from *Spitzer-IRAC*, and rest-frame optical spectra obtained with the MOS-

FIRE spectrograph at Keck Observatory to identify AGN. We describe these datasets below, as well as our methods for fitting the optical emission lines in our spectra and for estimating stellar masses and SFRs of AGN host galaxies by fitting their SEDs.

3.3.1 The MOSDEF Survey

In this study, we use spectroscopic data from the MOSDEF survey (Kriek et al. 2015). This survey uses the MOSFIRE spectrograph (McLean et al. 2012) on the 10 m Keck I telescope. MOSFIRE provides wavelength coverage from 0.97 to 2.40 μm with a spectral resolution of R = 3400, 3300, 3650, and 3600 respectively in the Y, J, H, and K bands. MOSDEF observations cover a total area of 500 arcmin^2 in three extragalactic fields: COSMOS, GOODS-N, and EGS from the CANDELS survey (Grogin et al. 2011; Koekemoer et al. 2011) in areas with 3D-*Hubble Space Telescope* (*HST*) grism survey (Brammer et al. 2012) coverage. Along with *HST* imaging, there is extensive multi-wavelength ancillary data from other telescopes including *Chandra, Spitzer* and *Herschel* for MOSDEF targets. In this paper we use data from the first two years of the survey. During this time observations were also taken in the GOODS-S and UDS fields, in addition to the main survey fields above, and these data are included here.

MOSDEF targets span a wide range of redshift from $1.37 < z < 3.80$ and when completed, the survey will include $\sim$1500 galaxies and AGN. The targets are chosen from three distinct redshift intervals ($1.37 < z < 1.70$, $2.09 < z < 2.61$ and $2.95 < z < 3.80$) to ensure that the rest-frame optical emission lines fall within windows of atmospheric transmission. Sources in MOSDEF are targeted down to limiting *HST* /WFC3 F160W magnitudes of 24.0, 24.5, and 25.0, respectively, at $z \sim 1.5$, 2.3, and 3.4 using the 3D-*HST* photometric catalogs (Skelton et al. 2014). Target priorities in MOSDEF are determined by their brightness and redshift information, with brighter sources and those with more secure prior redshift determinations given higher weights. AGN identified in advance

via X-ray or IR imaging are also given higher targeting weights. In data from the first two years of the MOSDEF survey, which we use here, we identify 482 galaxies and 55 AGN. Detailed information about the MOSDEF AGN sample is provided below. The full details of the survey, data reduction and analysis are presented in Kriek et al. (2015).

3.3.2 X-ray AGN Selection

The X-ray AGN in our sample were identified prior to MOSDEF targeting using the *Chandra* imaging in our fields, which had a depth of 4 Ms in GOODS-S, 2 Ms in GOODS-N, 800 ks in EGS and 160 ks in COSMOS (at the time of MOSDEF target selection). We use catalogs generated in a consistent manner as described by Laird et al. (2009) and Nandra et al. (2015) (see also Georgakakis et al. 2014c; Aird et al. 2015). Our adopted Poisson false probability detection threshold ($< 4 \times 10^{-6}$) corresponds to reaching hard band flux ($f_{2-10\ \mathrm{keV}}$) limits (over $>$10% of the area) of 1.6×10^{-16}, 2.8×10^{-16}, 5.0×10^{-16} and 1.8×10^{-15} in the GOODS-S, GOODS-N, EGS and COSMOS fields, respectively (although we note that the depths of the *Chandra* imaging varies substantially within a field).

We use the likelihood ratio technique to identify reliable optical, NIR and IRAC counterparts to the X-ray sources (as described in Aird et al. 2015; see also Sutherland & Saunders 1992b; Ciliegi et al. 2003b; Brusa et al. 2007b; Laird et al. 2009). For sources with multiple counterparts, we choose the match with the highest likelihood ratio. Finally, we match our catalog of X-ray counterparts to the 3D-*HST* catalogs used for MOSDEF targeting and find the closest 3D-*HST* match within $1''$.

For our X-ray AGN, we estimate the rest-frame 2–10 keV X-ray luminosities based on the hard (2–7 keV) observed flux or, if the source is not detected in the hard band, the soft (0.5-2 keV) observed flux. We assume a simple power-law spectrum including only Galactic absorption with a photon index of $\Gamma = 1.9$. We do not correct

our X-ray luminosities for intrinsic absorption effects (local to the AGN). At $z \sim 2.3$, only about 10% of the observed X-ray flux is suppressed at a column density of 10^{23} cm^{-2}. Therefore, our estimates of the X-ray luminosity are accurate and larger absorption column densities ($N_H > 10^{23}$ cm^{-2}) are required to significantly suppress the observed flux at $z \sim 2$.

In total, there are 28 X-ray AGN in the current MOSDEF sample, 22 of which are detected in the hard band with X-ray luminosities ($L_{\mathrm{X(2-10\ keV)}}$) within the range of 10^{43} to 10^{45} erg s^{-1}. Given the relatively high X-ray luminosities of these sources, we do not impose any luminosity cut on the X-ray AGN sample.

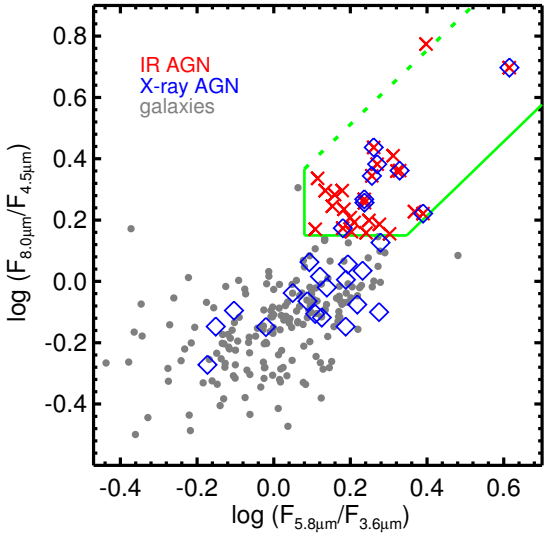

Figure 3.1. IRAC color-color space for MOSDEF sources, where criteria from Donley et al. (2012) defined in equations 3.2 to 3.4 in the text are shown in green. The gray points show MOSDEF galaxies, and the blue diamonds are X-ray AGN identified in section 3.3.2. The red points show the sources that fall inside the Donley-defined wedge and therefore are selected as IR AGN.

3.3.3 IR AGN Selection

Using hard X-ray (2–10 keV) detections ensures that our sample is not strongly biased against moderately obscured ($N_H \sim 10^{22-24}$ cm^{-2}) AGN, however, hard X-ray

radiation cannot penetrate Compton-thick regions with heavy obscuration ($N_H > 10^{24}$ cm^{-2}). In heavily obscured AGN, the high energy nuclear emission is absorbed and reprocessed by dust near the AGN and re-radiated at MIR wavelengths. This re-radiated emission from dust results in MIR imaging also being useful in identifying AGN.

Several MIR AGN selection techniques have been proposed using data from the IRAC (Fazio et al. 2004) on the *Spitzer* space telescope (e.g. Lacy et al. 2004; Stern et al. 2005; Alonso-Herrero et al. 2006; Donley et al. 2008, 2012). Depending on the depth of the data and the redshift of interest, some of these criteria can suffer from contamination from star-forming galaxies mis-identified as AGN. In starburst galaxies or galaxies with older stellar populations and/or higher dust extinction the stellar bump can mimic the power-law emission from AGN.

The Stern et al. (2005) criteria, which were empirically derived from shallow, wide-area *Spitzer* data, have been shown to be unreliable at various redshifts ($z \sim 1$ and $z \gtrsim 2.5$) (e.g. Georgantopoulos et al. 2008; Donley et al. 2012; Mendez et al. 2013). Here, using IRAC fluxes from v4.1 of the 3D-*HST* catalogs (Skelton et al. 2014), after removing X-ray AGN, we find that $\sim$10% of the full MOSDEF sample falls within the Stern et al. (2005) selection region (only $\sim$38% of these sources are IR AGN using the Donley et al. 2012 criteria), indicating that the Stern et al. (2005) selection may be contaminated by star-forming galaxies at the redshift and depth of our survey.

Donley et al. (2012) provide more reliable IR AGN identification criteria, which are designed to limit the contamination from star-forming galaxies, especially at high redshift. The robustness of this selection technique in identifying IR AGN from star-forming galaxies is confirmed by Mendez et al. (2013), using a large faint galaxy sample at intermediate redshifts. In the Donley et al. (2012) selection criteria, objects are required to be detected in all four IRAC bands and satisfy the following criteria in IRAC color-color space:

$$x = \log_{10}\left(\frac{f_{5.8\mu\mathrm{m}}}{f_{3.6\mu\mathrm{m}}}\right), \quad y = \log_{10}\left(\frac{f_{8.0\mu\mathrm{m}}}{f_{4.5\mu\mathrm{m}}}\right) \tag{3.1}$$

$$x \geq 0.08 \text{ and } y \geq 0.15 \text{ and} \tag{3.2}$$

$$y \geq (1.21 \times x) - 0.27 \text{ and} \tag{3.3}$$

$$y \leq (1.21 \times x) + 0.27 \text{ and} \tag{3.4}$$

$$f_{4.5\mu\mathrm{m}} > f_{3.6\mu\mathrm{m}} \text{ and} \tag{3.5}$$

$$f_{5.8\mu\mathrm{m}} > f_{4.5\mu\mathrm{m}} \text{ and} \tag{3.6}$$

$$f_{8.0\mu\mathrm{m}} > f_{5.8\mu\mathrm{m}} \tag{3.7}$$

In MOSDEF we identify IR AGN using these criteria, with some slight modifications. In addition to the detection in all four IRAC bands, we set a flux limit in each band that corresponds to a S/N respectively in channels 1 to 4 of 3, 3, 2.4, and 2.1 (see Mendez et al. 2013 for an explanation of how these limits are derived).

Figure 3.1 shows the relevant IRAC color-color space of $\log(f_{8.0\mu m}/f_{4.5\mu m})$ versus $\log(f_{5.8\mu m}/f_{3.6\mu m})$. The green solid and dashed lines indicate the criteria defined in equations 3.2 to 3.4, and enclose an area referred to as the "Donley wedge." The gray points are galaxies in the MOSDEF sample and the blue diamonds are X-ray AGN identified in section 3.3.2. The red points show the sources that fall inside the Donley wedge and therefore are selected as IR AGN. There is one red source above the dashed line that satisfies all the above criteria except for equation 3.4. The IRAC photometry for this source indicates a sharp increase in the flux from channel 1 to 4, which is common only in IR AGN. Since none of the galaxies in MOSDEF lie close to the dashed line,

we relax the upper bound on Donley wedge, showing it with a dashed line in Figure 3.1 and including this red source in our IR AGN sample. There are also three sources inside the Donley wedge that satisfy all the above criteria except for one of the equations 3.5, 3.6 or 3.7, which require a strictly increasing, red power-law SED in the IRAC bands. We relax these three criteria such that any source consistent with an increasing red power-law *within the 1σ errors on the IRAC photometry* is classified as an IR AGN. We note that 32% of the X-ray AGN lie inside the Donley wedge, which indicates that they are identified as AGN based on both the X-ray and IRAC imaging data. In total we identify 27 IR AGN in the current MOSDEF sample, 9 of which are also detected in X-rays.

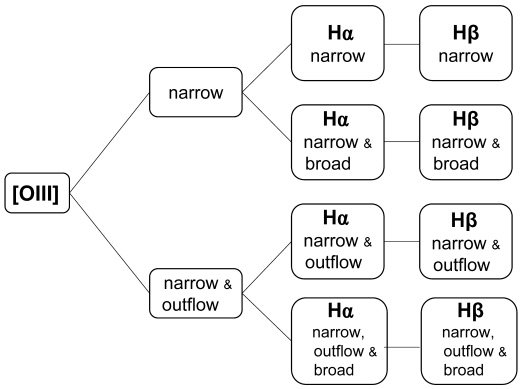

Figure 3.2. A flowchart representing the logic of our Gaussian emission line fitting procedure: In each step we evaluate any change in χ^2 to establish whether the additional components results in an improved fit (at the 99% confidence level). We first evaluate the fit to [O III] to determine whether an additional outflow component is required. We then evaluate whether the Hα fit requires a broad component (also including an outflow component if required by [O III]). Lastly, we fit Hβ with the same components as Hα .

3.3.4 Spectroscopic Data and Optical AGN Selection

The MOSDEF survey has obtained spectroscopic data using the MOSFIRE spectrograph, which enables us to detect emission lines at rest wavelengths of 3700–7000Å for our sources. These data enable us to use optical diagnostics such as the BPT

diagram (Baldwin et al. 1981; Veilleux & Osterbrock 1987) to identify AGN that may not be detectable with X-ray or IR imaging data. In this section we describe the emission line fitting procedure we used for measuring the flux of each line, and the AGN that are identified with optical diagnostics.

Optical Emission Line Flux Measurements

In order to use optical diagnostics to identify AGN in our sample, we need to measure the Hβ , [O III] , Hα , and [N II] emission lines. We fit Gaussian functions to the observed lines using the `MPFIT` nonlinear least-square fitting function in IDL (Markwardt 2009), using the error spectra to determine the errors on the fit. We simultaneously fit [O III] λ5008 with [O III] λ4960 , and Hα with [N II] λ6550 and [N II] λ6585 . We fix the continuum to be flat, with no slope, and allow up to 0.15% freedom to the centroid of the expected narrow and broad lines wavelength. We require the same physical component (i.e., narrow line, broad line) to have the same FWHM and velocity offset in each line, as determined from the line with the highest S/N. We fix the spacing between the [O III] λ4960 and [O III] λ5008 forbidden lines and fix their relative normalizations to a ratio of 1:3 (as well as for the [N II] λ6550 and [N II] λ6585 lines). For each source we consider four different models for the emission line profiles, with various components, as described below.

In model 1, we fit each line with a single Gaussian function with the same centroid velocity and FWHM which is required to be $<$2000 km s^{-1}, representing the narrow emission line component. In model 2, we fit each line with a narrow Gaussian component and additionally for Hβ and Hα include a broad Gaussian component (FWHM $>$2000 km s^{-1}) representing emission from the AGN broad-line region. In model 3, we fit each line with two Gaussian components, one narrow line component as above and a second component with a FWHM $<$2000 km s^{-1} and a negative velocity offset ($-500 < v < 0$

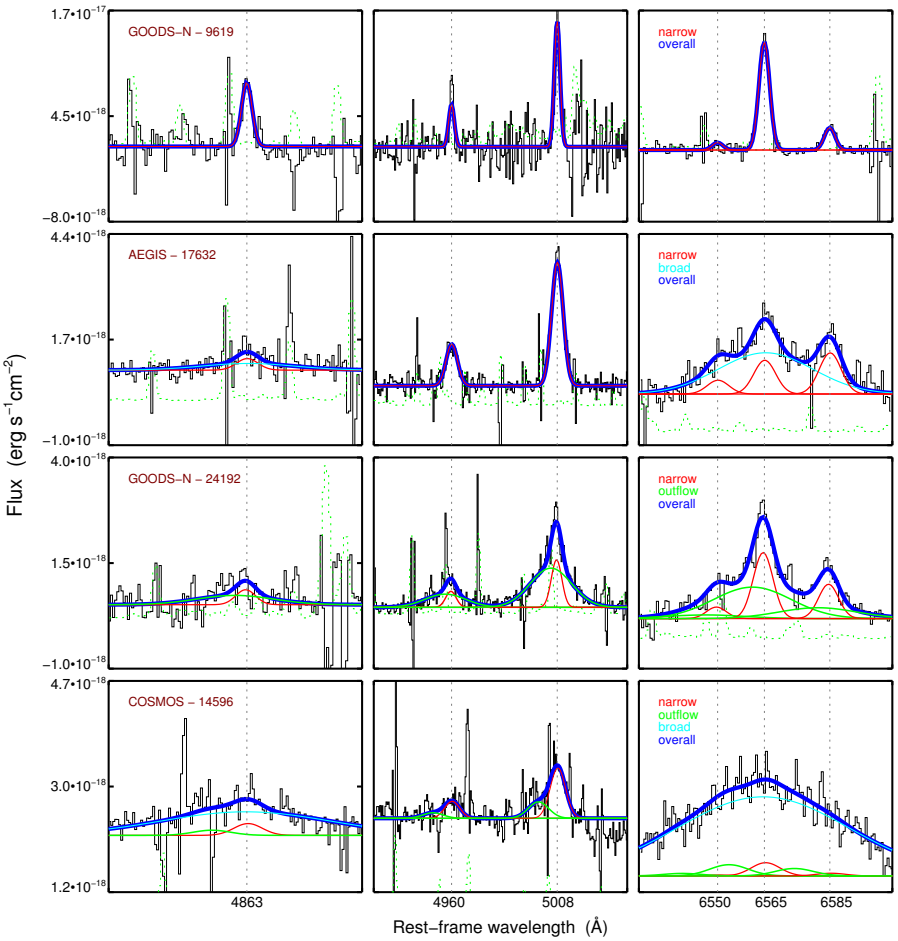

Figure 3.3. Examples of MOSDEF spectra and the multiple-component fitting procedure for four AGN in our sample (the IDs are from v4.1 of the 3D-*HST* catalogs). The overall fit is shown in blue, while the individual Gaussian components are shown in different colors: red for the narrow component, green for an outflow, and cyan for a broad component. The error spectra are shown with dotted green lines, while vertical dotted gray lines show the rest frame wavelength of the emission lines we fit. The top row shows an AGN where only a narrow Gaussian component is required to all of the lines. The second row shows an AGN that requires an additional broad component to Hβ and Hα . The third row shows an AGN with a clear outflow component, detected in the [O III] and Hα lines. The fourth row shows an AGN that requires both an outflow component (seen in [O III] λ5008) and a broad component. Sources that have a broad Hα and/or Hβ component with the S/N $>$ 3 are excluded from our analysis in Section 3.4, as we can not reliably probe their host galaxy properties.

km s^{-1}) relative to the narrow line component, representing an outflow that could be driven by an AGN (Leung et al. 2016 in preparation). The FWHM and centroid velocity

of the outflow component is fixed to be identical for all of the emission lines. In model 4, we fit each line with narrow and outflow components, and additionally allow for a broad component with an identical FWHM (>2000 km s^{-1}) to the Hβ and Hα lines.

In each model we evaluate any change in reduced χ^2 to establish whether the additional components result in an improved fit at confidence level of 99%. Figure 3.2 is a flowchart that shows the order of our fitting procedure. We first evaluate the reduced χ^2 from model 1 to model 3 for the [O III] line to see if the additional outflow component has improved the fit. If so, we then evaluate the Hα fit from model 3 to 4 to see if an additional broad component improves the fit. If the [O III] line is well fit with only a narrow component, we then compare the Hα fit in model 1 with model 2 to see whether the additional broad component improves the fit.

To find the minimum width of the Gaussian components, we identify sky lines in each wavelength filter for each source, fit them with a single Gaussian component, and use their average width as the minimum width of the narrow line fits. This sets the minimum width for the velocity dispersion of 2.5 Å in the observed H band and 3.5 Å in the observed K band, which at $z \sim 2.3$ corresponds to $\sim$ 45 km s^{-1} and $\sim$ 48 km s^{-1} respectively in H and K bands. The minimum width for the broad Gaussian component is set by the upper limit on the FWHM ($<$ 2000 km s^{-1}) of the narrow lines.

Figure 3.3 illustrates examples of MOSDEF spectra for four different AGN in our sample, with the best fit result of our multiple-component fitting procedure. The overall fit is shown in blue, and the individual components are shown in different colors. The top panel shows an AGN where a narrow Gaussian component is the best fit to all the lines. The second panel shows an AGN with a narrow component for all lines and an additional broad component to Hβ and Hα . The third panel shows an AGN with a significant outflow component for both the [O III] and Hα lines, in addition to the narrow component. In the last panel in addition to the outflow component (seen in the

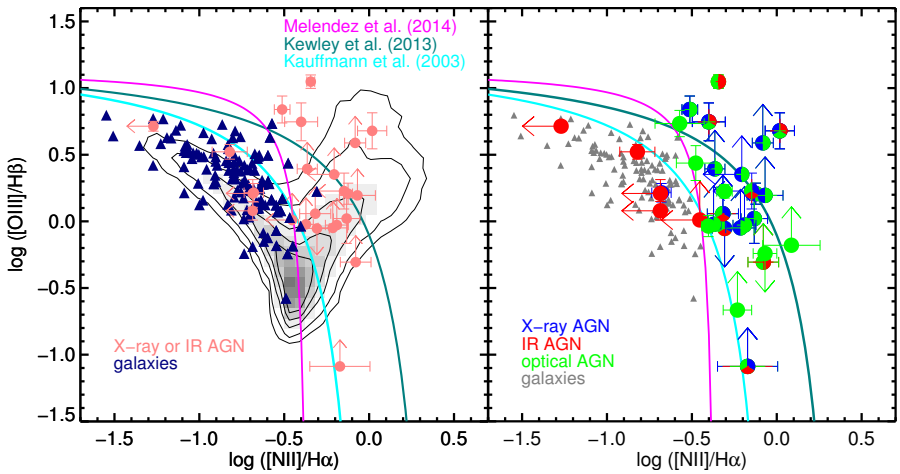

Figure 3.4. The BPT diagram for MOSDEF AGN and galaxies. *Left:* Pink circles show AGN identified with X-ray and/or IR imaging, with arrows showing 3σ limits for AGN for which all four relevant optical emission lines are not detected in MOSDEF. Dark blue triangles show MOSDEF galaxies (with $> 3\sigma$ detections of all four relevant optical emission lines). The contours and grayscale show the location of SDSS sources in this plane. The cyan line is the empirical criteria from Kauffmann et al. (2003a) that indicates the division between star-forming galaxies and AGN in SDSS. The dark green line is the theoretical prediction from Kewley (2013) of the maximum line ratios expected for starburst galaxies, in the absence of an AGN. The magenta line is the theoretical prediction for identifying AGN by Meléndez et al. (2014). Here we use this line to identify optical AGN in MOSDEF, as this line most cleanly separates known X-ray and/or IR AGN from galaxies in our sample. *Right:* Similar to the left panel but here MOSDEF AGN are shown using different colors that indicate the wavelength used to identify them as AGN. X-ray AGN are shown in blue, IR AGN are shown in red, and optical AGN (identified as lying above the Meléndez et al. (2014) line) are shown in green. The AGN that are identified using more than one wavelength method are shown with multiple colors. The MOSDEF galaxies with $> 3\sigma$ detections of all four of the necessary emission lines are shown in gray.

[O III] λ5008 line), the Hα fit improves with an underlying broad component.

In our spectral fits, we find that four AGN (identified at both X-ray and IR wavelengths) require a broad Hα and/or Hβ component with the S/N > 3. Since we can not reliably probe the host galaxy properties of these AGN, we exclude them for the analysis in Section 3.4. We keep these sources in our sample for the purpose of identifying optical AGN below in Section 3.3.4, but we do not consider the contributions

from the broad optical emission lines.

We note that for all sources where the best fit included an outflow component, we visually inspected the *HST* imaging to determine whether they might be merger candidates; in these cases the "outflow" component might not be from an outflow, but from a merger event. We identified six sources (ID = 28202, 26028, 22299, 16339, 9183, 3146 in v4.1 of 3D-*HST*) with two potential nuclei that indicate that the host galaxies of these AGN may be undergoing merger events. Since it is not clear which of the two components has the detected AGN, and since the photometry of the two components will often be blended for these sources, we exclude them from the analysis of AGN spectral or host galaxy properties in this paper. Of the 28 X-ray AGN in our sample, four are merger candidates, while from the 27 IR AGN, two are merger candidates.

Optical AGN Sample

We use the fluxes from our line fitting procedure to measure the [N II]/Hα and [O III]/Hβ line ratios, required to place sources on the BPT diagram. We do not include broad components in these fluxes. We correct the flux of the narrow components of the Hβ and Hα lines for underlying stellar absorption, using the best-fit SED models to the multi-wavelength photometry (for more details see Reddy et al. 2015). This correction results in an average change of ~ 0.01 and ~ 0.06 dex respectively in log([N II]/Hα) and log([O III]/Hβ) line ratios on the BPT diagram and thus has a small effect on our sample.

Figure 3.4 shows the BPT diagram for MOSDEF AGN and galaxies. In the left panel, AGN identified at either X-ray or IR wavelengths are shown with pink circles; the remaining MOSDEF sources (with $> 3\sigma$ detections of all four of the necessary emission lines) are shown with blue triangles. We note that there are galaxies with $< 3\sigma$ detections that are not shown in this panel. For the X-ray and IR selected AGN, since they are already identified as AGN with reliable methods we require a significant ($> 3\sigma$) detection

of at least one of the two lines required for each ratio. If the other line is not significantly detected, we use the 3σ limit on the flux to determine the limit on the line ratio (indicated by the arrows in Figure 3.4). For the 40 X-ray and/or IR detected AGN in our sample, we are able to place 24 AGN on the BPT diagram (including those with limits).

For comparison, we show the location of SDSS sources with contours and grayscale in this panel. The cyan line is the empirical demarcation from Kauffmann et al. (2003a) that shows the division between star-forming galaxies and AGN in SDSS. The dark cyan line is the theoretical prediction from Kewley (2013) of the maximum line ratios expected in starburst galaxies, in the absence of an AGN. We also show in magenta the theoretical prediction for the lowest line ratios allowed by AGN of Meléndez et al. (2014).

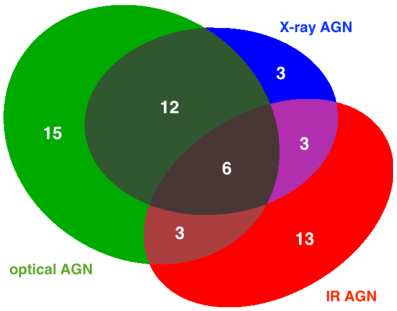

Figure 3.5. A Venn diagram showing the number of AGN in our sample identified at different wavelengths; the full sample contains 55 AGN (and 482 galaxies). The overlapping regions show the number of AGN selected at multiple wavelengths. This diagram shows our detected AGN sample and is not corrected for observational biases such as the depth of the data at each wavelength.

Sources that lie between the Kauffmann et al. and Kewley et al. lines are often referred as "composite" sources, in that their line ratios can have contributions from both star formation and AGN activity. For sources to the right of the Kewley (2013) line, such high line ratios can only be due to AGN activity (e.g. Shapley et al. 2015). We note that

the galaxies in our sample lie above the main locus of star-forming galaxies in SDSS in log([O III]/Hβ) and/or log([N II]/Hα) (by a median offset of $\sim$ 0.1 dex, see Coil et al. 2015; Shapley et al. 2015). This offset has been seen in other studies of high redshift galaxies (e.g. Yabe et al. 2012; Masters et al. 2014; Newman 2014; Steidel et al. 2014). Applying a luminosity limit to the SDSS sample that is comparable to the limit for high redshift galaxies reduces this offset somewhat (Juneau et al. 2014) but as shown in Coil et al. (2015) the offset does not completely disappear.

Figure 3.4 shows that the Kauffmann et al. (2003a) line may not be as reliable as a means of separating galaxy and AGN populations at $z \sim 2$ as at $z \sim 0$. On the other hand, using the Kewley (2013) line, which demarcates a pure sample of AGN, results in a highly incomplete and restricted AGN sample. In fact, the majority of the X-ray or IR detected AGN in the MOSDEF sample lie below the Kewley (2013) line. As discussed in Coil et al. (2015), the Meléndez et al. (2014) line can be used to more reliably separate galaxies and AGN in MOSDEF. The left panel of Figure 3.4 shows that the vast majority of the X-ray and IR detected AGN in our sample lie above this line, while the majority of the other MOSDEF sources lie below this line. Therefore in this study we identify all sources with line ratios that are above this line as optical AGN.

The right panel of Figure 3.4 shows the BPT diagram for MOSDEF sources, using the above classification of AGN at different wavelengths. For AGN that are identified using multiple wavelengths, we use multiple colors based on their identification methods. MOSDEF galaxies with at least 3σ detections in all four lines are shown with gray triangles. We emphasize that in addition to the four sources above the Meléndez et al. (2014) line in the left panel of Figure 3.4 which we identify as optical-only AGN, there are 11 sources with 3σ detections in both Hα and [N II] λ6585 without reliable Hβ and [O III] λ5008 detections. We also classify these sources as optical AGN due to their high log([N II]/Hα), which is greater than -0.3.

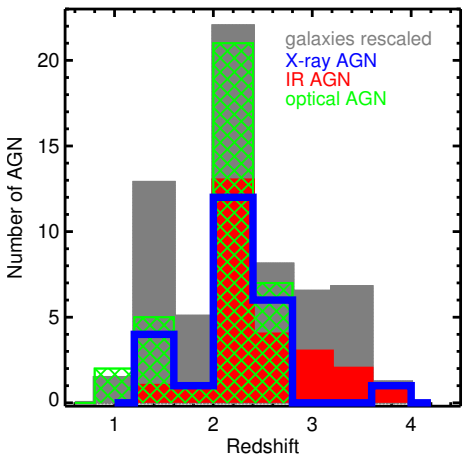

Figure 3.6. The redshift distribution for the 55 AGN and 482 galaxies in the MOSDEF sample. The distribution for each identification technique is shown with a different color. AGN identified at multiple wavelengths are counted in each distribution and can therefore be represented multiple times in this figure.

Using a UV-selected galaxy sample, Steidel et al. (2014) find a larger offset for star-forming galaxies in the BPT diagram, compared with local samples. Using the Meléndez et al. (2014) line to identify optical AGN in their sample would lead to a larger AGN fraction than in the MOSDEF sample and may lead to more contamination by star-forming galaxies in their sample. Instead, a more strict criterion of log([N II]/Hα) > -0.3 could be used. In the MOSDEF sample, however, using this cut results in only four sources being removed from the optical AGN sample and therefore does not change any of our conclusions. Since the Meléndez et al. (2014) line provides the cleanest separation between known AGN and galaxies in the MOSDEF sample, we use it here. We also note that it is unlikely that the integrated light of many of our sources to be dominated by shocks, which could potentially also move sources above the Meléndez et al. (2014) line.

For the sample used here, there are 40 X-ray and/or IR AGN, of which 21 are also identified as optical AGN. In addition, there are 15 sources classified as optical AGN that are only identified as AGN through optical diagnostics. In total, there are 55 AGN

in the MOSDEF sample. Figure 3.5 is a Venn diagram illustrating the number of AGN identified at different wavelengths in our sample. We use ellipses instead of circles in the Venn diagram, so that the areas are proportional to the number of AGN identified with each method.

Figure 3.6 illustrates the redshift distribution for AGN and galaxies in our sample. Each color represents the redshift distribution for a different identification technique, and as a single AGN can be detected at multiple wavelengths it can contribute to more than one histogram in this figure. While our AGN span a wide range of redshifts, they strongly peak at $z \sim 2$, due to the MOSDEF target selection. We note that we cannot identify optical AGN at $z > 2.6$, as at these redshifts the Hα and [N II] λ6585 lines fall beyond the observed wavelength coverage of our MOSFIRE spectra.

3.3.5 Stellar Mass and SFR Estimates

To measure the SFR and stellar mass of the AGN host galaxies, we use SED fitting, which is a widely adopted method for estimating physical properties of galaxies. We use the FAST stellar population fitting code (Kriek et al. 2009) with the multi-wavelength photometry from 3D-*HST* (Skelton et al. 2014) and the MOSDEF spectroscopic redshifts. We adopt the Conroy et al. (2009) Flexible Stellar Population Synthesis (FSPS) models, along with a Chabrier (2003) stellar initial mass function (IMF), the Calzetti et al. (2000) dust reddening curve and use a fixed solar metallicity. We consider delayed exponentially declining star formation histories, $\Psi \propto t \exp\left(\frac{-t}{\tau}\right)$, where t is the time since the onset of star formation and τ is the characteristic star formation timescale and is within the range of $0.1 < \tau < 10$ Gyr. FAST searches over a grid of models and uses χ^2 fitting to determine the best fit solution (Kriek et al. 2009).

There is one AGN (identified at both X-ray and optical wavelengths) in our sample that is not fully spatially covered by the CANDELS imaging in the COSMOS field, such

that the photometry is underestimated at the CANDELS wavelengths; therefore we do not include this AGN when presenting results from SED fits in this paper.

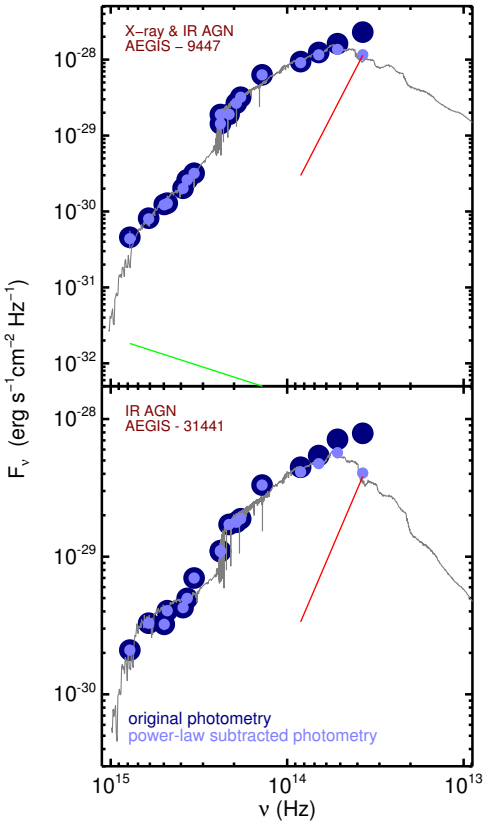

Figure 3.7. The observed photometry (dark blue) and power-law subtracted photometry (light blue) for two AGN in the MOSDEF sample. The green line shows the power-law subtracted from the original photometry at rest-frame wavelengths $< 1\ \mu m$, and the red line shows the power-law subtracted from the original photometry at rest-frame wavelengths $> 1\ \mu m$. The top panel shows an X-ray and IR AGN, where subtracting a blue power-law at UV and optical wavelengths and a red power-law at MIR wavelength results is a reduced χ^2 smaller than the fit to the original photometry. The bottom panel shows an IR AGN where the best fit requires subtracting only a red power-law, as shown.

Light from the AGN may contribute to the observed SED, particularly at UV and IR wavelengths, which can impact our estimates of the SFR and stellar mass of the host galaxy. The Wien tail of the blackbody radiation from dust grains near the SMBH can be fit with a red power-law at mid-IR wavelengths. Therefore, to take into account any possible contribution from the AGN, we subtract power-laws with varying slopes and

normalizations in both the UV and mid-IR from the observed photometry and re-run FAST on the remaining flux. We then choose the fit with the lowest reduced χ^2 as the best fit across all of the possible inputs (including no power-law subtraction, i.e., all galaxy light).

To create the grid of power-law SEDs to subtract, for both UV and mid-IR wavelengths, we allow the normalization to vary from 0 to 100 % in terms of the observed flux in the U and IRAC channel 3 (5.8 μm) bands. We assume power-laws of the form $F_\nu \propto \nu^\alpha$, where we allow α to range from 0 to 0.5 for the UV and -5 to -0.5 in the mid-IR. We note that Ivezić et al. (2002) considered a wider range of the optical spectral indices, $-2 \leq \alpha \leq 0.5$, based on the quasars in SDSS sample, but we consider a more limited range as the AGN in our sample are all lower luminosity and are type 2 AGN that are not expected to be dominated by the AGN component in the optical. We subtract the blue power-law from the photometry at rest-frame wavelengths < 1 μm.

For subtracting the red power-law corresponding to AGN contribution at mid-IR wavelengths, we initially considered slopes within the range of -3 to -0.5, following Donley et al. (2012). However, we found that a redder slope was often needed to describe the observed slope of the SED for the two reddest IRAC channels (3 and 4) and thus adjusted our limits to allow for slopes as red as $\alpha_{\rm IR} > -5$. We subtract the IR power-laws from the photometry at rest-frame wavelengths > 1 μm to avoid any unnecessary subtraction from other bands. The power-law subtraction allows us to correct for any possible contamination from AGN in our SED-derived host galaxy properties.

Figure 3.7 shows two examples of the original 3D-*HST* photometry and the power-law subtracted photometry for an AGN identified at both X-ray and IR wavelengths (top panel) and an IR-only AGN (bottom panel). The green line shows the power-law subtracted from the original photometry at rest-frame wavelengths < 1 μm, while the red line shows the power-law subtracted from the original photometry at rest-frame

wavelengths $> 1\ \mu m$. In the top panel, subtracting the blue power-law at UV and optical wavelengths and the red power-law at MIR wavelengths results in a better fit. For the IR AGN in the bottom panel subtracting only a red power-law at MIR wavelengths results in a better fit.

Using this method leads to a more robust estimate of SFR and stellar mass for AGN host galaxies. Santini et al. (2012) find that for type 2 AGN, stellar mass estimates derived from pure stellar templates are within a factor of two of the estimates derived including both stellar and AGN templates (with a mean difference of zero). Subtracting the AGN contribution from the original photometry as we do here leads to a 0.13 dex decrease in the average SFR and an 0.03 dex (in logarithmic space) decrease in the average stellar mass of the AGN in our sample.

Here we run the FAST code without using the so-called template error function, which can be used to account for any wavelength-dependent mismatch between the observed photometry of sources and the templates used (Brammer et al. 2008; Kriek et al. 2009, 2015). We find that the SFRs and stellar masses estimated from FAST without the template error function after subtracting power-laws are consistent with those derived from the original photometry using the template error function; this indicates our method for estimating SFR and stellar mass is robust.

3.3.6 [O III] Luminosity as a Proxy of AGN Activity

The [O III] emission line traces photoionized gas clouds in the narrow line region of AGN and is a good proxy for measuring nuclear activity (e.g. Kauffmann et al. 2003a; Heckman et al. 2005). However, star formation (SF) activity can also produce a narrow [O III] emission line, which can contaminate the signal from the AGN. At low redshifts, studies have used different methods to attempt to disentangle AGN and SF contributions to the [O III] emission line (e.g. Kauffmann & Heckman 2009a; Wild et al. 2010; Tanaka

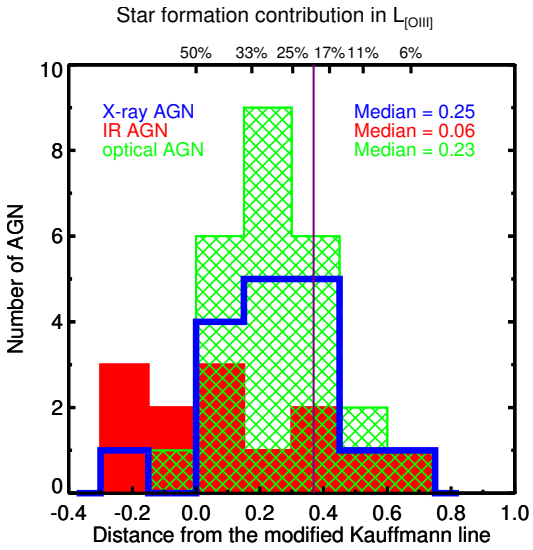

Figure 3.8. Histograms of the distance (in both [N II]/Hα and [O III]/Hβ) of each AGN population in the BPT diagram from the modified version of Kauffmann et al. (2003a) line (see text for details). The top x axis indicates the fractional star formation contribution to $L_{[OIII]}$, according to Kauffmann & Heckman (2009a). The median distance of our AGN sample is 0.17 dex which corresponds to a fractional contamination of $\sim$33%. The purple line roughly shows the distance of the Kewley (2013) line, above which the contamination is less than 20%.

2012). In this section we investigate whether these methods are applicable to higher redshift samples and estimate the contribution from SF to [O III] luminosity in our sample.

Kauffmann & Heckman (2009a) and Wild et al. (2010) use empirical techniques to estimate the contribution of SF to $L_{[OIII]}$ by measuring the distance of each source in the BPT diagram from the main locus of star formation. Kauffmann & Heckman (2009a) find that the contribution to $L_{[OIII]}$ from SF varies from $\sim$50% for sources on the Kauffmann et al. line to $\sim$10% for sources above the Kewley et al line.

Alternatively, Tanaka (2012) use SED fitting to estimate the SFR for SDSS sources, and then convert this to an Hα luminosity using the Kennicutt (1998) relation, with an additional power-law as an extinction factor estimated at the Hα wavelength. They then fit a relationship to the observed ratio of [O III]/Hα with stellar mass and

estimate $L_{[OIII]}$ from star formation for individual sources.

However, in our sample at $z \sim 2$, estimating the SF contribution to [O III] is more challenging, as we do not always have high S/N spectroscopic measurements of all of the relevant emission lines for all of our AGN. Initially, we investigated the level of SF contamination for AGN in the BPT diagram, using the method of Kauffmann & Heckman (2009a). Out of the 55 AGN in our sample, 31 have sufficient S/N to place them in the BPT diagram, though one of the two line ratios may be a limit. For these sources, we measure the distance of each AGN from the Kauffmann et al. line. However, we first shift the Kauffmann et al. line ~ 0.1 dex higher in log([O III]/Hβ) to account for the overall offset of the MOSDEF galaxy sample compared to SF galaxies in SDSS (see Figure 3.4 and Section 3.3.4 above); though we note that this shift could be along log([N II]/Hα) as well (see Shapley et al. 2015; Sanders et al. 2016). Figure 3.8 shows the histogram of the distance of each AGN on the BPT diagram in our sample from this modified Kauffmann et al. line.

For the AGN that we can show on the BPT diagram, we find a median distance of 0.17 dex from the modified Kauffmann et al. line. This median point (log([N II]/Hα) = -0.39, log([O III]/Hβ) = 0.36) lies in the Seyfert region of the BPT diagram, so we use the relevant trajectory from Kauffmann & Heckman (2009a) to find the contribution of SF to the [O III] emission. The top x axis in Figure 3.8 shows the fractional star formation contribution to $L_{[OIII]}$. The median contribution for our AGN is $\sim$33%. The purple line in Figure 3.8 roughly shows the distance of the Kewley (2013) line. This indicates that AGN above the Kewley (2013) line should have a fractional SF contamination of less than 20%.

We also estimate the median SF contamination to $L_{[OIII]}$ using the method of Tanaka (2012), as described above and find a median contamination of 30%. However, using this method we find a prohibitively large scatter which unfortunately indicates that

we cannot use this method to apply a correction for SF on a source by source basis.

Here, we use $L_{[\mathrm{OIII}]}$ as a proxy of AGN activity as the majority of the [O III] flux is from the AGN (both methods described above estimate a $\sim 32\%$ contribution from SF activity). Additionally, almost all of the AGN in our sample lie in the AGN region of the BPT diagram (for optical AGN this is by definition), which indicates their emission lines are dominated by AGN radiation rather than SF. We do not correct $L_{[\mathrm{OIII}]}$ for SF contamination here, as we cannot apply the Kauffmann & Heckman (2009a) method since it requires reliable detections for each emission line, and using the Tanaka (2012) method results in a substantial additional scatter. As we discuss below in Section 3.4, any trends that we find with $L_{[\mathrm{OIII}]}$ are also confirmed with L_{X} in our X-ray detected sample, such that none of our results should be substantially impacted by SF contamination to [O III] .

3.4 Results

In this section we consider AGN identification at different wavelengths and investigate AGN selection biases and host galaxy properties for different identification techniques. We first compare the luminosities of AGN selected at X-ray versus optical wavelengths. We then compare AGN host galaxy properties, such as SFR, dust content and stellar age, to a sample of inactive galaxies with the same distribution of stellar mass as the AGN host galaxies. Finally, we investigate the relationship between AGN activity and SFR in individual AGN host galaxies at $z \sim 2$. We emphasize that for any analysis with [O III] measurements we restrict our sample to sources with $> 3\sigma$ [O III] $\lambda 5008$ detections, which includes 34 AGN and 374 galaxies.

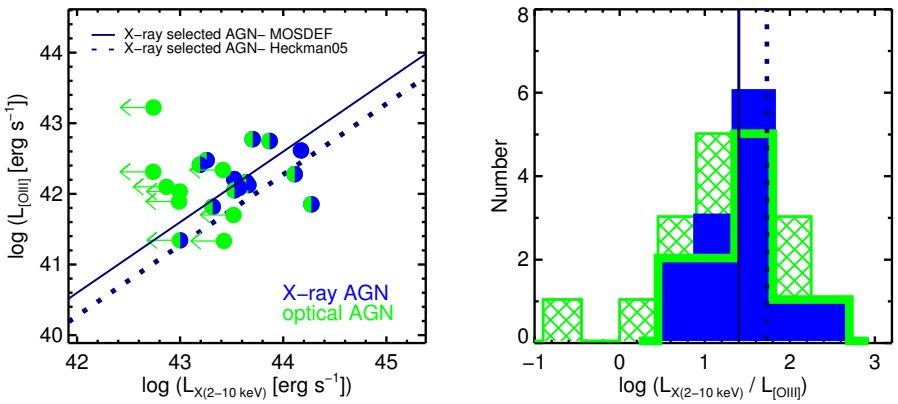

Figure 3.9. *Left:*$L_{[\mathrm{OIII}]}$ versus $L_{\mathrm{X}(2-10\ \mathrm{keV})}$ for X-ray (blue) and optical (green) AGN. The arrows shows an upper limit on $L_{\mathrm{X}(2-10\ \mathrm{keV})}$ for sources without X-ray detection. The solid light blue line shows the average $\log(L_{\mathrm{X}}/L_{[\mathrm{OIII}]})$ (1.40 dex, with 0.44 dex standard deviation) for X-ray AGN in MOSDEF while the dotted blue line shows the ratio (1.73 dex, with 0.41 dex standard deviation) for a sample of X-ray selected AGN in Heckman et al. (2005). *Right:* The distribution of $\log(L_{\mathrm{X}}/L_{[\mathrm{OIII}]})$ for X-ray AGN and optically selected AGN in MOSDEF. The solid green histogram indicates $\log(L_{\mathrm{X}}/L_{[\mathrm{OIII}]})$ for the optically selected AGN with X-ray identification, and the hashed histogram includes X-ray limits as well.

3.4.1 The Relationship between X-ray and Optical Emission

In this section, we address whether we can recover AGN that are absorbed at X-ray wavelengths by comparing L_{X} and $L_{[\mathrm{OIII}]}$ measurements for our samples of X-ray and optical AGN.

The [O III] λ5008 line, as one of the strongest narrow optical emission lines, provides a robust tracer of AGN power and (at least at lower redshifts) is less contaminated by emission due to star formation activity than the Hα line (e.g. Heckman et al. 2004; Brinchmann et al. 2004). The hard band X-ray emission is also a robust estimator of AGN power and can penetrate regions with low to moderate hydrogen column densities. However, X-ray emission will be suppressed in Compton thick or highly obscured AGN. Low luminosity AGN may also be missed due to the flux limit of the X-ray data especially towards the edges of the X-ray pointings.

In Figure 3.9 (left panel) we show $L_{[\mathrm{OIII}]}$ versus $L_{\mathrm{X}(2-10\ \mathrm{keV})}$ for X-ray (blue cir-

cles) and optically selected (green circles) AGN in MOSDEF. For the optical AGN that do not have X-ray detections in the hard band, we use the upper limits on $L_{\mathrm{X}(2-10\ \mathrm{keV})}$ Here we consider only AGN with significant [O III] λ5008 detections.[1] The blue solid line shows the average $\log(L_{\mathrm{X}}/L_{[\mathrm{OIII}]})$ for X-ray AGN in MOSDEF. The dotted line shows the measurement of $\log(L_{\mathrm{X}}/L_{[\mathrm{OIII}]})$ for an X-ray selected sample at $z < 0.2$ by Heckman et al. (2005).

We note that the AGN [O III] λ5008 luminosity in our sample is corrected for dust reddening. To determine the correction factor, we calculate the color excess from the Balmer decrement and combine this with the value of the MOSDEF dust attenuation curve at 5008 Å(Reddy et al. 2015). This correction results in an average increase of $\sim$ 0.17 dex in [O III] luminosity for the AGN in our sample. The [O III] luminosities from Heckman et al. (2005) are not corrected for dust reddening. We also note that the X-ray selected AGN in the Heckman et al. (2005) sample are detected in the 3–20 keV hard X-ray band, and we converted their luminosity to $L_{\mathrm{X}(2-10\ \mathrm{keV})}$ assuming Γ =1.9.

In the right panel of Figure 3.9 we show the distributions of $\log(L_{\mathrm{X}}/L_{[\mathrm{OIII}]})$ for X-ray and optical AGN samples. For the X-ray selected AGN in MOSDEF, the average $\log(L_{\mathrm{X}}/L_{[\mathrm{OIII}]})$ is 1.40 dex (with a standard deviation of 0.44 dex). This measurement is consistent with the average ratio in Heckman et al. (2005) (1.73 dex with a standard deviation of 0.41 dex), considering the uncertainties and the lack of the reddening correction in Heckman et al. (2005). Trouille & Barger (2010) with a larger sample of X-ray selected AGN at $z < 0.85$ also find a similar average $\log(L_{\mathrm{X}}/L_{[\mathrm{OIII}]})$ (1.46 dex, with 0.6 dex standard deviation), and indicate that the fraction of X-ray AGN that are not identified in optical diagnostics varies between 20-50% depending on the line used for classifying optical AGN (Kauffmann et al. 2003a versus Kewley et al. 2001). Trouille

[1]The [O III] line for sources not shown in this figure is not necessarily low flux; in many cases it is simply impacted by a sky line. We also note that even if we do not detect [O III] for a given source, we can still in some cases optically identify it as an AGN, if it has a high [NII]/Hα ratio.

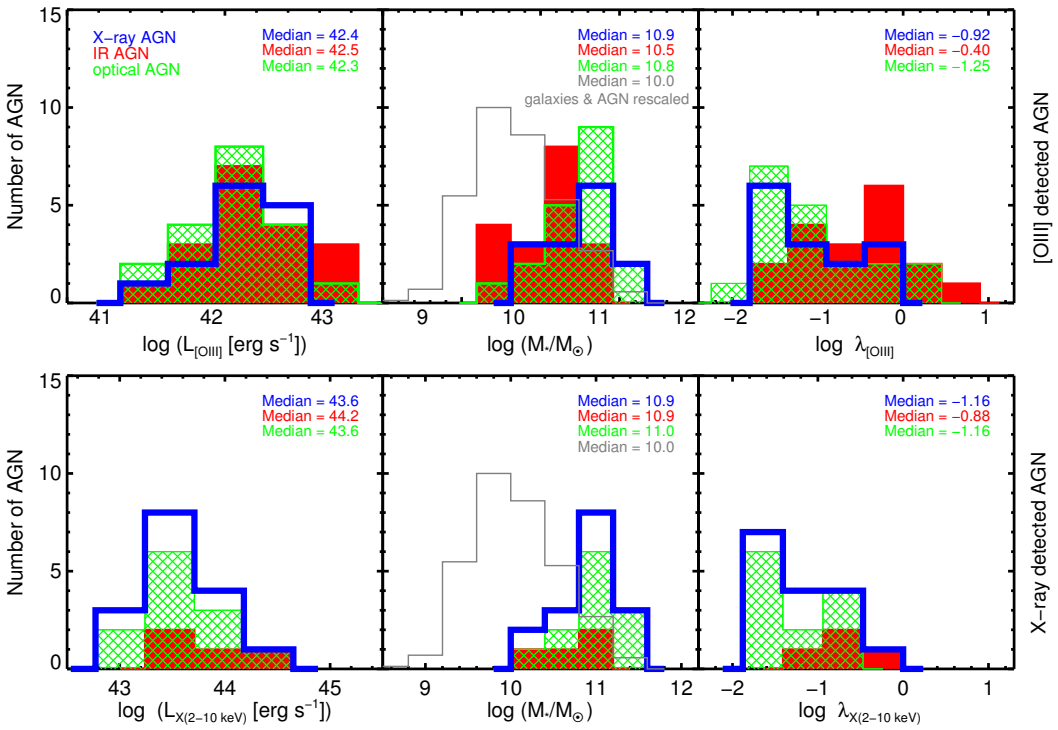

Figure 3.10. The observed luminosity (*left*), stellar mass (*center*), and specific accretion rates (*right*) distributions of X-ray (blue), IR (red), and optical (green) AGN with significant [O III] detection in top row and significant hard X-ray detection in the bottom row. The median values are given in each panel. AGN selected at all three wavelengths in our sample have very similar $L_{[OIII]}$ (and L_X) distributions (left panels). In the middle panels the gray histograms indicate the stellar mass distributions of our entire sample (galaxies and AGN). The stellar mass distributions clearly reflect the bias against AGN identification in low mass galaxies.

& Barger (2010) argue that this misidentification could be due to the complexity of the structure of the narrow-line region, which could result in escape of many of the ionizing photons, and therefore lower $L_{[OIII]}$ in some sources.

Considering a sample of optically selected AGN,[2] Heckman et al. (2005) find a large scatter in $\log(L_X/L_{[OIII]})$ and identify a population of type 2 AGN that are bright at [O III] λ5008 but under-luminous in X-ray. As shown in Figure 3.9, in MOSDEF we only identify two AGN with low $\log(L_X/L_{[OIII]})$ indicating the X-ray emission is heavily

[2]We note that the optical AGN in Heckman et al. (2005) are selected based on an [O III] λ5008 flux limit rather than the BPT diagram.

obscured.

The bulk of optically selected AGN in our sample have a similar $\log(L_X/L_{[OIII]})$ to the X-ray selected sample. The majority of optically selected AGN with limits on L_X still follow the overall $\log(L_X/L_{[OIII]})$ trend and are consistent with being intrinsically lower luminosity AGN. Thus at $z \sim 2$ the optical selection method is effective at identifying lower luminosity AGN that may be missed by X-ray surveys due to the limited (and variable) depth of the X-ray data. However, deeper X-ray data could reveal that these sources are under-luminous at X-ray wavelengths and thus are candidate obscured AGN.

Overall, we find that the relationship between L_X and $L_{[OIII]}$ in our sample at $z \sim 2$ is consistent with that of the Heckman et al. (2005) local X-ray AGN sample. However, only $\sim$50% of our optically selected AGN are detected at X-ray wavelengths (see also Figure 3.5). In part, this is due to the fact that the X-ray data does not have uniform depth across our fields, unlike the more uniform [O III] sensitivity in the MOSDEF spectra. Thus, at these redshifts, optical selection may be more effective at identifying AGN, especially lower luminosity sources, but does not obviously identify significant populations of heavily absorbed AGN. We also find that $\sim$75% of the X-ray AGN are selected at optical wavelength, indicating that optical selection is relatively complete but can miss some AGN that are found by X-ray surveys. This is mainly due to contamination of the optical spectra at $z \sim 2$ from the sky lines, as we discuss below in Section 3.5.1.

3.4.2 AGN Luminosities and Specific Accretion Rates

To further investigate the differences between AGN samples identified at different wavelengths at $z \sim 2$, in Figure 3.10 we compare the distributions of AGN luminosities (left panels), host stellar masses (central panels), and specific accretion rates (right panels) for our samples of X-ray AGN (blue), IR AGN (red) and optical AGN (green). In the middle panels, we additionally show the rescaled histogram of the stellar mass

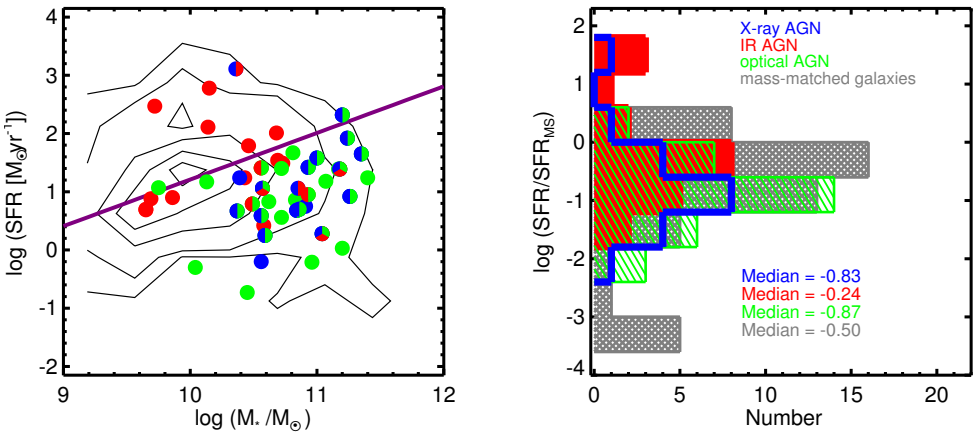

Figure 3.11. *Left:* SFR versus stellar mass for the full MOSDEF galaxy sample (contours) and X-ray (blue), IR (red), and optically-selected (green) AGN host galaxies. The purple line shows the relation from Shivaei et al. (2015) for the main sequence of star formation of MOSDEF galaxies at $z < 2.6$. Compared to the full galaxy sample, AGN host galaxies span a similar range of SFR but a more limited range of stellar mass. *Right:* The SFR/SFR$_{\rm MS}$ distributions in a stellar mass-matched inactive galaxy sample (gray) compared to the various AGN samples. The median SFR/SFR$_{\rm MS}$ are given for each population. IR AGN appear to be biased towards higher SFR/SFR$_{\rm MS}$. Based on the KS test, we find that the IR AGN have a different distribution of SFR/SFR$_{\rm MS}$ (at the $> 2\sigma$ equivalent confidence level) compared to either the optical AGN ($p = 0.004$) or the X-ray AGN ($p = 0.02$) samples.

distribution of our entire galaxy and AGN sample that includes 531 sources in gray. In the top row of Figure 3.10, we show only those sources with a significant [O III] flux in the MOSDEF data (and thus measured $L_{\rm [OIII]}$), which results in a sample of 34 sources. In the bottom row of Figure 3.10, we show only those sources with a significant hard X-ray detection (and thus measured $L_{\rm X}$), resulting in a sample of 16 sources (after excluding broad-line AGN and sources with soft band detections only). As noted above, a single source can be identified as an AGN at X-ray, IR and optical wavelengths, therefore the same object can be included in multiple distributions here. By construction, all sources in the bottom panels are identified as X-ray AGN, whereas in the top panels we include sources identified as X-ray and IR AGN where we are able to measure $L_{\rm [OIII]}$ but do not identify the source as an AGN based on our BPT diagnostics.

The specific accretion rate (shown in the right panels of Figure 3.10) traces the rate of SMBH growth relative to the stellar mass of the host galaxy, providing an indicator of how rapidly a galaxy is growing its black hole (see Aird et al. 2012). By calculating specific accretion rates, we can account for any differences in the stellar masses of the host galaxies of AGN selected at different wavelengths, revealing differences in the types of AGN that are selected with each method that may not be apparent from the observed luminosities.

The specific accretion rate is calculated from either the $L_{[\mathrm{OIII}]}$ or L_{X} and is given by

$$\lambda_{\mathrm{band}} = \frac{k_{\mathrm{band}} L_{\mathrm{band}}}{1.3 \times 10^{38} \times 0.002 \frac{M_*}{M_\odot}} \tag{3.8}$$

where k_{band} is the corresponding bolometric correction. We adopt a single bolometric correction at each wavelength. At optical wavelengths we use a mean bolometric correction of 600 from Kauffmann & Heckman (2009a), which corresponds to the mean correction for extinction-corrected [O III] λ5008 luminosity (see also Netzer 2009; LaMassa et al. 2010). For sources with X-ray detections we use a constant bolometric correction of $k_{\mathrm{X}(2-10\,\mathrm{keV})} = 25$. We also estimated the bolometric luminosity using the luminosity-dependent bolometric corrections from Hopkins et al. (2007) and Lusso et al. (2012) for type 2 AGN, but this does not alter the overall trends seen in Figure 3.10 when using a single bolometric correction. The denominator in the above equation is chosen such that the units of λ_{band} approximately correspond to the Eddington ratio (assuming a single scaling between SMBH mass and total stellar mass).

For AGN with significant [O III] detections, the median statistical uncertainties on $L_{[\mathrm{OIII}]}$, stellar mass, and $\lambda_{[\mathrm{OIII}]}$ are 0.04 dex, 0.10 dex, and 0.12 dex, respectively. For AGN with X-ray detections, the median uncertainties on L_{X} , stellar mass, and λ_{X} are 0.20 dex, 0.07 dex, and 0.23 dex. However, there may be additional uncertainties in

$\lambda_{[OIII]}$ and λ_X from the bolometric corrections (which may depend on Eddington ratio, see Vasudevan & Fabian 2007) that could result in larger uncertainties.

We use a Kolmogorov–Smirnov (KS) test to compare the distributions shown in Figure 3.10 for the different AGN selections and assess if there are significant differences (requiring a p-value < 0.05, corresponding to a $> 2\sigma$ equivalent confidence level). Based on our KS tests, we find no evidence for significant differences in the distributions between any two samples, indicating that the distributions of luminosities, host stellar masses and specific accretion rates for X-ray, IR, and optical AGN are all statistically consistent with being drawn from the same parent population.

However, the lack of significant differences could be due to our relatively small sample sizes. In Figure 3.10 there are indications of differences in these distributions, probed here for the first time at $z \sim 2$, that appear consistent with previously identified selection biases at lower redshifts (e.g. $z \sim 0.1 - 1$: Mendez et al. 2013). In general, there is a bias against AGN identification in relatively low mass galaxies. For IR selection there may be an additional bias against the most massive galaxies in our sample. IR selection appears to identify AGN with, on average, lower stellar masses and higher specific accretion rates i.e., sources where the light from the AGN dominates over the host galaxy.

X-ray selection is able to probe low specific accretion rates which may introduce a bias toward higher stellar mass host galaxies (e.g. Aird et al. 2012, due to the X-ray flux limits, low specific accretion rate sources will not be identified in lower mass galaxies). Optical selection—a key additional probe with our MOSDEF sample—appears to identify AGN with similar properties to the X-ray selected population i.e., down to low specific accretion rates and generally in higher stellar mass galaxies.

Overall, our results show that with optical diagnostics we are able to identify less powerful, low accretion rate AGN that may not be identified at other wavelengths

(either due to obscuration or limited sensitivity). We also find that IR AGN selection preferentially identifies powerful AGN that are hosted in relatively lower mass galaxies, compared to optical and X-ray AGN selection. Each of these identification methods at different wavelengths are incomplete and suffer from selection biases, therefore a combination of identification methods can provide a more complete picture of AGN properties.

3.4.3 AGN Host Galaxy Properties

In this section we investigate the properties of the host galaxies of our AGN samples in more detail and compare with a sample of inactive galaxies from MOSDEF.

The MOSDEF galaxy sample spans a wide range in SFR ($-1 \lesssim \log(\frac{\mathrm{SFR}}{\mathrm{M_\odot\ yr^{-1}}}) \lesssim 3$) and stellar mass ($8 \lesssim \log(\frac{\mathrm{M_*}}{\mathrm{M_\odot}}) \lesssim 12$). From the data in the first two years of the MOSDEF survey, we identify 481 galaxies with an average stellar mass of $\sim 10^{10}$ $\mathrm{M_\odot}$. While the AGN host galaxies span the full range of SFRs of the galaxy sample, they span a more limited range in stellar mass (less than 2 orders of magnitude) with an average stellar mass of $10^{10.6}$ $\mathrm{M_\odot}$ for their host galaxies. The observational bias against AGN identification (at any wavelength) in low mass galaxies restricts our AGN sample to relatively massive host galaxies (e.g. Aird et al. 2012).

Since stellar mass correlates with other physical properties such as metallicity, age, and SFR of the galaxy, we construct a stellar mass-matched control sample of inactive galaxies for comparative analysis with the AGN host galaxies. To create this sample, we bin the AGN host galaxies in narrow intervals of $\Delta\log(\frac{\mathrm{M_*}}{\mathrm{M_\odot}}) = 0.05$ dex and select 50 inactive galaxies from the full galaxy sample to create a sample with the same stellar mass distribution as the AGN host galaxies.

In the left panel of Figure 3.11, we show the SFR versus stellar mass distributions of AGN (colored points) in MOSDEF compared to the full galaxy sample (contours).

There is a well known, positive correlation between the SFR and stellar mass of galaxies, known as the "main sequence" of star formation (e.g., Elbaz et al. 2007b; Noeske et al. 2007b; Karim et al. 2011; Whitaker et al. 2012; Shivaei et al. 2015). The purple line in this figure shows the relation for the main sequence of star formation, based on SED fitting, for MOSDEF galaxies at $1.4 < z < 2.6$ from Shivaei et al. (2015):

$$\log(\frac{\mathrm{SFR}}{\mathrm{M}_\odot\ \mathrm{yr}^{-1}}) = (0.80 \pm 0.05) \times \log(\frac{M_*}{M_\odot}) - (6.79 \pm 0.55) \tag{3.9}$$

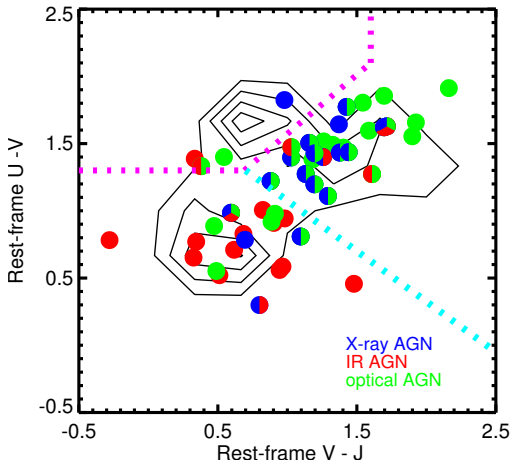

Figure 3.12. The rest-frame U-V versus V-J color diagram, where contours shows mass-matched inactive galaxies and the blue, red, and green circles show X-ray, IR, and optical AGN. The dotted magenta line isolates quiescent galaxies using criteria from Williams et al. (2009), while the dotted cyan line shows the demarcation from Kriek et al. (2015) for dividing dusty versus less dusty star-forming galaxies. Considering the errors in Table 3.1, the fraction of AGN in each part is not significantly different than their mass-matched galaxies. Comparing the fraction of IR and optical AGN indicates that a higher fraction of IR AGN are in less dusty star-forming region (at 3.8σ significance) and a higher fraction of optical AGN are in dusty star-forming region (at 4.2σ significance).

Figure 3.11 shows that AGN exist in galaxies over the full range of SFR probed by the MOSDEF sample. We find that the majority of optical and X-ray AGN host galaxies lie below the main sequence of star formation, while IR AGN host galaxies are found both above and below the main sequence.

In the right panel of Figure 3.11, we show the distribution of SFR/SFR$_{MS}$ which is the relative offset of the SFR from the main sequence at the stellar mass of the host galaxy. We additionally show the SFR/SFR$_{MS}$ distribution for our mass-matched inactive galaxy sample. The median SFR/SFR$_{MS}$ for each sample is given in the figure. The median statistical uncertainty on log(SFR/SFR$_{MS}$) for AGN is 0.23 dex and 0.34 dex for the mass-matched galaxies. A KS test shows that the SFR/SFR$_{MS}$ distribution of the AGN host galaxies is not significantly different from our stellar mass-matched inactive galaxy sample. We further consider three control samples of inactive galaxies, each mass-matched with AGN identified at each wavelength, and compare the physical properties of individual AGN population with their mass-matched galaxies. We find that the distribution of SFR/SFR$_{MS}$ for each AGN sample is consistent with their inactive mass-matched galaxies. Comparing between the various AGN samples (using KS tests), we find that the distributions of SFR/SFR$_{MS}$ of X-ray and optical AGN are statistically consistent with each other. However, we find the distribution of SFR/SFR$_{MS}$ for IR AGN is different at (at the $> 2\sigma$ equivalent confidence level) compared to the optical AGN ($p = 0.004$) or the X-ray AGN ($p = 0.02$) samples.

To further investigate the host galaxy properties, we consider the rest-frame U–V versus V–J color diagram (UVJ color). This diagram is commonly used to distinguish quiescent galaxies from star-forming galaxies with different dust content (e.g Williams et al. 2009; Whitaker et al. 2011; Muzzin et al. 2013). To estimate rest-frame colors we use the EAzY code (Brammer et al. 2008) by interpolating between the observed photometric bands (see Kriek et al. 2015), with the AGN contributions subtracted. In Figure 3.12 we show our AGN (colored points) in UVJ space, along with mass-matched MOSDEF galaxies (contours). The dotted magenta line in this figure shows the region isolating the quiescent galaxies, identified using criteria from Williams et al. (2009):

Table 3.1. The fraction of AGN and, stellar mass-matched galaxies in different parts of UVJ space

Region	AGN	mass-matched galaxies
quiescent	$8\% \pm 4\%$	$14\% \pm 4\%$
less dusty SF	$39\% \pm 7\%$	$49\% \pm 6\%$
dusty SF	$53\% \pm 7\%$	$37\% \pm 6\%$

$$U - V > 1.3 \tag{3.10}$$

$$U - V = 0.88 \times (V - J) + 0.69 \tag{3.11}$$

$$V - J < 1.6 \tag{3.12}$$

The cyan dotted line shows the demarcation from Kriek et al. (2015) that divides star-forming galaxies into those that are red and dusty from those that are blue and less dusty.

Table 3.1 indicates the fraction of AGN in each region of UVJ space, compared to the fractions of our mass-matched galaxy sample that fall in each region. The errors on the fractions are estimated from bootstrap resampling. Given the errors, there is not a significant difference between the fractions of AGN and mass-matched galaxies in different regions of UVJ space.

The location of galaxies in UVJ space depends sensitively on stellar mass; in particular within the star-forming population, dusty galaxies are more massive (e.g

Williams et al. 2010). Here, we find that AGN have a similar distribution in UVJ space to a stellar mass-matched inactive galaxy sample. Figure 3.12 also shows that the majority of optical AGN (73%) and X-ray AGN (72%) are identified in dusty star-forming galaxies, while the majority of the IR AGN are identified in less dusty star-forming galaxies (68%).

Considering the sensitivity of the UVJ diagram to stellar mass, and the fact that each AGN population has a different mass distribution, we compare the distribution of UVJ colors for each of our three AGN samples to an appropriately mass-matched galaxy sample. For the X-ray and IR AGN samples we find that their distribution in UVJ space is consistent with their corresponding mass-matched galaxy sample, indicating that the higher density of IR-AGN in the non-dusty star-forming region in Figure 3.12 can be attributed to the lower stellar masses (on average) of the hosts of IR-selected AGN. The fraction of optical AGN in the dusty star-forming region is higher than their mass matched galaxies (at 2.9σ significance), which we discuss below in Section 3.5.

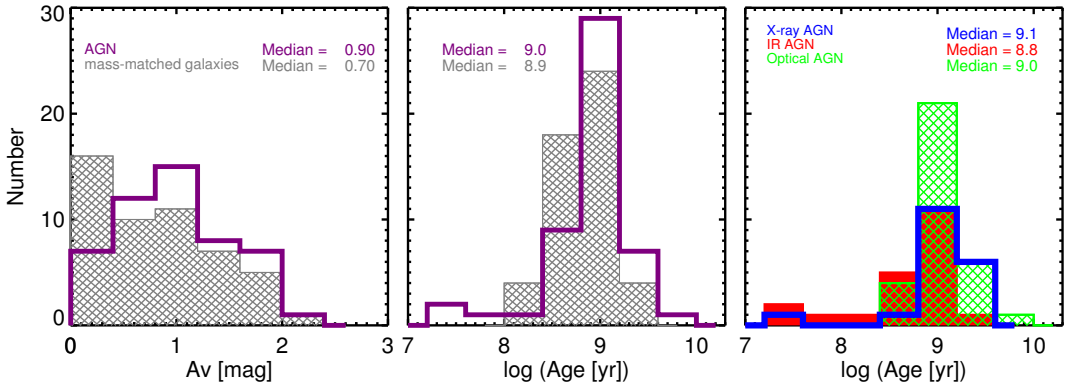

Figure 3.13. *Left:* The dust extinction (A_v) distributions; *Middle:* The stellar age distribution for full MOSDEF AGN (purple) and mass-matched galaxy samples (grey). The KS test shows that the AGN and mass-matched galaxy samples have statistically similar A_v and age distributions. The median values with the standard errors are given for each population. *Right:*The stellar age distribution in each AGN population. IR AGN reside in galaxies with younger stellar population compared to the optical AGN host galaxies at $> 2\sigma$ significance ($p = 0.02$).

In Figure 3.13 we compare the dust extinction and stellar age derived from SED

fitting (after subtracting the AGN contribution) for AGN host galaxies with the mass-matched inactive galaxies. We illustrate the distributions of visual extinction (A_V) (left panel) and stellar age (middle panel) for AGN and mass-matched galaxies. Additionally, we show the distributions of stellar age for individual AGN populations in the right panel. The median values of each distribution are given in the figure. The median statistical error on A_V is 0.40 magnitudes for the AGN and 0.30 magnitudes for the mass-matched galaxies. The median error on log(stellar age) is 0.30 dex for the AGN and 0.13 dex for the mass-matched galaxies.

The full (non mass-matched) MOSDEF galaxy sample has a median A_V=0.5 magnitude and a median stellar age of $10^{8.6}$ yr, with distributions in A_V and stellar age that are significantly different from the AGN sample. The median dust extinction and age are very similar in AGN and mass-matched inactive galaxies populations, and KS tests show that the two populations do not have statistically different distributions in either parameter. The similarity of these distributions is not entirely unexpected, given that there are strong correlations between stellar mass and both extinction and stellar age.

We note that stellar age estimation is sensitive to various parameters in SED fitting, in particular, the star formation history models. However, the distribution of τ (the characteristic star formation timescale) for the MOSDEF AGN is not significantly different from the distribution of τ for the mass-matched galaxies. We also find a similar *joint* distribution in stellar age and dust extinction between the AGN and mass-matched galaxies, in that galaxies with younger stellar populations are dustier than galaxies with older stellar populations.

In the right panel of Figure 3.13 we show stellar age distributions for the separate AGN populations in our sample and find a median stellar age of $\sim$ 1.3 Gyr, 630 Myr and 1 Gyr, respectively, for X-ray, IR and optical AGN. KS tests show a 2σ (p=0.02) significance level difference in their age distributions that is most likely due to the stellar

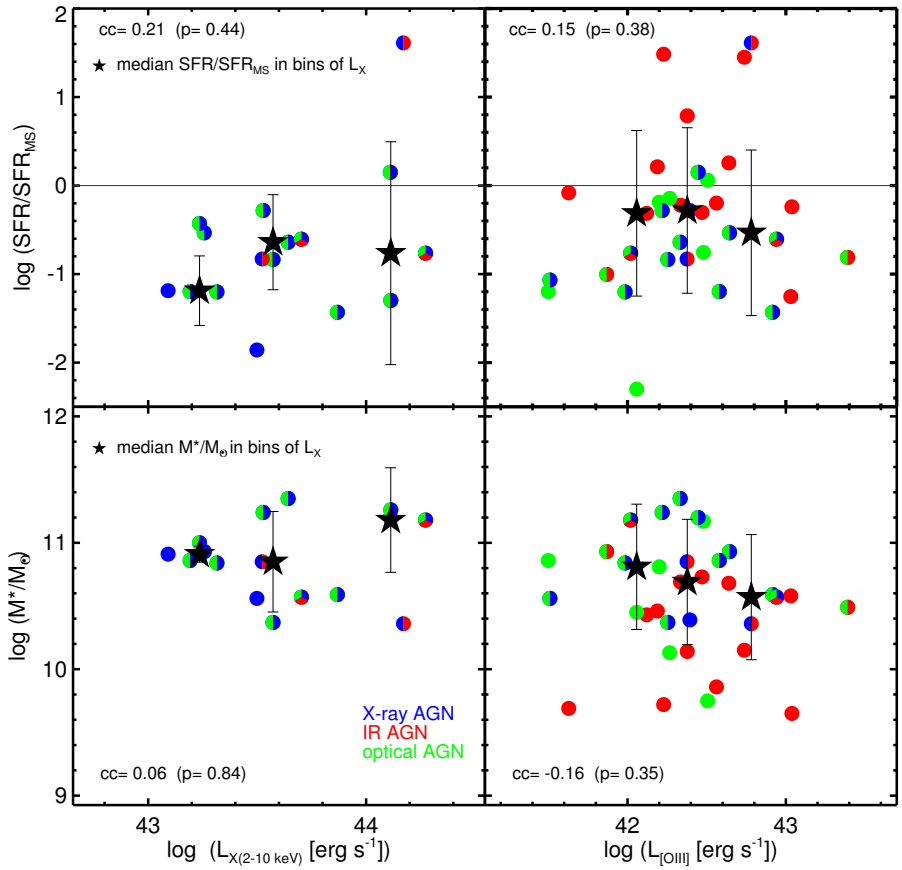

Figure 3.14. Left: The AGN host galaxy SFR relative to the main sequence of SFR (SFR/SFR$_{MS}$, top) and host galaxy stellar mass (bottom) as a function of L_X (left) and $L_{[OIII]}$ (right, for AGN with significant [O III] detections). The X-ray, IR and optical AGN are shown respectively with blue, red and green circles; the black stars indicate the median SFR/SFR$_{MS}$ and stellar mass in bins of L_X (or $L_{[OIII]}$), with the error bars showing the standard deviation on the median values. The purple horizontal line in the upper panels shows the main sequence of star formation, based on SED fitting, for MOSDEF galaxies at $1.4 < z < 2.6$ from Shivaei et al. (2015), used here to define a SFR/SFR$_{MS}$ of zero. The correlation coefficients are given in each panel.

mass selection biases, with IR AGN being identified in relatively lower mass galaxies, compared to optical and X-ray AGN.

Overall, our results indicate that the distributions of SFR, dust, and stellar age in AGN and mass-matched inactive galaxies are very similar, and that the key parameter in finding these similar distributions is the stellar mass of both populations. Stellar mass also plays an important role in AGN identification. While IR AGN are biased against

the most massive galaxies, we can identify them in less dusty galaxies with younger stellar population and relatively high star formation activity. In contrast, optical AGN are identified in dusty massive galaxies with older stellar populations and lower star formation activity.

3.4.4 The Relationship between Star Formation and AGN Activity

We now investigate whether there is a connection between star formation activity and AGN activity for individual sources in our $z \sim 2$ sample. To trace the AGN activity we use L_X for those AGN with X-ray detections and $L_{[OIII]}$ for AGN with significant [O III] measurements. To quantify the relation between AGN luminosity and SFR, we calculate the correlation coefficient and the corresponding significance using the $r-correlate$ routine in IDL, which computes the Spearman's rank correlation coefficient (cc) and the significance of its deviation from zero (p).

As noted in Section 3.4.3, the SFRs and stellar masses of galaxies are known to be correlated (e.g., Elbaz et al. 2007b; Karim et al. 2011; Shivaei et al. 2015). Therefore an underlying correlation between AGN luminosity and host galaxy stellar mass, if it existed, could result in a correlation between SFR and AGN luminosity. To take this stellar mass-dependent effect into account, instead of quantifying any correlation between SFR and AGN luminosity, we use SFR/SFR$_{MS}$ (the relative offset of the SFR from the main sequence at the stellar mass of the host galaxy). We use equation 3.9, which defines the star-forming main sequence for the MOSDEF sample for galaxies at $1.4 < z < 2.6$ from Shivaei et al. (2015).

In Figure 3.14, we show SFR/SFR$_{MS}$ versus L_X for X-ray AGN host galaxies in the top left panel and stellar mass versus L_X in the lower left panel. The right panels show SFR/SFR$_{MS}$ versus $L_{[OIII]}$ (top) and stellar mass versus $L_{[OIII]}$ (bottom) for AGN with 3σ [O III] detections. We also show the median SFR/SFR$_{MS}$ and stellar mass in bins of

L_X and $L_{[OIII]}$ with the black stars, where the error bars indicate the standard deviation of the median in each luminosity bin. As shown in the figure, we find no significant correlation between SFR/SFR$_{MS}$ and either L_X or $L_{[OIII]}$.

We note again that we have not accounted for any contribution to $L_{[OIII]}$ from star formation in our sample, as we are unable to correct for this on a source by source basis. In general, there is a positive correlation between SFR and [O III] emission in the galaxy population (e.g. Mehta et al. 2015). Although we do not find a significant correlation between SFR/SFR$_{MS}$ and $L_{[OIII]}$ here, the possible contribution from star formation to $L_{[OIII]}$ could produce a correlation and should thus be considered in any future studies with larger samples.

Overall, we do not find any significant correlations between SFR and AGN luminosity in our sample. However, a common gas supply for triggering and fueling both of these phenomena could play an important role in galaxy and AGN growth. With a larger sample (and the possibility of correcting $L_{[OIII]}$ for star formation contributions), the connection between the growth of SMBHs and their host galaxies can be investigated more accurately.

3.5 Discussion

In this paper we use data from the first two years of the MOSDEF survey, which includes 55 AGN identified with X-ray, IR, and/or optical diagnostics at $z \sim 2$.

We investigate the selection of these AGN and their host galaxies properties. Below we first discuss the uniqueness and overlap of AGN identification at different wavelengths and summarize the selection biases of each identification method. We further compare the host galaxy properties of the AGN in our sample with other studies in the same redshift regime. Finally, we discuss our ability to probe the coeval growth of SMBHs and galaxies at $z \sim 2$ with this dataset.

3.5.1 Uniqueness and Overlap of AGN Identified at Different Wavelengths

Our sample of 55 AGN at $z \sim 1.4$–3.8 identified using X-ray, IR and/or optical diagnostics allows us to quantify the uniqueness and overlap of AGN selection at different wavelengths. The numbers of AGN identified at different wavelengths and the overlap between the samples are shown by the Venn diagram in Figure 3.5. As shown in this figure, roughly half of the IR AGN sample and almost half of optical AGN sample are *not* identified as AGN at the other wavelengths. X-ray AGN identification provides important confirmation of AGN selected at other wavelengths, but in our sample it does not uniquely identify many additional AGN to those identified at MIR and optical wavelengths.

The number of AGN recovered at each wavelength depends on the depth of the observational data available at that wavelength. To investigate the differing depths of our observations, we compare the bolometric luminosity for AGN identified at each wavelength. We adopt a single bolometric correction at each wavelength. As mentioned in Section 3.4.1, we adopt $k_{\mathrm{X}(2-10\,\mathrm{keV})} = 25$ and $k_{[\mathrm{OIII}]} = 600$ respectively for sources with X-ray detections and significant [O III] detections. At MIR wavelengths we adopt the average bolometric correction from Richards et al. (2006) at 5.8 μm, giving $k_{\mathrm{IR}} = 8$. Although a single bolometric correction is likely an oversimplification, it is sufficient for our purposes to compare the effective depths of the data at different wavelengths. The median bolometric luminosities are $L_{bol(X)} = 10^{45.1}$ erg s^{-1} for sources with X-ray detections, $L_{bol([OIII])} = 10^{45.2}$ erg s^{-1} for sources with significant [O III] detections and $L_{bol(IR)} = 10^{45.3}$ erg s^{-1} for sources with 5.8 μm detections. The similar median bolometric luminosities indicate that our data are reaching similar depths at each wavelength. However, there are AGN identified at a single wavelength that are not recovered at other wavelengths. Are these AGN intrinsically less luminous at other wavelengths or is their unique identification due to another observational bias?

While X-ray imaging is a robust method for identifying AGN with hydrogen column densities up to $N_H \approx 10^{23-24}$ cm^{-2}, X-ray emission cannot penetrate higher column densities and will therefore not identify Compton-thick AGN. In addition, variation of the depth of *Chandra* observations in our various fields as well as a changing effective depth within a field results in a non-uniform flux limit (see, e.g., Mendez et al. 2013). Therefore, X-ray imaging may miss AGN that are identified at other wavelengths. Furthermore, X-ray selection is not expected to identify many AGN that cannot be recovered at other wavelengths with sufficiently deep data. Indeed, in MOSDEF we find that the majority (87%) of X-ray AGN are also recovered with IR or optical methods.

We find that 75% of our X-ray AGN are recovered at optical wavelengths. There are six X-ray AGN that are *not* identified at optical wavelengths: four of these sources have low S/N optical emission lines that are contaminated by sky lines; one of these sources is at $z > 3$ where Hα and [N II] fall beyond the wavelength coverage of MOSFIRE and therefore cannot be placed on the BPT diagram; and one source is on the star-forming sequence in the BPT diagram, indicating that it has a high SFR relative to the AGN luminosity and could therefore not be identified as an optical AGN. We thus conclude that optical AGN selection could identify the majority of X-ray selected AGN and is mainly limited by the quality of the spectroscopic data. However, this method is likely biased against AGN in host galaxies with high SFRs (e.g. Coil et al. 2015) as sources with higher SFR move towards the star formation locus on the BPT diagram.

Slightly less than half (42%) of the optical AGN in our sample are not identified at X-ray or IR wavelengths, the majority in fields with relatively shallow X-ray data. These differences likely reflect the non-uniform depths probed by the X-ray data, compared to the fairly uniform depth at [O III] probed with the MOSDEF spectra. Also, as the Donley et al. (2012) selection is very incomplete, these optical AGN are not identified using our IR selection criteria. Thus, optical selection can potentially identify substantial

populations of AGN that are missed at other wavelengths.

There are 13 IR AGN in our sample that are not selected at X-ray or optical wavelengths. Although these sources have significant [O III] fluxes, they cannot be classified as optical AGN for various reasons. All of these sources either do not have observations of Hα and [N II] (typically because they are at $z \gtrsim 3$) or have sky line contamination such that their [N II]/Hα ratio cannot be measured. Based on our upper limits on X-ray luminosities, it appears that these 13 IR AGN are not identified at X-ray wavelengths due to the depths of the available X-ray data; indeed, 11 of these sources are in the COSMOS and AEGIS fields, where we have shallower X-ray data. Thus, IR AGN selection does *not* appear to identify a substantial AGN population (such as heavily obscured sources) that cannot be identified at other wavelengths. However, IR selection provides a more uniform depth than X-ray selection and is not affected by the data quality issues that impact optical selection; thus IR selection can be used to improve the completeness of AGN samples.

Mendez et al. (2013) reached similar conclusions regarding IR AGN selection using a larger sample of AGN at intermediate redshifts ($z < 1.2$), finding that 90% of IR AGN identified with shallow IR data are detected with sufficiently deep X-ray data. As the depth of the IR observations increases, Mendez et al. (2013) find that the fraction of IR AGN that are *not* recovered by X-rays also increases, reflecting the additional IR AGN samples that are identified with extremely deep IR data. Using deep IR data, Donley et al. (2012) find that just 38% of IR AGN in their sample are recovered at X-rays wavelengths, although as the depth of the X-ray data increases this fraction increases to 52% (see also Donley et al. 2007; Hickox et al. 2009). More recently, Cowley et al. (2016) find X-ray counterparts for only $\sim 22\%$ of their IR AGN. Cowley et al. (2016) use the Messias et al. (2012) redshift-dependent IR AGN selection criteria; thus the lower fraction of X-ray counterparts in their work could be either due to shallower X-ray data or the different IR

Table 3.2. The selection biases of X-ray, IR and optical AGN host galaxies in MOSDEF

Host galaxy property	X-ray AGN	IR AGN	optical AGN
Stellar mass	bias towards high mass galaxies	bias towards moderate mass galaxies	bias towards high mass galaxies
SFR	no bias	bias towards relatively higher SFR	bias towards relatively lower SFR
Dust	possible bias towards higher dust content	possible bias towards lower dust content	possible bias towards higher dust content

selection method used.

3.5.2 AGN Selection Biases

As shown above and elsewhere, there are substantial observational selection biases in AGN samples identified at different wavelengths. These biases impact the observed properties of the AGN host galaxies identified.

In terms of X-ray identification, our results indicate that X-ray selection can identify AGN at low specific accretion rates, which results in a selection bias towards massive host galaxies (see Figures 3.10 and 3.11). Indeed, previous studies have extensively shown that AGN identification *at any wavelength* is biased against low mass galaxies (e.g. Kauffmann et al. 2003a; Xue et al. 2010; Aird et al. 2012). This bias has also been seen in various studies of X-ray AGN host galaxies (e.g. Alonso-Herrero et al. 2008; Aird et al. 2012; Azadi et al. 2015). In terms of star formation activity of X-ray AGN hosts, although they are mostly located below the main sequence of star formation, their SFR distribution is not significantly different from that of inactive galaxies with a similar mass distribution, as most galaxies at that high stellar mass are also below the main sequence.

In terms of IR AGN identification, IR AGN selection is biased towards identifying AGN with high specific accretion rates where the AGN IR light dominates over the host galaxy light (Mendez et al. 2013). This selection bias can result in identifying more luminous AGN in moderately massive host galaxies. Using a larger sample at intermediate redshifts, Mendez et al. (2013) find that IR AGN selection mainly identifies high X-ray luminosity AGN, while X-ray selection identifies AGN with a wider range of luminosities. Given that most IR AGN in our sample are not detected at X-ray wavelength we cannot make such a comparison here. We further find that within MOSDEF, IR AGN are found in less dusty host galaxies with relatively younger stellar populations and higher SFRs. This effect can be understood as related to the stellar mass selection biases for IR AGN: IR AGN are identified in lower stellar mass galaxies (compared to X-ray or optical AGN) that tend to have less dust and younger stellar populations than higher mass galaxies.

In terms of optical AGN identification, we find that optical selection can identify lower accretion rate AGN that may not be recovered at other wavelengths. Considering the similar $L_{[OIII]}$ distributions for the various AGN in our sample, this trend is driven by the high stellar masses of the optical AGN host galaxies (see also Coil et al. 2015), similar to X-ray AGN. We further find that optical AGN reside in dusty galaxies with older stellar populations and relatively moderate star formation activity (median $\log(SFR/SFR_{MS})$= -0.87 dex). The higher stellar mass of the optical AGN host galaxies leads to a bias towards higher dust content. It is also more likely for optical AGN to be identified in galaxies with older stellar populations and lower SFR in the BPT diagram (Coil et al. 2015). We further note that the bias towards more massive host galaxies leads to a bias towards higher metallicities, therefore the optical selection method may not be successful in identifying low mass-low metallicity host galaxies (e.g. Groves et al. 2006). We emphasize that although our sample is small, the selection biases of optical AGN against lower mass galaxies with higher SFR has been also reported in studies of optical AGN at

lower redshifts with large samples (Kauffmann et al. 2003a; Trump et al. 2015).

Overall, we find that compared to IR and optical AGN selection techniques, X-ray identification is the least biased, with only a bias towards high stellar mass (but no additional SFR bias). We summarize the various selection biases discussed above in Table 3.2.

3.5.3 MOSDEF Host Galaxy Properties Compared to the Literature

In this study, we find no significant differences between MOSDEF AGN host galaxies and inactive galaxies of the same stellar mass. In particular, we find no significant differences between the star formation activity of AGN host galaxies with the inactive mass-matched galaxies for AGN selected at a given wavelength. Thus, after taking into account of the observational selection biases, we find no evidence that AGN activity is preferentially occurring in a particular type of galaxy, although our relatively small sample size may preclude us from identifying weak trends.

The same result has been seen in some recent studies, e.g. Rosario et al. (2015) find a similar SFR distribution in X-ray AGN hosts and mass-matched galaxies at $z \sim 2$. Bongiorno et al. (2012) also find similar distribution of sSFR for AGN and the inactive galaxies with a slight increase in AGN fraction towards lower sSFR. On the other hand, a number of studies find that AGN are preferentially found in star-forming (main sequence) galaxies at these redshifts. Azadi et al. (2015) perform X-ray sensitivity corrections and find that X-ray AGN are $2-3$ times more likely to be found in galaxies with elevated SFR (see also Aird et al. 2012; Santini et al. 2012; Harrison et al. 2012; Bernhard et al. 2016). Recently, Mullaney et al. (2015) use *Herschel* and *ALMA* measurements and find that the majority of X-ray AGN are *below* the main sequence of star formation, arguing that studies using mean-stacking for SFR measurements can overestimate the level of

star formation in the host galaxies.

The MOSDEF sample does not contain a large number of quiescent galaxies, which lack high S/N emission lines at the observed wavelengths of the survey (Kriek et al. 2015). However, the fraction of our AGN in the quiescent region of UVJ space is similar to the fraction of mass-matched galaxies in that region. With a small number of quiescent galaxies in our sample, the majority of our AGN are in star-forming galaxies which is consistent with the results from other studies at $z \sim 2$. However, to robustly determine whether AGN host galaxies lie preferentially below, above, or along the main sequence of star formation will require larger samples for investigations.

Ellison et al. (2016) considered a sample of multi-wavelength identified AGN at $z \sim 0$, and similar to our results find IR AGN in galaxies with elevated SFR relative to the main sequence and optical AGN in galaxies with lower SFR than the main sequence. Cowley et al. (2016) performed a similar analysis at $z \lesssim 3$, and find that the specific star formation rate (sSFR, $\frac{SFR}{\mathrm{M}_*}$) in AGN host galaxies is, on average, higher than in mass-matched galaxies at $z \gtrsim 2$ for their IR selected AGN sample. No significant differences in sSFR were found for X-ray or radio AGN at these redshifts.

However, in our sample we find a similar sSFR distribution for IR AGN and mass-matched galaxies. As IR AGN in MOSDEF span a similar range of stellar mass as the IR AGN identified in Cowley et al. (2016), the higher sSFR in Cowley et al. (2016) must be due to higher SFR for IR AGN in their sample. Additionally, our investigation shows that the majority of IR AGN in our sample reside in less dusty star-forming galaxies, while Cowley et al. (2016) at $z \gtrsim 2$ find the majority of IR AGN in dusty star-forming galaxies. The different SFR and dustiness of IR AGN in our sample compared to Cowley et al. (2016) could be due to the fact that Cowley et al. (2016) use a combination of IRAC and 24 μm observations for IR AGN identification (see Messias et al. 2012).

We further used the location of AGN host galaxies in UVJ space to investigate

their dust properties. The location of galaxies in UVJ space is very sensitive to stellar mass, with lower mass galaxies residing preferentially in the less dusty star-forming region, and more massive star-forming galaxies in the dusty region (e.g. Whitaker et al. 2011). While the full AGN sample used here shows a similar distribution as mass-matched inactive galaxies in UVJ space, we find that the fraction of optical AGN in the dusty star-forming region is higher than their inactive mass-matched galaxies at the 2.9σ level. However, the X-ray and IR AGN show a very similar behavior to their mass-matched galaxies. Although our optical AGN hosts are predominantly in dusty star-forming galaxies, we note that the A_V of these optical AGN hosts is not significantly higher than in the mass-matched galaxies or non-optical AGN population. Therefore, the difference in the fraction of optical AGN and their mass-matched galaxies in the UVJ diagram could be a statistical fluctuation, rather than due to any intrinsic difference in dust content of the optical AGN host galaxies.

Overall, the AGN in our sample have very similar physical properties to those of mass-matched inactive galaxies. At these redshifts, a larger sample of both quiescent galaxies and AGN are required to study any potential differences between the SFR or dustiness of AGN hosts and inactive galaxies more robustly.

3.5.4 Are the Growth of Black holes and the Growth of their Host Galaxies Correlated at $z \sim 2$?

As discussed in the introduction, the global SMBH accretion rate density and SFR density both peak at $z \sim 2-3$ (e.g., Aird et al. 2015), which indicates that globally there is a relation between the growth of SMBH and their host galaxies. But the question still remains whether such a correlation exists on the scale of individual host galaxies. Our results indicate that $\mathrm{SFR/SFR_{MS}}$ and AGN luminosity are not significantly correlated within our sample, using either L_{X} or $L_{[\mathrm{OIII}]}$ as a probe of AGN activity. Why then, given

the similarity in the global scaling relations, we do not find a correlation?

Due to their stochastic fueling (e.g. Ulrich et al. 1997; Peterson 2001), the luminosities of AGN may undergo dramatic changes in a short time scale (Keel et al. 2012b), while star formation activity remains stable in the host galaxies over long timescales (e.g. Wong 2009; Hickox et al. 2012). Therefore rapid AGN variability can play an important role in washing out any underlying trend that may exist between SFR/SFR_{MS} and AGN luminosity. In fact, studies using average AGN luminosity in bins of SFR, instead of the luminosity of individual AGN, find a positive trend between AGN luminosity and SFR of the host galaxy. (e.g. Chen et al. 2013; Hickox et al. 2014; Azadi et al. 2015; Dai et al. 2015).

Although the connection between galaxy-wide star formation and AGN activity might be hidden due to the variable nature of AGN, Diamond-Stanic & Rieke (2012) find evidence of a strong correlation between AGN luminosity and SFR in the circumnuclear regions ($r < 1$ kpc). Thus, while our results do not show a significant correlation between the large-scale star formation and AGN activity, these phenomena may have an underlying connection through a common gas supply. We note that violent events such as major mergers can provide a gas influx to fuel both AGN activity and star formation. However, the moderate luminosity of AGN in our sample indicate that these sources are generally at lower luminosities than those thought to be triggered by major mergers (e.g. Schawinski et al. 2012; Treister et al. 2012).

As discussed above in Section 3.3.6, AGN and star formation activity in the host galaxy can both contribute to the [O III] luminosity. In the local Universe studies have proposed various methods for estimating the contribution from star formation to the [O III] emission line (e.g. Kauffmann & Heckman 2009a; Wild et al. 2010; Tanaka 2012). At the redshifts and depth of the MOSDEF survey only a fraction of our AGN can be accurately placed on the BPT diagram, due to contamination from sky lines and the lack

of spectroscopic wavelength coverage at higher redshifts. Therefore, the commonly-used methods for estimating the star formation contribution to $L_{[\mathrm{OIII}]}$ at low redshifts cannot be applied to our sample. Although $L_{[\mathrm{OIII}]}$ can be boosted by star formation activity, here we do not find a significant correlation between SFR and $L_{[\mathrm{OIII}]}$, which indicates that it is unlikely for the instantaneous star formation rate to be correlated with $L_{[\mathrm{OIII}]}$.

3.6 Summary

In this paper we use the data from the first two years of the MOSDEF survey to investigate AGN identification and their host galaxies properties at $1.37 < z < 3.80$, with the majority of our sample at $z \sim 2$. We identify 55 AGN using the X-ray imaging data from *Chandra*, mid-IR data from IRAC camera on *Spitzer*, and rest-frame optical spectra from MOSDEF survey. We investigate the selection biases from each identification method and explore the host galaxy properties of these AGN. We further consider the relation between star formation activity and AGN luminosity in our sample. Our main conclusions are as follows:

- We find that AGN identified at any wavelength are biased against low mass host galaxies; this is an observational selection bias. IR AGN identification has an additional bias against the most massive galaxies. Quantifying the SFR relative to the main sequence and comparing the distributions for IR and optical AGN, we find that IR AGN are primarily identified in galaxies with relatively higher SFRs, while optical AGN are identified in galaxies with relatively lower SFRs (p=0.004, at $> 2\sigma$ significance). X-ray selection does not display any bias in the SFR distribution relative to the main sequence. The observational biases in stellar mass can result in biases in terms of the dust content of host galaxies, with IR AGN showing a possible bias towards less dusty host galaxies and optical and X-ray

AGN showing a possible bias towards more dusty host galaxies in our sample.

- Within the star-forming galaxy population, once stellar mass selection biases are taken into account, we find that AGN reside in galaxies with similar physical properties (SFR, dust content, and stellar age) as inactive galaxies. Therefore we find no evidence of AGN activity in particular types of galaxies, which is consistent with stochastic fueling of AGN in any kind of galaxy, and no strong evidence for AGN feedback.

- The majority of the AGN in our sample can be identified using optical diagnostics. We find that 75% of the X-ray AGN in our sample are also identified with optical diagnostics, indicating the reliability of optical AGN selection. However, optical identification is limited by the quality of the spectroscopic data, as optical emission lines in most of the non-optical AGN in our sample at $z \sim 2$ are contaminated by night sky lines.

- Almost half of the IR AGN in our sample are recovered at X-ray or optical wavelengths. IR imaging provides a more uniform depth than X-ray data and is not affected by the quality of optical spectroscopy; thus IR AGN identification can improve the completeness of AGN samples at $z \sim 2$.

- The relationship between $L_{\rm X}$ and $L_{\rm [OIII]}$ in our sample at $z \sim 2$ is consistent with the relation of Heckman et al. (2005) in the local Universe. Unlike Heckman et al. (2005), who found that the majority of local optical AGN can be recovered at X-ray wavelengths, we find X-ray counterparts for only 50% of the optical AGN in our sample. This is likely due to the relatively shallower and variable depth of the X-ray data across our fields.

- We do not find a significant correlation between SFR/SFR$_{\rm MS}$ (SFR relative to the

main sequence of star formation) and AGN luminosity (using L_X or $L_{[OIII]}$) in our sample. Although $L_{[OIII]}$ can be boosted by star formation activity in the host galaxy, at $z \sim 2$ we cannot apply correction techniques commonly used at lower redshifts to estimate the SF contamination.

Although the selection biases in our sample are derived from a small number of AGN, they are consistent with results of studies at intermediate redshifts with larger samples. The presence of these selection biases indicates that in order to obtain a more complete AGN census, complementary identification techniques at multiple wavelengths are required. To robustly study AGN host galaxy properties, the selection biases from each identification technique should be taken into account.

3.7 Acknowledgements

We thank the MOSFIRE instrument team for building this powerful instrument, and for taking data for us during their commissioning runs. This work would not have been possible without the 3D-HST collaboration, who provided us the spectroscopic and photometric catalogs used to select our targets and to derive stellar population parameters. Based on observations made with the NASA/ESA Hubble Space Telescope, which is operated by the Association of Universities for Research in Astronomy, Inc., under NASA contract NAS 5-26555. These observations are associated with programs 12177, 12328, 12060-12064, 12440- 12445, 13056. Funding for the MOSDEF survey is provided by NSF AAG grants AST-1312780, 1312547, 1312764, and 1313171 and grant AR-13907 from the Space Telescope Science Institute. A.L.C. acknowledges support from NSF CAREER award AST-1055081. N.A.R. is supported by an Alfred P. Sloan Research Fellowship. JA acknowledges support from ERC Advanced Grant FEEDBACK 340442. The data presented herein were obtained at the W. M. Keck Observatory, which is operated

as a scientific partnership among the California Institute of Technology, the University of California and the National Aeronautics and Space Administration. The Observatory was made possible by the generous financial support of the W. M. Keck Foundation. The authors wish to recognize and acknowledge the very significant cultural role and reverence that the summit of Mauna Kea has always had within the indigenous Hawaiian community. We are most fortunate to have the opportunity to conduct observations from this mountain.

Chapter 3, in full, is a reprint of the material as it appears in The Astrophysical Journal 2017. Azadi, M., Coil, A., Aird, J., Reddy, N., Shapley, A., Freeman, W., Kriek, M., Leung, GCK., Mobasher, B., Price, S., Sanders, R., Shivaei, I., Siana, B. 2017. The dissertation author was the primary investigator and author of this paper.

Chapter 4

The MOSDEF Survey: The Nature of Mid Infrared Excess Galaxies

4.1 Abstract

We present analysis from the MOSFIRE Deep Evolution Field (MOSDEF) survey on the nature of so-called "MIR-excess" galaxies which are galaxies with SFR inferred from MIR data substantially elevated relative to that estimated from UV data, after correcting for dust. We use a sample of ∼200 galaxies and AGN with significant 24 μmdetections from MIPS on *Spitzer* at $z < 2.61$. While we identify $\sim 20\%$ of our galaxies as mid-IR excess , we find that identification of mid-IR excess galaxies is strongly reliant on the SFR estimating and dust reddening corrections. We indicate that commonly-used extrapolations of the total SFR from the observed 24 μmband, using luminosity-dependent templates based on local galaxies, overestimate the total IR luminosity and SFR in $z \sim 2$ galaxies. By including *Herschel* FIR observations, with a stellar mass-dependent, luminosity-independent template we obtain a more reliable estimate of the SFR, consistent with other star formation tracers. We also indicate that the method used for reddening correction of UV driven SFR plays an important role in a robust estimation of SFR and identification of mid-IR excess galaxies. Using the X-ray, IR and BPT selected AGN data from the MOSDEF survey, we do not find a

higher prevalence for AGN in MIR-excess galaxies relative to MIR-normal galaxies. Also stacking analysis of X-ray undetected galaxies does not reveal a harder spectrum in MIR-excess sources relative to MIR-normal galaxies. However, we find that variation of depth of X-ray data from field to field is important in the stacking analysis. Overall, our analysis does not indicate that AGN activity contributes to the MIR-excess, which implies that this phenomena may be primarily due to emission from PAH dust molecules.

4.2 Introduction

By the advent of infrared (IR) satellites such as the Infrared Astronomical Satellite (IRAS; Neugebauer et al. 1984), the Infrared Space Observatory (ISO; Kessler et al. 1996) and later *Spitzer* (Werner et al. 2004), the *Wide-field Infrared Survey Explorer* (WISE; Wright et al. 2010) and *Herschel* (Pilbratt et al. 2010), remarkable progress has been made in our understanding of the stellar content and star formation of galaxies. Mid-IR (MIR) imaging instruments such as the Multi-band Imaging Photometer on *Spitzer*(MIPS; Rieke et al. 2004) allow us to detect emission from various phenomena contributing at mid-IR wavelengths in galaxies. In particular, studies indicate that MIPS 24 μmdata can be used to estimate the total star formation rate (SFR) of galaxies, as it correlates well with other star formation tracers such as Hα (e.g. Calzetti et al. 2005; Daddi et al. 2007c; Kennicutt et al. 2009).

Using MIPS observations, several studies have found that there are galaxies for which the observed 24 μmflux is substantially elevated relative to what is expected from multi-wavelength data (e.g. Daddi et al. 2007c; Papovich et al. 2007), which has resulted in the identification of so called "mid-IR excess " galaxies. Specifically, Daddi et al. (2007c) report the discovery of a large population ($\sim$25%) of $z \sim 2$ BzK-selected galaxies with a mid-IR excess such that their combined IR and UV SFR exceed the extinction-corrected UV SFR by a factor of three. However, the fraction of mid-IR

excess galaxies identified by Daddi et al. (2007a) may be reliant on the accuracy of both the IR and UV star formation estimates, and there are known uncertainties on each that need to be treated carefully.

Several studies propose empirically- (or semi-empirically-) derived templates based on local star-forming galaxies to estimate the SFR from 24 μmband data (e.g. Chary & Elbaz 2001; Dale & Helou 2002; Rieke et al. 2009). It has been shown that the identification of mid-IR excess galaxies depends on the method used for estimating the total IR luminosity, L_{IR} . While Daddi et al. (2007c) use templates from Chary & Elbaz (2001), Salim et al. (2009) use Dale & Helou (2002) templates to find a much lower fraction of mid-IR excess galaxies than Daddi et al. (2007c,a). After the launch of *Herschel*, which enabled the detection of high redshift galaxies directly at far-IR (FIR) wavelengths, studies found that the luminosity-dependent templates created based on local galaxies systematically overestimate L_{IR} in galaxies with $L_{IR} > 10^{12}\ L_{\odot}$ at $z > 1.5$ (e.g. Nordon et al. 2010; Muzzin et al. 2010; Elbaz et al. 2011). This is due to high redshift luminous galaxies having a lower dust temperature than their local counterparts (e.g. Symeonidis et al. 2011b). To resolve the problem of overestimating L_{IR} , more recent studies propose a single luminosity-independent conversion for L_{IR} estimation from MIR observations (Wuyts et al. 2008, 2011; Elbaz et al. 2011; Nordon et al. 2012). Furthermore, several studies indicate that stellar mass, metallicity, or specific star formation rate (sSFR) can also impact the L_{IR} estimation from 24 μmobservations (e.g. Smith et al. 2007; Nordon et al. 2012; Shivaei et al. 2017).

The identification of mid-IR excess galaxies identification also depends on the extinction-corrected UV SFR. $\mathrm{SFR_{UV}}$ can be corrected for dust absorption using various methods, ranging from using measurements of the UV photometry slope to using an average correction based on different attenuation curves (Cardelli et al. 1989; Calzetti et al. 2000; Reddy et al. 2015). It has recently become possible using NIR spectroscopic

data to directly measure the ratio of Balmer emission lines Hα /Hβ , or the Balmer decrement, in statistical samples of individual galaxies at $z \sim 2$. The Balmer decrement is an indicator of reddening of the ionized gas, which can be used to estimate the stellar continuum reddening as well (Reddy et al. 2015). However, in dusty galaxies reddening corrections are very uncertain (e.g. Goldader et al. 2002), and L_{IR}/L_{UV} varies with stellar mass, dust temperature, and evolution of the dust temperature with redshift (e.g. Bouwens et al. 2016). Therefore, underestimating the reddening correction can lead to the identification of mid-IR excess galaxies that may not be real.

Some studies have suggested that the elevated MIR flux in mid-IR excess galaxies is due to a contribution from active galactic nuclei (AGN) that are not directly detected at X-ray wavelengths (e.g. Daddi et al. 2007a; Alexander et al. 2011; Rangel et al. 2013). Daddi et al. (2007a) find that the spectral energy distribution (SED) of the mid-IR excess galaxies peaks at redder wavelengths than the rest-frame 1.6 μmstellar peak. They also find a redder K-5.8 μmcolor in mid-IR excess galaxies than in normal galaxies, which they conclude is due to an underlying AGN contribution. By performing an X-ray stacking analysis on MIR-excess galaxies without an X-ray detection, Daddi et al. (2007a) find a much harder X-ray spectrum in mid-IR excess galaxies than in normal galaxies, which suggests the presence of Compton-thick AGN (see also Fiore et al. 2008).

The depth and sensitivity of the X-ray data plays an important role in AGN identification (Mendez et al. 2013; Azadi et al. 2017). More recently, Rangel et al. (2013) used deeper *Chandra* observations of BzK-selected galaxies in the *Chandra* Deep Field North (CDFN) and *Chandra* Deep Field South (CDFS) fields to find no significant evidence for elevated X-ray detection rate in mid-IR excess galaxies compared to normal galaxies. Stacking analysis in Rangel et al. (2013) show a softer signal than Daddi et al. (2007a) which they argue is due to a mixture of highly absorbed AGN, low-luminosity unobscured AGN and star-forming galaxies. They discuss that the hard spectrum in the

stacking analyses of earlier studies (e.g. Daddi et al. 2007a; Fiore et al. 2008) is due to a few hard X-ray sources that were just below the detection limit of that data used at the time, which are now directly detected with deeper X-ray data. Rangel et al. (2013) also find that while there are AGN among the mid-IR excess galaxies population, they are not typically Compton-thick AGN. They conclude that the bulk of the mid-IR excess galaxies population are luminous, dusty, star-forming galaxies where the SFRs are either overestimated in the mid-IR, underestimated in the UV, or both.

While these studies rely only on X-ray diagnostics to identify AGN, other methods and wavelengths can be used for AGN identification. In general, X-ray imaging is a reliable method for identifying AGN (e.g. Azadi et al. 2017) and only fails when the hydrogen column density (N_H) in the dusty structure surrounding the supermassive black hole (SMBH) exceeds $\sim 10^{24}$ cm^{-2} (e.g. Comastri et al. 2011). The obscuring structure also blocks the UV and optical continuum from the central engine but reradiates the absorbed energy at MIR wavelengths. This MIR radiation from the AGN reveals itself as a power-law in the MIR SED, which is a feature that is also used to identify X-ray obscured and unobscured AGN (e.g. Lacy et al. 2004; Stern et al. 2005; Donley et al. 2012; Mendez et al. 2013). Additionally, optical diagnostics such as the "BPT diagram" ([N II]/Hα versus [O III]/Hβ , Baldwin et al. 1981) are also used to identify AGN at both $z \sim 0$ and $z \sim 2$ (e.g. Kauffmann et al. 2003a; Coil et al. 2015). Using multi-wavelength AGN identification techniques can therefore provide a clearer picture of the AGN contribution in mid-IR excess galaxies.

We note that the excess 24 μmemission in $z \sim 2$ galaxies reported in the above studies could be due to enhanced emission from polycyclic aromatic hydrocarbon (PAH) molecules rather than obscured AGN activity (e.g. Pope et al. 2008; Nordon et al. 2012). Emission from PAH molecules is significant at rest-frame wavelengths of 5–12 μm, but the strength of the emission varies with stellar mass and metallicity (e.g. Engelbracht

et al. 2006; Smith et al. 2007; Shivaei et al. 2017) and may contribute up to 20% of the L_{IR} (e.g. Smith et al. 2007). Therefore, investigations of mid-IR excess galaxies should take into account the possible enhancement at mid-IR wavelengths due to PAH features.

In this paper we study the nature of mid-IR excess galaxies at $z \sim 2$ in the MOSFIRE Deep Evolution Field (MOSDEF) survey (Kriek et al. 2015). The MOSDEF survey used the MOSFIRE multi-object NIR spectrograph (McLean et al. 2012) on the Keck I telescope to observe galaxies and AGN at $z \sim$1.37 – 3.80 over the course of four years; for this study we use the data from the first three years of the survey. Our aim is to resolve the outstanding question of whether the identification of mid-IR excess sources is due to an overestimation of the IR-based SFR, an underestimation of the UV-based SFR, and/or AGN contamination. In MOSDEF we benefit from a more complete galaxy selection at $z \sim 2$ than previous studies and do not limit our sample to BzK galaxies.

We investigate how the identification of mid-IR excess galaxies depends on the choice of templates used for estimating L_{IR} and the methods used for the reddening correction of $\mathrm{SFR_{UV}}$. In the MOSDEF sample we directly measure the Balmer decrement in individual galaxies (Reddy et al. 2015), such that in addition to testing average attenuation curves and the UV spectral slope, we can use Balmer decrements for the $\mathrm{SFR_{UV}}$ reddening correction. As discussed above, for identifying the contribution due to AGN previous studies had to rely only on X-ray stacking analyses. In this study we additionally use the rest-frame optical spectra obtained in the MOSDEF survey and the BPT diagram (e.g. Baldwin et al. 1981), as well as MIR identification of AGN, to investigate the contribution of AGN to the observed mid-IR excess .

The outline of the paper is as follows: in Section 4.3 we describe our dataset, the procedure used for measuring the optical emission lines, the 24 $\mu m$and FIR data, and the IR stacking analysis, and the method used for estimating stellar masses. In Section 4.4 we present our results on the nature of the obscured AGN at $z \sim 2$. In

this section we consider various methods for estimating L_{IR} and correcting $\mathrm{SFR_{UV}}$ for extinction correction, and perform X-ray stacking analysis. We discuss our results in 4.5 and conclude in Section 4.6. Throughout the paper we adopt a flat cosmology with Ω_Λ =0.7 and H_0=72 km $\mathrm{s^{-1}Mpc^{-1}}$.

4.3 Data

In this paper, we use the dataset from the first three years of the MOSDEF survey to study the nature of galaxies with mid-IR excess at $z \sim 2$. In this section, we describe our galaxy and AGN sample and the methods used for measuring the emission lines and stellar masses. We also describe the 24 $\mu m$and FIR data in our sample, as well as IR stacking analysis.

4.3.1 The MOSDEF Survey

In the MOSDEF survey (Kriek et al. 2015) we use spectroscopic data from the MOSFIRE spectrograph (McLean et al. 2012) on the 10 m Keck I telescope. MOSFIRE provides wavelength coverage from 0.97 to 2.40 μm with moderate resolution (R=3000-3650). The targets in the MOSDEF survey were selected from three redshift intervals ($1.37 < z < 1.70$, $2.09 < z < 2.61$ and $2.95 < z < 3.80$) to ensure coverage of the strong rest-frame optical emission lines ([O II] ,Hβ ,[O III] ,Hα) in the Y, J ,H and K bands. AGN identified in advance via X-ray imaging from *Chandra* or IR imaging from IRAC on *Spitzer* telescopes. AGN were given higher targeting weights as well as brighter sources with more secure prior redshift estimations.

In MOSDEF we obtain the spectra for sources in five extragalactic fields of AEGIS, COSMOS, GOODS-N, GOODS-S, and UDS in areas overlapping with CANDELS (Grogin et al. 2011; Koekemoer et al. 2011) and 3D-*Hubble Space Telescope* (*HST*) grism survey (Brammer et al. 2012)(for the full details of the survey see Kriek

et al. 2015). Our overall sample from three years of the MOSDEF survey includes ∼792 galaxies and AGN. We note that for the purpose of this paper we limit our sample to $z < 2.61$ to ensure that 24 μm observations from MIPS on *Spitzer* cover the rest-frame 8 μm.

4.3.2 Emission Line Measurements

In MOSEDF we measure the flux of the rest-frame optical emission lines and use them to estimate the Balmer decrement (Hα /Hβ), and to identify optical AGN using [O III]/Hβ vs [N II]/Hα BPT diagram. In this section we briefly describe the methods used by Reddy et al. (2015) and Azadi et al. (2017) for measuring the flux of the emission lines.

For MOSDEF galaxies the Hβ , [O III] , Hα , and [N II] emission line fluxes are estimated by fitting multiple Gaussian functions described in Reddy et al. (2015). Reddy et al. (2015) allow a linear fit to the continuum, a single Gaussian component to Hβ and [O III] , and a triple Gaussian function to [N II] λ6550 , Hα and [N II] λ6585 . The spectra of each galaxy were perturbed 1000 times within the error spectra and the dispersion of the perturbed lines was taken as the flux error.

To identify optical AGN we use the procedure described in Azadi et al. (2017). Azadi et al. (2017) use `MPFIT` nonlinear least-square fitting function in IDL (Markwardt 2009). In this method the continuum is fixed to be flat and the same physical components are required to have the same FWHM and velocity offset determined from the line with the highest S/N. The spacing between the [O III] λ4960 and [O III] λ5008 (as well as the [N II] λ6550 and [N II] λ6585 lines) forbidden lines are fixed and their flux ratios are set to be 1:3. We fit [O III] λ5008 simultaneously with [O III] λ4960 , and Hα with [N II] λ6550 and [N II] λ6585 using 4 models. In model 1, all lines are fitted with a narrow component with FWHM <2000 km s^{-1}. In model 2, in addition to the narrow

components we allow for an underlying broad component for the Hβ and Hα lines with FWHM >2000 km s^{-1}. In model 3, we fit each line with a narrow component and an additional component with FWHM <2000 km s^{-1} but with a velocity offset relative to the narrow component representing the outflow components. In model 4, all the narrow, outflow and broad Hβ and Hα are considered. The first model with narrow components is considered as the best fit for the sources unless the additional component improve the reduced χ^2 at 99% confidence level (Azadi et al. 2017). We note that the flux of Hβ and Hα lines (narrow components) are corrected for the underlying stellar absorption (for more details see Reddy et al. 2015).

4.3.3 AGN Sample

In MOSDEF we use three methods to identify AGN, X-ray imaging from *Chandra*, mid-IR imaging from *Spitzer* and the BPT diagram using the MOSDEF spectra; the details of MOSDEF AGN identification is described in Azadi et al. (2017).

The X-ray AGN were identified prior to MOSDEF targeting using *Chandra* observations with depth of 4 Ms in GOODS-S, 2 Ms in GOODS-N, 800 ks in EGS and 160 ks in COSMOS fields, corresponding to hard band flux ($f_{2-10\,\mathrm{keV}}$) limits of 1.6×10^{-16}, 2.8×10^{-16}, 5.0×10^{-16} and 1.8×10^{-15} respectively in each field. The X-ray catalogs were generated according to the method described by Laird et al. (2009), Nandra et al. (2015) and Aird et al. (2015). To identify the optical, NIR and *Spitzer* IRAC counterparts of the X-ray sources we use the likelihood ratio technique (e.g. Brusa et al. 2007b; Laird et al. 2009; Aird et al. 2015) where the source with the highest likelihood ratio is selected as the best match for sources with multiple counterparts. Eventually we match the X-ray counterparts to the 3D-*HST* catalogs used for targeting in MOSDEF. We estimate the rest-frame 2–10 keV X-ray luminosities based on the hard (2–7 keV) or the soft (0.5-2 keV) band flux (when there is no detection for the hard band) assuming a

simple power-law spectrum with Galactic absorption and photon index of $\Gamma = 1.9$.

Although X-ray imaging is reliable for AGN identification, it may fail in identifying highly obscured and Compton thick AGN. IR imaging can recover some of these heavily obscured AGN as UV and optical photons from the central engine are absorbed by dust grains in the obscuring structure and re-emitted at longer wavelengths. Several mid-IR AGN selection techniques have been proposed using IRAC (Fazio et al. 2004) on the *Spitzer* space telescope or WISE survey (e.g. Lacy et al. 2004; Stern et al. 2005; Donley et al. 2012; Mateos et al. 2012). Each of these selection methods may suffer from contamination from star-forming galaxies misclassified as AGN. However, Mendez et al. (2013) show that at intermediate redshifts Donley et al. (2012) is a reliable method for identifying mid-IR AGN. In MOSDEF we use Donley et al. (2012) criteria with some modifications; Donley et al. (2012) criteria is as follow:

$$x = \log_{10}\left(\frac{f_{5.8\mu\mathrm{m}}}{f_{3.6\mu\mathrm{m}}}\right), \quad y = \log_{10}\left(\frac{f_{8.0\mu\mathrm{m}}}{f_{4.5\mu\mathrm{m}}}\right) \tag{4.1}$$

$$x \geq 0.08 \text{ and } y \geq 0.15 \text{ and} \tag{4.2}$$

$$y \geq (1.21 \times x) - 0.27 \text{ and} \tag{4.3}$$

$$y \leq (1.21 \times x) + 0.27 \text{ and} \tag{4.4}$$

$$f_{4.5\mu\mathrm{m}} > f_{3.6\mu\mathrm{m}} \text{ and} \tag{4.5}$$

$$f_{5.8\mu\mathrm{m}} > f_{4.5\mu\mathrm{m}} \text{ and} \tag{4.6}$$

$$f_{8.0\mu\mathrm{m}} > f_{5.8\mu\mathrm{m}} \tag{4.7}$$

We require detection in all IRAC bands with S/N limits of 3, 3, 2.4, and 2.1

respectively in channels 1 to 4 (Mendez et al. 2013). Our slight modification includes relaxing equation 4.4 and allowing within the 1σ errors on the IRAC photometry in equations 4.5, 4.6 or 4.7. Donley et al. (2012) criteria is very pure and restricted, and these modification are made to include a few sources which satisfy all the above conditions except for one (for more details see Azadi et al. 2017).

We use the BPT digram to identify optical AGN; to measure the [N II]/Hα and [O III]/Hβ line ratios we use the line fitting procedure described in 4.3.2 and exclude any sources that require a significant broad component for either Hβ or Hα lines. As shown in Coil et al. (2015) and Azadi et al. (2017) we consider sources above the Meléndez et al. (2014) line as optical AGN in our sample.

As we mention below, in this paper we restrict our analysis to sources with significant 24 μmdetection at redshifts < 2.61. Therefore from 792 galaxy and AGN, we limit our sample to 146 galaxy and 52 X-ray, IR or optical AGN.

4.3.4 Stellar Mass Measurement

We estimate stellar mass of the galaxies in MOSDEF using the spectral energy distribution (SED) fitting with the multi-wavelength photometry from 3D-*HST* (Skelton et al. 2014) and our spectroscopic redshift measurements. We use the FAST stellar population fitting code (Kriek et al. 2009), with Chabrier (2003) stellar initial mass function (IMF), Conroy et al. (2009) Flexible Stellar Population Synthesis (FSPS) models, the Calzetti et al. (2000) dust reddening curve, and a fixed solar metallicity in a delayed exponentially declining star formation histories.

4.3.5 24 μm Flux Density and L_8 Measurements

In this study we restrict our analysis to galaxies with significant *Spitzer*/MIPS24 μmdetection which restrict our sample to 199 galaxies and AGN. We use the 24 μmdata

from the Far-Infrared Deep Extragalactic Legacy Survey (Dickinson & FIDEL Team 2007). We adopt the method described in Reddy et al. (2010) and Shivaei et al. (2017) for estimating the 24 μmflux densities. In this method, a higher resolution data from IRAC is used to determine the location of each object. Around each target a sub-image is constructed and a point spread function (PSF) is fitted simultaneously to all sources including the target and a covariance matrix is used to determine the robustness of each fit. The background flux is estimated by fitting PSF to random positions at least 1 FWHM away from the target, and the standard deviation of those fluxes is taken as noise (see Reddy et al. 2010; Shivaei et al. 2017).

As noted above in this study we limit our sample to galaxies with $z < 2.61$ to ensure that their 24 μm flux densities cover the rest-frame 8 μmluminosity. To estimate the rest-frame 8 μmluminosity ($L_8 = \nu L_\nu[8\mu m]$) we calculate the K-correction using the templates developed by Chary & Elbaz (2001). Since Chary & Elbaz (2001) templates are based on local galaxies we first shift them according to the redshift of each galaxy and then convolve them with the MIPS 24 μmresponse curve. We identify the best template for each galaxy using the χ^2 minimization method (Shivaei et al. 2017).

4.3.6 *Herschel*/PACS Data and IR Stacking Analysis

As we discuss in Section 4.4 including FIR bands plays an important role in estimating the bolometric IR luminosity and hence identification of mid-IR excess galaxies. In parts of our analysis we include the *Herschel*/PACS 100 and 160 μmdata available in AEGIS, COSMOS (Elbaz et al. 2011) and GOODS (Magnelli et al. 2013) fields. The number of MOSDEF galaxies with PACS 100 and 160 μmrobust detection is respectively 50 and 47 (30 with both). To measure 100 $\mu m$and 160 μmflux densities we use the prescription described above for 24 μm, but instead of using IRAC data as priors we consider sources with significant MIPS 24 μmdetection.

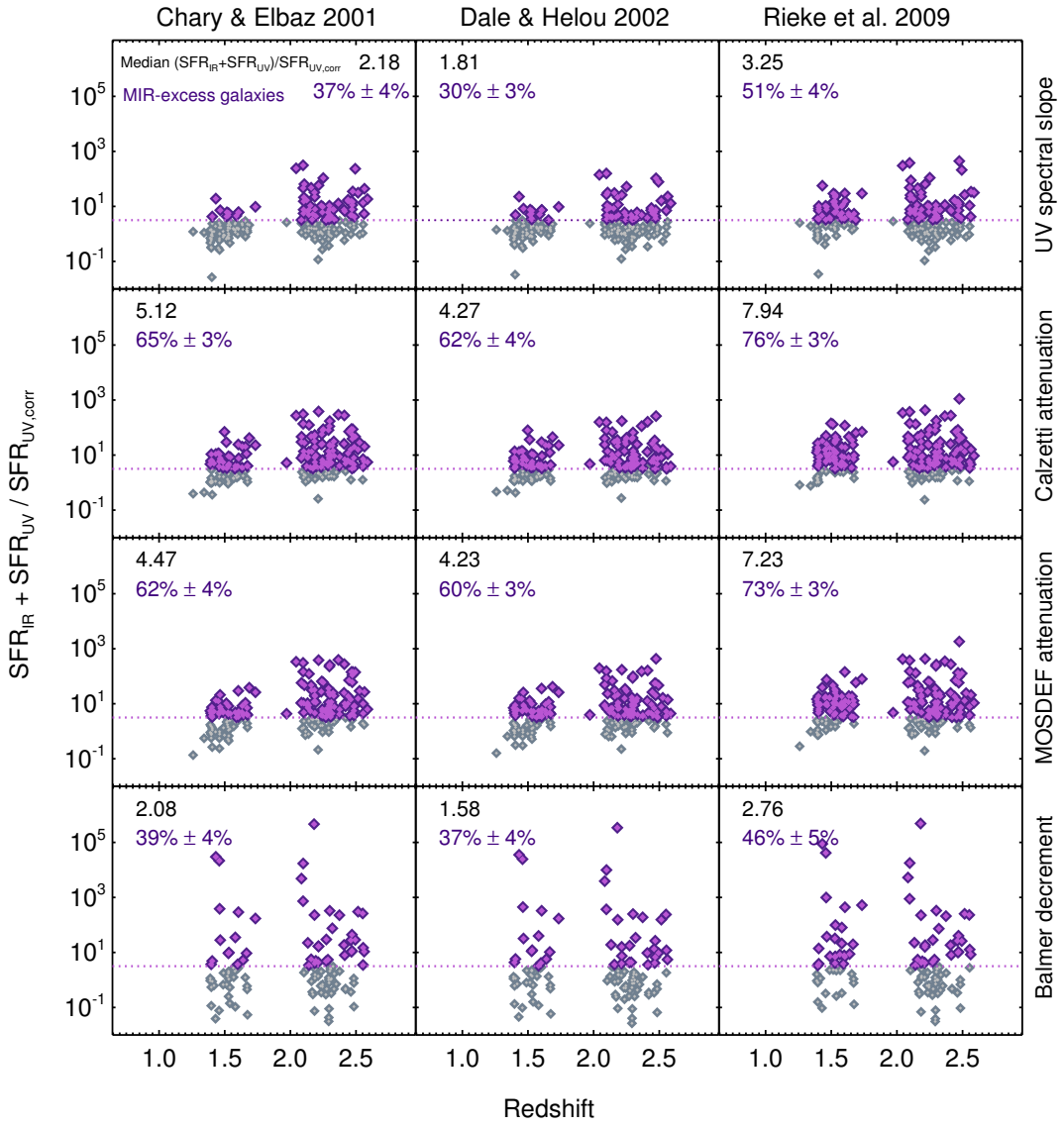

Figure 4.1. SFR/SFR$_{\rm MS}$ versus redshift for galaxies with significant 24 μmflux densities. The bolometric IR luminosity is estimated by extrapolation from 24 μmband using the luminosity dependent templates of Chary & Elbaz (2001), Dale & Helou (2002) and Rieke et al. (2009) in each column. Each row is corresponding to a different method for extinction correction of SFR$_{\rm UV}$; the methods are, UV spectral slope measured by fitting a power-law to the SED fits at 1200-2600Å , extinction estimated from Calzetti et al. (2000) attenuation curve and MOSDEF attenuation curve, and extinction measured from the Balmer decrement (Hα /Hβ), respectively in row one to four. The number of sources in the last row is different since our analysis is limited to the galaxies with significant Hβ and Hα detection. The percentage of 24 μmgalaxies that are mid-IR excess as well as the median SFR/SFR$_{\rm MS}$ are shown in each panel. The fraction of mid-IR excess galaxies strongly relies on L_{IR} and extinction correction.

The majority of the MOSDEF galaxies do not have a robust detection at 24 μmor FIR wavelengths. Therefore, we stack the MIPS and Herschel images for sources with S/N < 3 using the prescription described in Shivaei et al. (2017). The L_{IR} in stacked images is measured by using Chary & Elbaz (2001) templates where the best fit is determined as the one returning the minimum χ^2 to the PACS stacks.

4.4 Analysis and Results

4.4.1 Definition of MIR-Excess Galaxies

Studying a sample of BzK galaxies at $z \sim 2$, Daddi et al. (2007c) report the existence of a population of a so-called "MIR-excess" galaxies for which the total IR luminosity estimated from MIPS 24 μmflux densities shows an excess relative to that expected from other SFR tracers. They identify mid-IR excess sources as galaxies satisfying this criterion:

$$\log\left(\frac{\mathrm{SFR_{IR}} + \mathrm{SFR_{UV}}}{\mathrm{SFR_{UV,corr}}}\right) > 0.5 \tag{4.8}$$

where $\mathrm{SFR_{IR}}$ is the SFR estimated from MIPS 24 μmflux densities, $\mathrm{SFR_{UV}}$ is the star formation estimated from the UV data, and $\mathrm{SFR_{UV,corr}}$ is the UV star formation corrected for dust extinction. The empirical threshold of 0.5 dex is chosen by Daddi et al. (2007c) assuming that the intrinsic scatter in the ratio is to first order symmetrical, therefore a population of galaxies with excess in UV star formation rates exist as well. Daddi et al. (2007c) use Chary & Elbaz (2001) templates to convert 24 μmflux into L_{IR} , and correct $\mathrm{SFR_{UV}}$ for dust attenuation using Calzetti et al. (2000) attenuation law. Daddi et al. (2007c) find that $\sim 25\%$ galaxies at $z \sim 2$ show such an excess at MIR wavelength (after removing the X-ray detected AGN from their sample), and emphasize

that existence of this population is independent of the templates used for estimating the bolometric IR luminosity.

As noted above, in this paper we aim to investigate how the choice of templates for estimating L_{IR} and correction methods for estimating $SFR_{UV,corr}$ effect identification of mid-IR excess galaxies. Below we use the templates introduced by various studies to estimate L_{IR} , and consider various methods for correcting SFR_{UV} for dust extinction, and identify mid-IR excess galaxies in MOSDEF.

4.4.2 MIR-Excess Galaxies in MOSDEF

L_{IR} Estimated from Luminosity Dependent Templates

Figure 4.1 illustrates SFR/SFR_{MS} as a function of redshift. We use the luminosity dependent templates of Chary & Elbaz (2001), Dale & Helou (2002) and Rieke et al. (2009) to estimate L_{IR} in each column. We correct SFR_{UV} for extinction with various methods in each row, in the first row we use the UV spectral slope estimated from the SED fitting, in the second row we use the color excess calculated with Calzetti et al. (2000) attenuation curve, and use the MOSDEF attenuation curve in the third row, and use the Balmer decrement in the last row.

Below we first describe each of these templates used for L_{IR} estimation and then clarify the correction method used for estimating $SFR_{UV,corr}$. We illustrate the median SFR/SFR_{MS} and the percentage of galaxies with mid-IR excess in each panel where the errors on fractions are estimated from bootstrap resampling. We note that all of the MOSDEF AGN are included in this figure.

In the three luminosity dependent templates used in Figure 4.1 L_{IR} is estimated from extrapolation from a single band (24 μm). Chary & Elbaz (2001) consider the data from *ISO*, *IRAS* and *SCUBA* for local galaxies, and from the correlation between the luminosities at each wavelength construct 105 luminosity dependent between 0.1-1000

μm. These templates cover the L_{IR} between between $10^8 - 10^{13}$ $L_\odot$ for normal galaxies to ULIRGS. In practice, Chary & Elbaz (2001) estimate L_{IR} using only MIPS 24 μmband. They convolve MIPS 24 μmresponse curve with their SED models, and from a linear interpolation find the best template corresponding to the observed 24 μmflux density. Chary & Elbaz (2001) use the best template to convolve 12, 25, 60 and 100 μmresponse curves with, and use Sanders & Mirabel (1996) relation (Equation 4.9) for calculating the bolometric IR luminosity. However, in this paper we use the method described in section 4.3.5 to find the best template, and consider the luminosity corresponding to that template from Chary & Elbaz (2001) as the total IR luminosity.

$$L_{IR} = L(8-1000\ \mu m) = 1.8\times10^{-14}\times10^{26}\times (13.48L_{12}+5.16L_{25}+2.58L_{60}+L_{100}) \tag{4.9}$$

Dale & Helou (2002) semi-empirical templates are built on data from *ISO*, *IRAS* and *SCUBA* for 69 local galaxies with $L_{IR} < 10^{11}$ $L_\odot$.

Dale & Helou (2002) develop a theoretical model with three components for the emission from small and large dust grains, and the PAH molecules (see also Dale et al. 2001). In their model each dust grain's mass has a power-law distribution as a function of intensity:

$$dM(U) \propto U^{-\alpha}dU \qquad 0.3 < U < 10^5 \tag{4.10}$$

where M(U) is the dust mass heated by field at intensity U, and α, varies between 1–2.5 respectively from star-forming to quiescent galaxies. Dale & Helou (2002) construct 64 templates based on the variation of α. To estimate L_{IR} they consider the template producing the observed $f_\nu(60)/f_\nu(100)$ color as the best template, and by integrating from that template calculate L_{IR} .

In Figure 4.1 we use Dale & Helou (2002) templates with 24 μmband data assuming the empirical calibration of Marcillac et al. (2006) (Equation 4.11) as the scaling relation (see Marcillac et al. 2006; Papovich et al. 2007; Reddy et al. 2012). We find the best template by χ^2 minimization and use Sanders & Mirabel (1996) relation to estimate the total IR luminosity (Reddy et al. 2012).

$$\log(\frac{f_\nu(60)}{f_\nu(100)}) = 0.128 \times \log(L_{IR}) - 1.611 \tag{4.11}$$

To convert the L_{IR} to $\mathrm{SFR_{IR}}$ in the first two columns of Figure 4.1 we use Kennicutt (1998) relation assuming Salpeter (1955) IMF. In the last column we implement Rieke et al. (2009) relation between SFR and 24 μmluminosity to estimate $\mathrm{SFR_{IR}}$ directly from 24 μmflux densities (see Equation 4.12).

To derive this relation, Rieke et al. (2009) consider a sample of 11 local LIRGS and ULIRGS with *Spitzer*/IRS spectra and additional photometric data from optical to radio wavelengths. Rieke et al. (2009) calculate the IR luminosity for each of their galaxies using Sanders et al. (2003) calibration (similar to Sanders & Mirabel 1996), and combine the SED of the galaxies with luminosities close to each other to build a set of average templates. To optimize the weights of the average templates, they use synthetic colors of 25/8 μm, 25/12 $\mu m$and 60/25 μmsimultaneously from their observed data as a constraint. Their final average SEDs include 14 templates with L_{IR} between $10^{9.75} - 10^{13}$ $\mathrm{L_\odot}$.

Here we use the redshift dependent relation provided by Rieke et al. (2009) to

estimate SFR_{IR} :

$$\log_{10}(SFR[M_{\odot}/yr]) = \mathrm{A(z)} + \mathrm{B(z)} \times (\log(4\pi D_L f_{24,obs}) - 53) \tag{4.12}$$

in which $4\pi D_L f_{24,obs}$ is in Jy cm^2.

To estimate SFR_{UV} in Figure 4.1, we fit SEDs to the 3D-*HST* photometry and measure the UV flux (at the rest-frame wavelength 1600 Å) from the best stellar population model (for more details see Reddy et al. 2015). We convert the estimated luminosity to SFR_{UV} using Kennicutt (1998) relation with Chabrier (2003) IMF. As noted above, the rows in Figure 4.1 are corresponding to different extinction correction method of SFR_{UV} . In the first row, we correct SFR_{UV} for the dust extinction using the UV spectral slope. We calculate the UV slope (β_{SED}) by fitting power-laws to the SED at the rest-frame wavelength 1260–2600 Å . We calculate UV extinction using Equation 4.13 below obtained in Reddy et al. (2015).

$$A_{UV} = 1.84\beta + 4.48 \tag{4.13}$$

Below in Section 4.5 we discuss how the UV spectral slope estimated by fitting a power-law to directly to the photometry at UV wavelengths result in a different correction factor, and therefore different fraction of mid-IR excess galaxies.

In the second row, we use Calzetti et al. (2000) attenuation curve and the visual extinction (A_V) estimated from from the SED fitting described in section 4.3.4, while in

the third row we use MOSDEF attenuation curve presented in Reddy et al. (2015):

$$\begin{aligned} k(\lambda) &= -5.726 + \frac{4.004}{\lambda} - \frac{0.525}{\lambda^2} + \frac{0.029}{\lambda^3} + 2.505 \\ & \qquad 0.15 < \lambda < 0.60\ \mu m \\ &= -2.672 - \frac{0.010}{\lambda} - \frac{1.532}{\lambda^2} - \frac{0.412}{\lambda^3} + 2.505 \\ & \qquad 0.60 < \lambda < 2.85\ \mu m \end{aligned} \tag{4.14}$$

In the last row instead of an average attenuation, we use the ratio of Balmer emission lines (Hα /Hβ) in individual galaxies as a tracer of reddening of *ionized gas*. In this row we limit our sample to galaxies with significant Hβ and Hα emission, therefore the number of sources in the last row is different than the other panels of Figure 4.1. To estimate E(B-V) for the ionized gas we use the relation from Reddy et al. (2015):

$$E(B-V)_{gas} = \frac{2.5}{k(H\beta) - k(H\alpha)} \log(\frac{H\alpha/H\beta}{2.86}) \tag{4.15}$$

where $k(H\beta)$ and $k(H\alpha)$ are calculated with MOSDEF attenuation curve. In general, it is shown that the visual extinction of nebular lines is greater than the reddening of UV-optical continuum since the ionizing radiation originates from regions close to the dusty molecular clouds (e.g. Calzetti et al. 1994, 2000). We use the relation between the nebular reddening and UV continuum reddening as a function of specific SFR (sSFR) driven in (Reddy et al. 2015, Equation 4.16 below) to estimate $\mathrm{SFR_{UV,corr}}$.

$$\begin{aligned} E(B-V)_{gas} - E(B-V)_{stars} = \\ -0.049 + 0.079 \times (\log(sSFR) + 10)) \end{aligned} \tag{4.16}$$

In the last row we find a larger scatter and a larger correction factor compared to the other rows which is due to the small Hβ flux measurements. The average Balmer decrement for sources in the last panel is 4.3. We note that AGN may contribute significantly to the Hα line and might be expected to have a higher Balmer decrement than the inactive galaxies. However, our investigation shows that the AGN in our sample have a very consistent Balmer decrement to the rest of galaxies, therefore are included in our analysis in this row.

Overall, Figure 4.1 indicate that percentage of 24 μmselected galaxies classified as mid-IR excess can change in a wide range of 30–76% depending on the templates used for L_{IR} measurements and $\mathrm{SFR_{UV}}$ reddening correction. The median $\mathrm{SFR/SFR_{MS}}$ reported in each panel shows that Dale & Helou (2002) method is more successful than the other templates since with this method there is more consistency between $SFR_{IR}+SFR_{UV}$ and $SFR_{UV,corr}$. Daddi et al. (2007a) by using Chary & Elbaz (2001) templates and Calzetti et al. (2000) attenuation curve find that $\sim 30\%$ of $z\sim 2$ galaxies are mid-IR excess , while we find a much higher fraction (65%) with the same prescription. Below in Section 4.5 we indicate how the depth of 24 μmdata could result in such a significant difference.

L_{IR} Estimated from Luminosity Independent Conversions

The luminosity dependent templates described above are built based on local galaxies and may not be applicable at higher redshifts. With the advent of *Herschel*, detection of individual $z\sim 2$ galaxies at FIR wavelengths became possible. Studies show that extrapolation from 24 μmcan result in overestimation of L_{IR} in luminous galaxies at $z\sim 2$ (e.g. Nordon et al. 2010; Elbaz et al. 2011), as these galaxies may have a cooler temperature than their local counterparts (e.g. Symeonidis et al. 2011b). While in the local Universe there is a positive correlation between the luminosity of galaxies and dust temperature, at $z\sim 2$ there is a large scatter in their relation which leads in a deviation

Table 4.1. The average bolometric correction factor L_{IR}/L_8 driven when stacks of *Herschel* data are included

$< L_{IR} > / < L_8 >$	Chary & Elbaz (2001)	Dale & Helou (2002)	Rieke et al. (2009)
$9.6 < \log(\frac{M_*}{M_\odot}) < 10.0$	13.9	12.5	15.6
$10.0 < \log(\frac{M_*}{M_\odot}) < 10.6$	5.21	4.63	5.21
$10.6 < \log(\frac{M_*}{M_\odot}) < 11.6$	6.25	4.81	4.31

from a unique SED shape (e.g. Elbaz et al. 2010; Symeonidis et al. 2011b; Wuyts et al. 2011). Elbaz et al. (2011) with the deep 100 to 500 μmFIR data from *Herschel* show that at $z > 1.5$ mid-IR excess occurs in *individual* galaxies with $L_{IR} > 10^{12}$L$_\odot$ and argue that while local LIRGS and ULIRGS can be in starburst mode, at $z \sim 2$ they are mainly on the main sequence and therefore can be treated as a scaled up versions of local main sequence galaxies (e.g. Elbaz et al. 2011; Nordon et al. 2012).

In Figure 4.2, we show two additional methods for estimating L_{IR} from Elbaz et al. (2011) and Wuyts et al. (2008) which are both luminosity independent. Elbaz et al. (2011) find that the bolometric correction factor at 8 μm(L$_{\rm IR}$/L_8) is universal at $z < 2.5$. They use the normalization from Chary & Elbaz (2001) templates, identify the best template as the one that fits best to *Herschel* data, and calculate L_{IR} by integrating from the best fit SED. To resolve the problem of overestimation of L_{IR} for $z \sim 2$ ULIRGS, Elbaz et al. (2011) among many recent studies propose a single luminosity independent conversion (see also Wuyts et al. 2008, 2011; Nordon et al. 2012). In the left panel of Figure 4.2 we use the universal ratio of L$_{\rm IR}$/L_8 = 4.9 from Elbaz et al. (2011).

In the right panel of Figure 4.2 we use Wuyts et al. (2008) conversion factors for

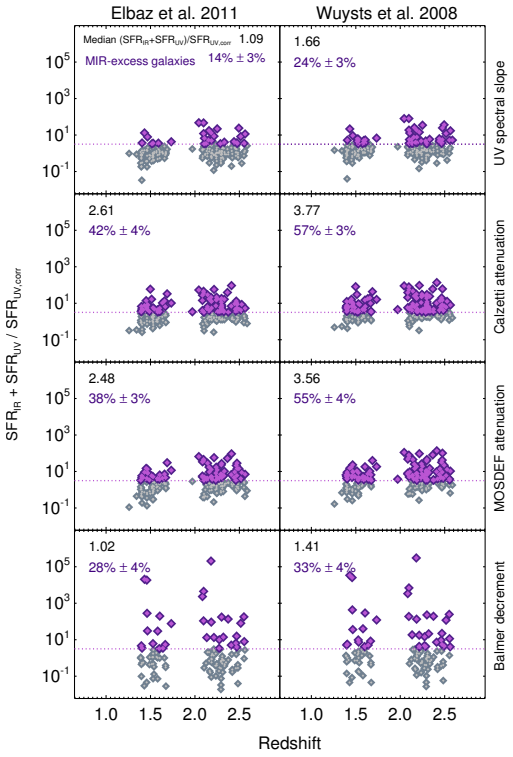

Figure 4.2. SFR/SFR$_{\rm MS}$ versus redshift for galaxies with significant 24 μmflux densities. In the left column, the bolometric IR luminosity is estimated from Elbaz et al. (2011) universal ratio of $L_{\rm IR}/L_8$ = 4.9 which was driven by including *Herschel* FIR data. In the right column, the luminosity independent, redshift dependent conversions of Wuyts et al. (2008) driven based on 24 μmdata is used for measuring L_{IR} . Each row is corresponding to a different method for extinction correction of SFR$_{\rm UV}$; the methods are, UV spectral slope measured by fitting a power-law to the SED fits at 1200-2600Å , extinction estimated from Calzetti et al. (2000) attenuation curve and MOSDEF attenuation curve, and extinction measured from the Balmer decrement (Hα /Hβ), respectively in row one to four. The number of sources in the last row is different since our analysis is limited to the galaxies with significant Hβ and Hα detection. The percentage of 24 μmgalaxies that are mid-IR excess as well as the median SFR/SFR$_{\rm MS}$ are reported in each panel. While the fraction of mid-IR excess galaxies strongly relies on L_{IR} and extinction correction, it is smaller in the left panel when FIR data are included for estimating L_{IR} .

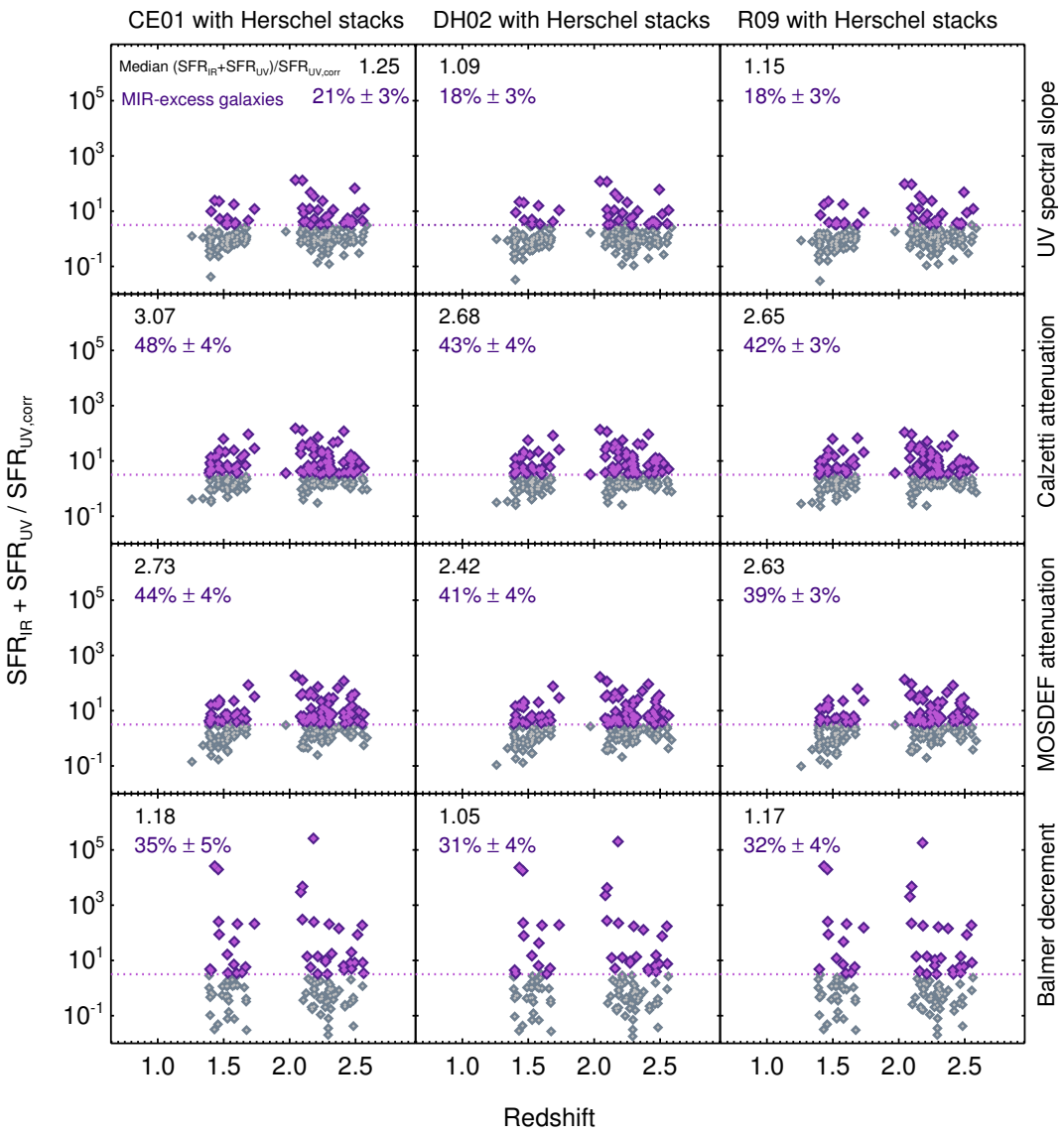

Figure 4.3. SFR/SFR$_{\rm MS}$ versus redshift for galaxies with significant 24 μmflux densities, using the three templates of Chary & Elbaz (2001),Dale & Helou (2002) and Rieke et al. (2009) while the best fits are determined from *Herschel*/PACS stacks. The L_{IR} is estimated using the luminosity independent, mass dependent conversions in Table 4.1.Each row is corresponding to a different method for extinction correction of SFR$_{\rm UV}$; the methods are, UV spectral slope measured by fitting a power-law to the SED fits at 1200-2600Å , extinction estimated from Calzetti et al. (2000) attenuation curve and MOSDEF attenuation curve, and extinction measured from the Balmer decrement (Hα /Hβ), respectively in row one to four. The number of sources in the last row is different since our analysis is limited to the galaxies with significant Hβ and Hα detection. The percentage of 24 μmgalaxies that are mid-IR excess as well as the median SFR/SFR$_{\rm MS}$ are reported in each panel. The fraction of mid-IR excess galaxies and the median SFR/SFR$_{\rm MS}$ drop significantly relative to the same panels in Figure 4.1.

MIPS 24 μmband at the redshift of each of our galaxies. Wuyts et al. (2008) use Dale & Helou (2002) models and find $L_{IR,\alpha}$ corresponding to different α values from those models (see Equation. 4.10); they take the average of $L_{IR,\alpha}$ as the best luminosity for each galaxies. We note that unlike Elbaz et al. (2011), Wuyts et al. (2008) conversions are not driven with FIR data. Wuyts et al. (2011) indicate that the conversion factors from Wuyts et al. (2008) result in IR luminosities that are median consistent (although with a large scatter) with *Herschel* L_{IR} measurements.

Comparing the fraction of mid-IR excess galaxies and the medianSFR/SFR_{MS} in the two columns of Figure 4.2 indicate that Wuyts et al. (2008) overestimate L_{IR} relative to Elbaz et al. (2011). Our investigation shows that at lower luminosities the L_{IR} estimated from these two methods are consistent, but at higher luminosities they deviate from the 1–1 line with Wuyts et al. (2008) L_{IR} dominating Elbaz et al. (2011) measurements which is probably due a lack of FIR data in Wuyts et al. (2008) analysis. A comparison between Figures 4.1 and 4.2 also confirms this point, as the left column of Figure 4.2 shows an improvement in SFR_{IR} estimation relative to Chary & Elbaz (2001) measurements with only MIR data, while Wuyts et al. (2008) method results to similar measurements to Dale & Helou (2002).

Overall, we find that when FIR data are included we obtain a more robust estimate of the bolometric IR luminosity, and a luminosity independent conversion factor such as Elbaz et al. (2011) universal ratio leads to a better agreement between between $SFR_{IR} + SFR_{UV}$ and $SFR_{UV,corr}$.

L_{IR} Estimated from Luminosity Independent Conversions and *Herschel* Stacks

In this section we repeat a similar analysis to Figure 4.1 but in addition to 24 μmband we include *Herschel* data to obtain a more reliable L_{IR} . However, most of the MOSDEF galaxies are not *Herschel*/PACS detected, so we include stacks of PACS 100

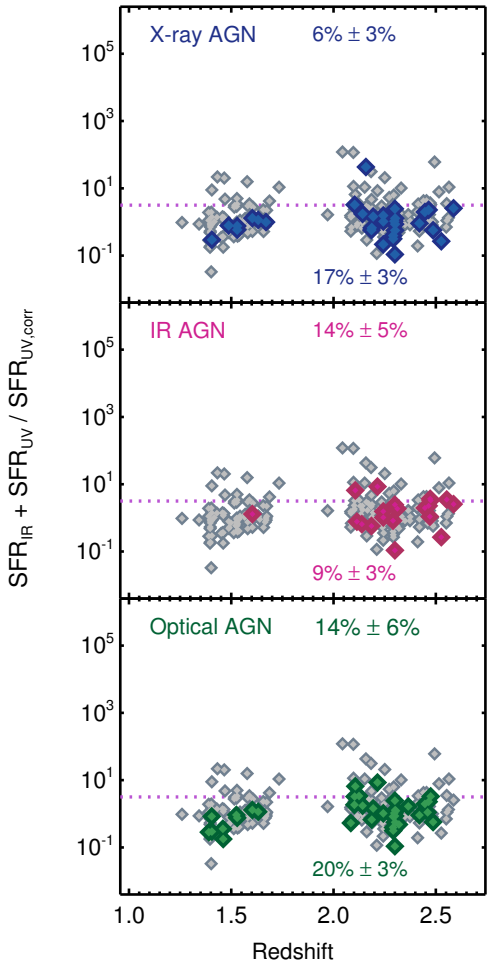

Figure 4.4. The fraction of X-ray, IR and optical AGN above and below the mid-IR excess threshold in SFR/SFR$_{MS}$ versus redshift space. SFR/SFR$_{MS}$ in all three panels is estimated with our most robust method (with the average L_{IR} /L_8 driven with 24 μmdata and stacks of PACS data in bins of stellar mass using Dale & Helou (2002) templates, and SFR$_{UV}$ corrected with UV spectral slope). The percentages of AGN above and below the mid-IR excess threshold do not reveal a preference for AGN in residing in mid-IR excess galaxies; this result stands for all the panels shown in Figure 4.3 with different templates and reddening corrections.

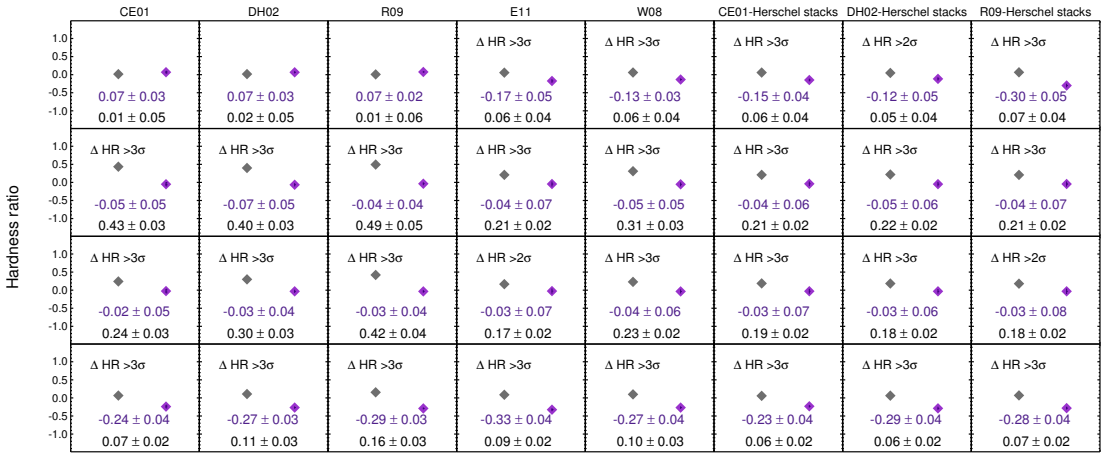

Figure 4.5. The hardness ratio of the mid-IR excess and MIR-normal galaxies after excluding the X-ray detected AGN in all 32 combinations of the templates and dust corrections considered in this work. When there is a significant difference at 2 or 3σ level in the hardness ratios, it is shown on the plot. We do not find a harder X-ray spectrum in mid-IR excess galaxies in either of these panels.

and 160 μmdata and find the best template in each method as the one that fits best to the PACS stacks. We perform this stacking analysis in bins of stellar mass since the ratio of L_{IR}/L_8 varies with stellar mass, metallicity or sSFR (e.g. Nordon et al. 2012; Shivaei et al. 2017). We present the the conversion factors in each bin of stellar mass in Table 4.1 (for more details on stacking analysis see Section 2.7 and Shivaei et al. 2017). and use these conversions to measure $\mathrm{SFR_{IR}}$ in Figure 4.3.

The median $\mathrm{SFR/SFR_{MS}}$ in Figure 4.3 indicate an improvement in SFR measurements with the luminosity independent, mass dependent conversions compared to Figure 4.1. The percentage of mid-IR excess galaxies drops significantly compared to their corresponding columns in Figure 4.1 (except for the last row where the scatter is large). Although our *Herschel* data is not as deep as Elbaz et al. (2011), we find similar $\mathrm{SFR/SFR_{MS}}$ and fractions of mid-IR excess galaxies in the left columns of Figures 4.2 and 4.3.

Overall, our analysis show that the luminosity independent conversion factors,

when FIR observations and stellar mass variations are taken into account, result in a robust estimate of L_{IR} and consequently a more reliable percentage for mid-IR excess galaxies. We find that Dale & Helou (2002) templates with extinction correction estimated from UV spectral slope provides the best agreement between $SFR_{IR} + SFR_{UV}$ and $SFR_{UV,corr}$.

4.4.3 AGN in MIR-Excess Galaxies

Several studies have proposed that mid-IR excess occurs in galaxies due to an underlying AGN contribution (e.g. Daddi et al. 2007a; Alexander et al. 2011; Rangel et al. 2013). Daddi et al. (2007c) after excluding the X-ray selected AGN find that $\sim 25\%$ of the $z \sim 2$ galaxies are mid-IR excess and argue that existence of this population reflects the presence of an underlying obscured AGN activity. In general, AGN could have a significant contribution to MIR emission that makes them distinguishable from star-forming galaxies (e.g Alonso-Herrero et al. 2006; Donley et al. 2012), but the question is could this contribution be the main reason for mid-IR excess phenomenon?

In MOSDEF we benefit from a sample of multi-wavelength identified AGN, and in particular from the optical (BPT) selection that can recover AGN that might be missed by X-ray or IR imaging techniques Azadi et al. (2017). In Figures 4.1, 4.2 and 4.3 we showed 32 different methods (eight templates and four dust correction methods) for mid-IR excess galaxies identification. As we noted above the method using Dale & Helou (2002) templates with *Herschel* stacks in bins of stellar mass and UV spectral slope from the SED fitting is the most robust method as it provides the best agreement between $SFR_{IR} + SFR_{UV}$ and $SFR_{UV,corr}$. We use this method in Figure 4.4 and show the fraction of sources that are X-ray, IR or optical AGN above and below the mid-IR excess threshold. With none of the three identification techniques AGN are more prevalent in mid-IR excess region.

While in Figure 4.4 we only illustrate one of the 32 methods of SFR estimation

discussed in this paper, we perform a similar analysis for all the other methods as well. With none of the methods shown in Figure 4.3, where L_{IR} is estimated more robustly, we find a higher fraction of AGN in among mid-IR excess galaxies (not even at 2σ level). But with some of the luminosity-dependent templates from local galaxies (shown in Figure 4.1) we do find a higher percentages of X-ray, IR or optical AGN at $2-3\sigma$ confidence level in mid-IR excess region. In particular, using a similar method as Daddi et al. (2007a) (CE01 template with Calzetti attenuation) we find a higher fraction of X-ray (3σ), IR(2σ) and optical AGN (2σ) in mid-IR excess region. However, the median $\mathrm{SFR/SFR_{MS}}$ of 5.12 with this method indicates that the higher incidence of AGN in mid-IR excess galaxies is due to the faulty estimation of SFR, and with a more reliable estimation in Figure 4.4 we do not find any evidence for a higher prevalence of AGN in mid-IR excess galaxies.

4.4.4 X-ray Stacking Analysis of MIR-Excess Galaxies

X-ray imaging is a reliable method for AGN selection (Mendez et al. 2013; Azadi et al. 2017, e.g.), however, it fails in identification of highly absorbed AGN with hydrogen column density of $N_H > 1.5 \times 10^{24}$ cm^{-2} (e.g. Della Ceca et al. 2008; Comastri et al. 2011). Studies predict that 10-50% of AGN are Compton thick (e.g. Akylas & Georgantopoulos 2009; Alexander et al. 2011; Lanzuisi et al. 2015) which is indeed a sizable fraction. The absorbed and reprocessed radiation from these AGN buried in dust may contribute to MIR radiation.

To examine whether the excess at MIR wavelengths in our galaxies occurs due to the obscured AGN activity, we exclude the X-ray detected AGN, and stack the X-ray photons in the remaining sample. In Figure 4.5 we illustrate the hardness ratio (H-S/H+S, where H and S are respectively the total count rates in the hard and soft X-ray bands) for the mid-IR excess and MIR-normal galaxies in all 32 combinations of templates and dust

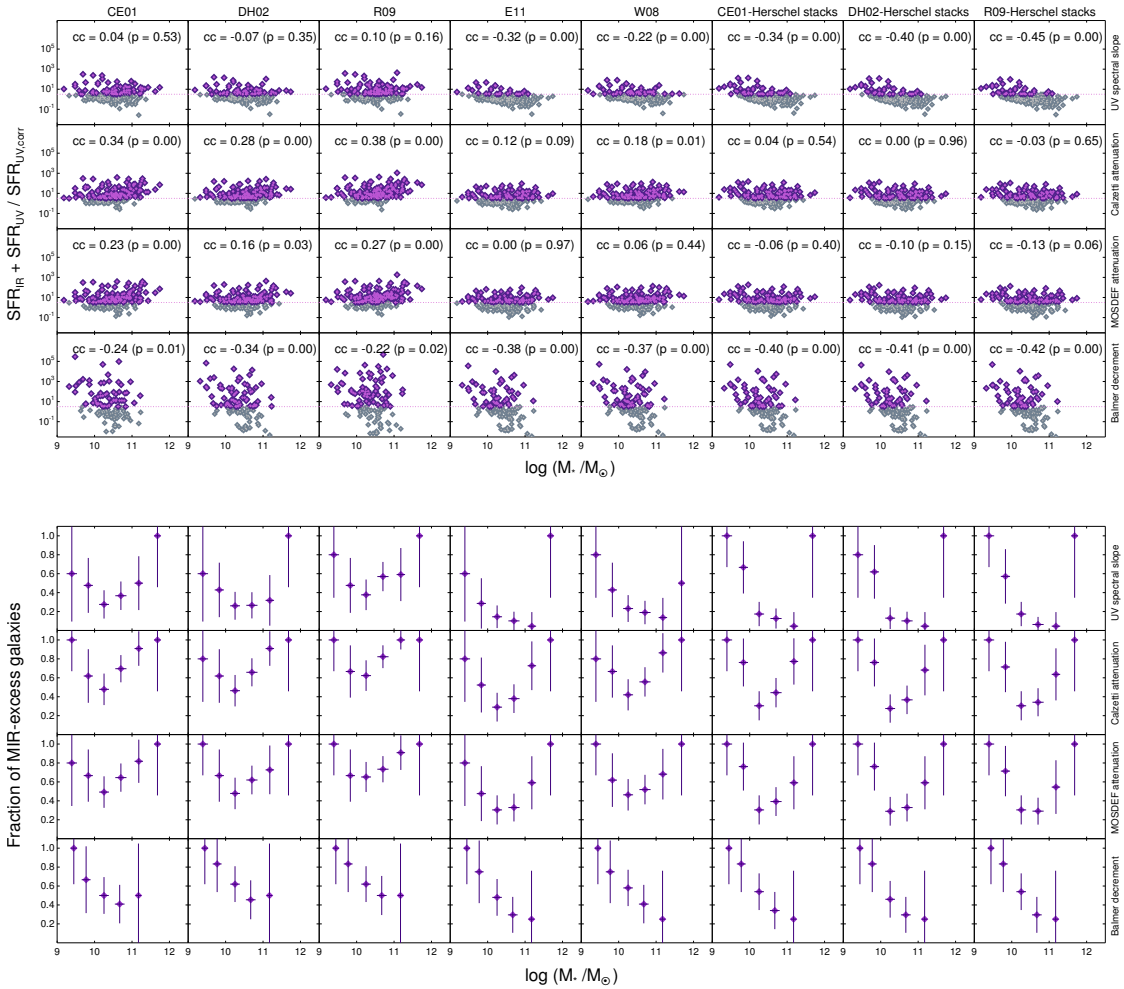

Figure 4.6. *Top:* SFR/SFR$_{\rm MS}$ versus stellar mass in all 32 combinations of the templates and dust corrections considered in this work. The number of sources in the last row is different since our analysis is limited to the galaxies with significant Hβ and Hα detection. The correlation coefficients and the significance levels are reported in each panel. *Bottom:* The fraction of mid-IR excess galaxies in bins of stellar mass. The stellar mass selection biases, inaccurate L_{IR} estimation and variation of reddening correction factor can justify the discrepancies between the trends in these panels.

corrections considered in this work. When there is a significant difference (at 2 or 3σ level) in the hardness ratios of the mid-IR excess and MIR-normal galaxies it is shown on the plot.

We find a relatively harder signal in MIR-normal galaxies than the mid-IR excess population. In none of these panels the hardness ratios for mid-IR excess galaxies propose an underlying hard spectrum, instead the negative hardness ratios in some panels indicate that the soft X-ray signals dominate in mid-IR excess galaxies in some cases. As we discuss later the soft X-ray signals could be due to variety of phenomena, from reflection-dominated radiation in obscured AGN to star-formation activity of the host galaxies.

Our best method (row1-column7) does not advocate for the dominance of the hard in either of the two populations, while in row 2-column 1 which is Daddi et al. (2007a) method we find a harder spectrum in MIR-normal galaxies that mid-IR excess ones, which is is at odds with Daddi et al. (2007a) finding. As we discuss below in Section 4.5, the hard spectrum of mid-IR excess galaxies in Daddi et al. (2007a) is probably due to a few undetected X-ray AGN, that in deeper X-ray surveys are detected(see also Alexander et al. 2011; Rangel et al. 2013).

We do not find a higher fraction of AGN above the mid-IR excess threshold. Also stacking analysis of our X-ray undetected sample does not show a harder spectrum in mid-IR excess galaxies than MIR-normal galaxies, which propose that AGN do not contribute to the MIR radiation in our sample.

4.4.5 MIR-Excess and Stellar Mass

In this section, we examine how the incidence of mid-IR excess varies with the stellar mass of the galaxies. In Figure 4.6 we plot SFR/SFR$_{\rm MS}$ versus stellar mass in all 32 combinations of the templates and dust corrections. The correlation coefficients (cc)

and their corresponding significance (p) are shown on the plot. We use the $r-correlate$ routine in IDL, which calculates the Spearman's rank correlation coefficient and the significance of its deviation from zero. In the bottom panels we plot fraction of mid-IR excess galaxies in intervals of $\Delta\log(\frac{M_*}{M_\odot})$ = 0.5 dex of stellar mass, where the stellar masses are inferred from the SED fitting. We calculate the errors assuming a binomial distribution using the Bayesian method of Cameron (2011).

The relation between SFR/SFR$_{\rm MS}$ and stellar mass varies from a statistically significant positive trend in the panels with locally-calibrated templates to negative trends in luminosity-independent, mass dependent templates driven with stacks of *Herschel* data. However, these trends may not be intrinsic, and may only appear from selection biases and inaccurate L_{IR} estimation. This figure shows a selection bias in identification of mid-IR excess galaxies, as in the lowest mass bin we are unable to detect galaxies with low L_{IR} and low SFR.

Daddi et al. (2007a) find that mid-IR excess source are preferentially in galaxies with large stellar masses and find that the fraction of mid-IR excess galaxies increases with stellar mass. While with the same method in row 2-column 1 we also find a positive correlation, this may only occur due to an overestimation of L_{IR} in massive galaxies. In our best method (row 1-column 7) we find a negative correlation with large errors on the fractions in the low and high mass bins. If we limit our analysis to the 4 middle mass bins, we do find a significant difference between the fraction of mid-IR excess galaxies in these two panels. Investigation of the relation of SFR$_{\rm IR}$ and SFR$_{\rm UV,corr}$ with stellar mass in these two methods can justify this discrepancy. Daddi et al. (2007a) method overestimate L_{IR} in moderately massive to massive galaxies compared to our best method. Also there is a large scatter between SFR$_{\rm UV,corr}$ and stellar mass with Calzetti attenuation curve compared to UV spectral slope measured from SED fitting in MOSDED sample, which result higher SFR$_{\rm UV,corr}$ in massive galaxies with our best method compared to

the correction with Calzetti attenuation curve.

Overall, we find that the relation between SFR/SFR$_{\rm MS}$ and stellar mass, and the fraction of mid-IR excess galaxies in bins of stellar mass strongly depends on the used templates and reddening corrections. Selection biases, inaccurate L_{IR} estimation and variation of reddening correction factor can justify the discrepancies between the trends shown in Figure 4.6.

4.5 Discussion

In this paper we use the data from three years of the MOSDEF survey to investigate the nature of so-called mid-IR excess galaxies which are sources that their combined SFR$_{\rm IR}$ and SFR$_{\rm UV}$ is larger than the dust corrected SFR$_{\rm UV}$ by a factor of three. In this section we first investigate how the UV spectral slope measurements plays an important role in a robust estimation of extinction corrected SFR$_{\rm UV}$. We then investigate the chosen IMF effect on SFR-luminosity calibration and identification of mid-IR excess galaxies. We also discuss how depth of X-ray surveys is important in the stacking analysis of mid-IR excess galaxies. Finally, we compare the fraction of mid-IR excess galaxies identified in this study with Daddi et al. (2007a) .

4.5.1 UV Spectral Slope Measurements

Our analysis in Section 4.4 shows that identification of mid-IR excess is strongly reliant on both L_{IR} estimation and SFR$_{\rm UV}$ extinction correction. While we examine various methods for the reddening correction, we find the combination of the UV slope for reddening correction, and L_{IR} calculated with Dale & Helou (2002) templates using stacks of *Herschel* data in bins of stellar mass result in a median SFR/SFR$_{\rm MS}$ ~ 1 illustrating the consistency between $SFR_{IR} + SFR_{UV}$ and $SFR_{UV,corr}$ measurements. With this combination we obtain the lowest percentage for mid-IR excess galaxies ($18\% \pm 3\%$) in

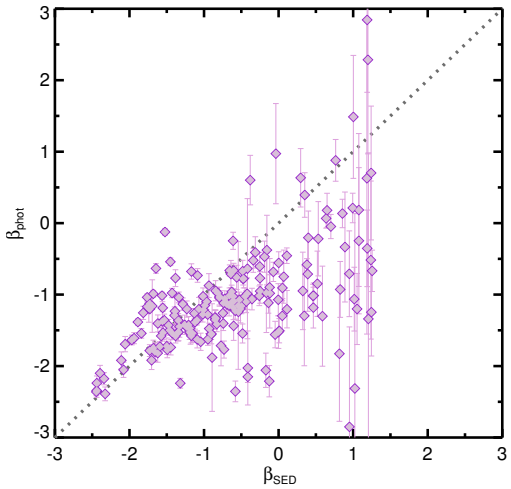

Figure 4.7. The UV spectral slope estimated from fitting a power-law to the photometric data (β_{phot}) at 1200-2600 Å versus the slope estimated from fitting a power-law to the SED fits (β_{SED}). The gray dotted line is the 1–1 line. The large uncertainties on the photometric data lead to the large error bars on (β_{phot}) and $\mathrm{SFR_{UV,corr}}$. On average β_{SED} is larger than β_{phot}, which result in a higher reddening correction of $\mathrm{SFR_{UV}}$, and consequently lower $\mathrm{SFR/SFR_{MS}}$ and lower fraction of mid-IR excess galaxies compared to β_{phot}.

our analysis.

The UV slope in this analysis is measured by fitting power-laws to the SED fits (β_{SED}) at 1200-2600 Å . However, it is also common to estimate the UV slope by fitting power-laws directly to the photometric data (β_{phot}) at these wavelengths (e.g. Reddy et al. 2015). However, using β_{phot} instead of β_{SED} increases the fraction of mid-IR excess galaxies to $44\% \pm 4\%$ and the median $\mathrm{SFR/SFR_{MS}}$ to 2.75 with the same L_{IR} measurements. To investigate the discrepancy between the two methods, in Figure 4.7 we plot β_{phot} versus β_{SED}. While the values are spread around the 1–1 line, the SED slopes dominate the photometric slopes at higher β_{SED} end; this results in a larger extinction correction factor($10^{0.4A_{UV}}$), and consequently a smaller fraction of mid-IR excess galaxies with β_{SED} relative to β_{phot}.

The error bars in Figure 4.7 demonstrate the large uncertainty of β_{phot} measurements, which is due to the large errors on the photometric data, particularly in red galaxies

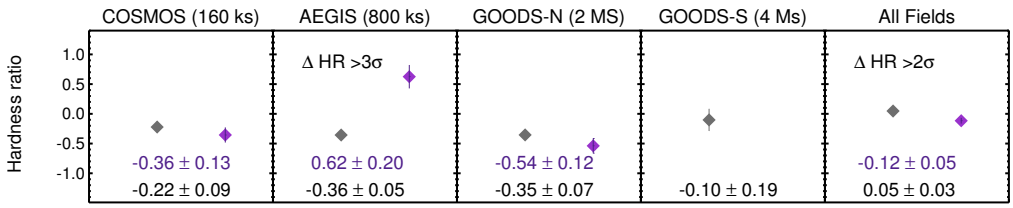

Figure 4.8. The hardness ratio of the X-ray undetected mid-IR excess and MIR-normal galaxies in each of the MOSDEF fields, where SFR/SFR$_{\rm MS}$ is estimated using our best method (row 1- column 7 in Figure 4.3). With shallower X-ray data we may find a hard spectrum due to the obscured AGN population, but in deeper fields, the soft band emission form low luminosity unabsorbed AGN as well as the soft emission from star formation activity dominate in stacking analysis.

that are faint at UV and optical wavelengths. Despite the large errors, β_{phot} provides an estimation of the slope independent of any assumption on the stellar population, while β_{SED} relies on the models adopted in the SED fitting. However, this can turn into a disadvantage in older galaxies with redder slopes due to an older stellar population rather than dust obscuration.

Overall, we find that β_{SED} provides the best estimate of SFR$_{\rm UV,corr}$, and the commonly used β_{phot} underestimates the reddening correction factor. Fitting power-laws to the SED may be more reliable than using the photometry directly due to the larger uncertainties of the photometric data.

4.5.2 IMF Effect on Identification of Mid-IR Excess Galaxies

The chosen IMF plays an important role in the SFR-luminosity calibration and consequently on identification of mid-IR excess galaxies. In our analysis in the result section, we assumed universal constant conversions driven with Salpeter and Chabrier IMF for estimating SFR$_{\rm IR}$ and SFR$_{\rm UV}$ respectively. However, by changing the IMF in each of these conversions (e.g. estimating SFR$_{\rm UV}$ with Salpeter or estimating SFR$_{\rm IR}$ with Chabrier IMF) we find a different SFR/SFR$_{\rm MS}$ and a different fraction of mid-IR excess galaxies than shown in Figures 4.1 to 4.3.

The calibration of SFR indicators relies on the chosen IMF. While some studies accept a constant universal IMF that does not strongly depend on the environment (for a review see Bastian et al. 2010), some others argue that it varies with redshift, metallicity and galaxy formation history (e.g. Wilkins et al. 2008; Cappellari et al. 2012). Changing the IMF may have different effects on the stellar populations with different masses; for instance at the high-mass end ($\sim 100\ M_{\odot}$) adopting Chabrier IMF instead of Salpeter elevates the estimated SFR, while at sub-solar masses it lowers the estimated SFR. The luminosity and SFR that we probe are dominated by stellar populations with masses $\gtrsim 10\ M_{\odot}$, therefore our measurements are reliant on the adopted IMF slope at the intermediate to high-mass regime.

We note that individual SFR indicators may also trace stellar populations at different age and main-sequence lifetime. For instance, the UV luminosity probes the ongoing SFR originating from stars with short main-sequence lifetimes, while IR emission originates from stellar populations covering a large range of age, with timescales varying between 100 Myr to 10 Gyr, respectively in ULIRGS to star-forming galaxies (for a review see Calzetti 2013). Therefore, calibration of luminosity and SFR might be more complicated than a simple conversion driven with a single IMF.

Investigation of universality of IMF, or the SFR-luminosity calibration is beyond the scope of this paper, but variation of SFR-luminosity calibration from the adopted IMF can change the SFR estimation, and the fraction of galaxies identified as mid-IR excess .

4.5.3 AGN Contribution in MIR-Excess and X-ray Depth in Stacking Analysis

Our multi-wavelength AGN analysis, and X-ray stacking analysis in the result section show that it is unlikely for the detected or undetected AGN to contribute significantly to MIR radiation in mid-IR excess galaxies. Using a the same IR templates and

UV dust correction as Daddi et al. (2007a) we find that not only X-ray AGN are more prevalent in mid-IR excess region, but IR and optical AGN show the same behavior as well. A more robust estimation of SFR in our analysis indicate that such a prevalence for the detected AGN in mid-IR excess mainly occurs due to the inaccurate SFR estimation, in particular overestimation of L_{IR} with locally-calibrated templates. More recently with a similar IR template and UV reddening correction as Daddi et al. (2007a) , Rangel et al. (2013) find that at $z \sim 2$ the fraction of X-ray detected AGN above the mid-IR excess threshold is by a factor of 3 higher than those below the threshold. However, they argue that this happens due to a strong correlation between SFR/SFR$_{\rm MS}$ and L_{IR} , and the fractions of the X-ray detected AGN above and below mid-IR excess limit are very similar if considered in small bins of L_{IR} .

Our stacking analysis shows the hardness ratio of X-ray undetected mid-IR excess and MIR-normal galaxies varies with the templates and reddening correction methods. Unlike Daddi et al. (2007a) in most of our combinations we find a harder X-ray spectrum in MIR-normal galaxies than the mid-IR excess population. However with our best combination (row 1- column 7 in Figure 4.3, see also Figure 4.8), we do not a hard spectrum in either mid-IR excess or MIR-normal galaxies. Using the deep X-ray data in CDFN and CDFS fields, Rangel et al. (2013) stacks the X-ray undetected sources and find the hardness ratio of -0.50 ± 0.12 and -0.45 ± 0.15 respectively above and below the mid-IR excess limit in CDFN. Neither of these hardness ratios are suggestive of an underlying obscured AGN activity.

Rangel et al. (2013) also show that by limiting their sample to same depth (1 Ms) as Daddi et al. (2007a) they find a much harder spectrum with the hardness ratio of -0.16 ± 0.16 in mid-IR excess galaxies, and discuss that the relatively harder spectrum in Daddi et al. (2007a) is due to a few undetected X-ray AGN that are detected with their deeper X-ray data. We note that this conclusion shows at least some of the galaxies in

mid-IR excess population in Daddi et al. (2007a) sample are indeed obscured AGN, but does not approve that mid-IR excess occurs only due to the AGN activity as in Daddi et al. (2007a) analysis L_{IR} is systematically overestimated.

While Daddi et al. (2007a) and Rangel et al. (2013) samples are from CDFS and CDFN (see also Alexander et al. 2011), MOSDEF have a more inhomogeneous X-ray depth, varying from field to field, and within individual fields. In Figure 4.8 we show the hardness ratio of the X-ray undetected sample in each of our fields above and below the mid-IR excess limit using our best method for SFR estimations. The number of sources in these fields are 49, 92, 49 and 8 respectively from left to right, and there is no mid-IR excess source in GOODS-S. The depth of the observations in each field is shown on the plot as well.

In the first instance, the variation of the hardness ratio in mid-IR excess population do not seem to follow the same trend by increasing depth (COSMOS-AEGIS compared to AEGIS-GOODS-N). This might be due to the variation of the X-ray observation depth within each field, in order that the hard X-ray signal in AEGIS may arise from areas with a shallower depth than 160 ks of COMSOS. In AEGIS, the hardness ratio shows an underling hard X-ray spectrum in mid-IR excess galaxies, while in GOODS-N it drops to a substantially lower hardness ratio. The hardness ratio in GOODS-N may be due to the soft band radiation from unobscured low luminosity AGN, reflection-dominated component in heavily obscured AGN and/or star-forming galaxies (Rangel et al. 2013), while in AEGIS it is mainly due to an obscured AGN population.

Overall, our stacking analysis do not advocate for a hard X-ray spectrum in mid-IR excess galaxies. But this may change within individual fields depending on the depth of the X-ray observations. The stacked signals of the shallower X-ray data might be dominated by the obscured AGN hard radiation, but in deeper fields those AGN have a higher chance to be detected and being excluded from the stacking analysis. Therefor,

the stacked signals in deeper fields is probably dominated by the soft spectrum from AGN or star-forming galaxies.

4.5.4 Comparison with Daddi et al. (2007a)

contribution from PAH molecules.

Our best combination of SFR estimators shows that $18\% \pm 3\%$ of the galaxies in MOSDEF are mid-IR excess ; Daddi et al. (2007a) find that between 20-30% of their BzK selected galaxies at $z \sim 2$ sample show this excess. While the fraction of the mid-IR excess population in MOSDEF is not substantially smaller than Daddi's, it worth mentioning that with a similar SFR estimation to Daddi et al. in Figure 4.1 we identify 65% of our sources as mid-IR excess galaxies. This high percentage is due to the shallower 24 μmdata in our sample, and also lower reddening correction factors in our analysis compared to Daddi et al.. Investigation of the 24 μmdata indicates that on average, L_8 in MOSDEF 24 μmdetected galaxies is smaller than Daddi et al. by a factor of 2.

While Daddi et al. (2007a) attribute the excess in MIR radiation to the contribution from obscured AGN, we do not find any strong evidence for AGN contribution. We note the 24 μmdata in our sample may also trace the radiation from PAH molecules at rest-frame wavelengths of 5–12 μmShivaei et al. (2017). While the strength of PAH molecules varies with stellar mass and metallicity (e.g. Engelbracht et al. 2006; Smith et al. 2007; Shivaei et al. 2017), Smith et al. (2007) find that they may contribute up to 20% to the bolometric IR luminosity. Therefore the excess at MIR wavelength in our sample could be due to the radiation from PAH instead of obscured AGN population.

4.6 Summary

In this paper we use the data from the first three years of the MOSDEF survey to study the nature of mid-IR excess galaxies. We use Daddi et al. (2007a) definition for mid-IR excess galaxies, which classify them as those with the ratio of the combined SFR_{IR} and SFR_{UV} to the extinction corrected SFR_{UV} exceeding a factor of three. We limit our analysis to the galaxies with significant 24 μmdetection, and to ensure that 24 μmdata traces the rest-frame 8 μmdata we further restrict our analysis to 198 galaxy and AGN at $z < 2.61$. We investigate the templates from various studies for L_{IR} estimation as well as various reddening correction methods, and identify the best combination as the one generating SFR_{IR} + $SFR_{UV} \sim SFR_{UV,corr}$. We investigate how different combinations of templates and reddening corrections result in identification of a different fraction of our sample as mid-IR excess galaxies. We further investigate the contribution form AGN in the excess MIR radiation. Our main conclusions are as follows:

- We find the identification of mid-IR excess galaxies is strongly reliant on both SFR_{IR} estimation and SFR_{UV} dust reddening correction. Our most robust SFR estimation indicate that $18\% \pm 3\%$ of the MOSDEF sample are mid-IR excess galaxies.

- We find that the bolometric IR luminosity estimated from locally-calibrated, luminosity dependent templates overestimate L_{IR} and SFR_{IR} in $z \sim 2$ galaxies. Our analysis shows that the mass-dependent, luminosity-independent templates driven when *Herschel* FIR data is included provide a more robust L_{IR} estimation at higher redshifts, which result in identification of smaller population of galaxies as MIR-excess.

- We find that the UV spectral slope estimated by fitting power-laws to the SED fits at UV wavelength provides a more reliable reddening correction factor than an

average attenuation curve. The UV spectral slope can also be measured by fitting power-laws directly to the photometric data. We find the photometric slopes lead to the identification of a higher fraction of galaxies as mid-IR excess . However, due to the errors on the photometry, the uncertainty on the extinction correction factor from photometric slopes is a larger than the SED slopes.

- With a reliable estimation of SFR_{IR} and dust corrected SFR_{UV} , investigation of the detected AGN in mid-IR excess galaxies do not indicate a higher prevalence for X-ray, IR or optical AGN in mid-IR excess galaxies that the normal galaxies.

- Stacking the X-ray undetected galaxies in MOSDEF does not reveal a hard X-ray spectrum in mid-IR excess galaxies. However, we find that the result of X-ray stacking analysis relies on the depth of the X-ray observations in each field, as we do not a uniform X-ray depth in MOSDEF fields. Stacking the X-ray undetected galaxies in shallower fields may reveal a harder spectrum in mid-IR excess galaxies but as depth of X-ray data increases the mid-IR excess galaxies reveal a softer spectrum. The softer signal in deeper fields could be due to variety of phenomena from reflection-dominated radiation in obscured AGN to soft radiation from low luminosity unobscured AGN or star-forming galaxies.

Overall, our analysis in this study indicate that $\sim 20\%$ of the our $z \sim 2$ sample in MOSDEF are mid-IR excess galaxies. We discussed the effects of various IR templates, dust reddening correction methods and IMF assumption in identification of this population. We note that we note that the depth of the 24 μmdata plays a very important role in this analysis, as a deeper MIR dataset may result in a identification of a lower fraction of galaxies as MIR-excess.

ACKNOWLEDGEMENTS

We thank the MOSFIRE instrument team for building this powerful instrument, and for taking data for us during their commissioning runs. This work would not have been possible without the 3D-HST collaboration, who provided us the spectroscopic and photometric catalogs used to select our targets and to derive stellar population parameters. Based on observations made with the NASA/ESA Hubble Space Telescope, which is operated by the Association of Universities for Research in Astronomy, Inc., under NASA contract NAS 5-26555. These observations are associated with programs 12177, 12328, 12060-12064, 12440- 12445, 13056. Funding for the MOSDEF survey is provided by NSF AAG grants AST-1312780, 1312547, 1312764, and 1313171 and grant AR-13907 from the Space Telescope Science Institute. A.L.C. acknowledges support from NSF CAREER award AST-1055081. N.A.R. is supported by an Alfred P. Sloan Research Fellowship. JA acknowledges support from ERC Advanced Grant FEEDBACK 340442. The data presented herein were obtained at the W. M. Keck Observatory, which is operated as a scientific partnership among the California Institute of Technology, the University of California and the National Aeronautics and Space Administration. The Observatory was made possible by the generous financial support of the W. M. Keck Foundation. The authors wish to recognize and acknowledge the very significant cultural role and reverence that the summit of Mauna Kea has always had within the indigenous Hawaiian community. We are most fortunate to have the opportunity to conduct observations from this mountain.

Chapter 4 is a draft of material that will be submitted to The Astrophysical Journal, Azadi, M., Coil, A., Aird, J., Reddy, N., Shivaei, I., Shapley, A., Freeman, W., Kriek, M., Leung, GCK., Mobasher, B., Price, S., Sanders, R., Siana, B., Zick, T. 2017. The dissertation author is the primary investigator and author of this paper.

Chapter 5

Conclusions and Future Work

In this dissertation we investigate various methods of AGN identification, the physical properties of AGN identified at various wavelengths, the physical properties of the host galaxies, and the nature of galaxies with MIR-excess.

In Chapter 2, we consider the relationship between AGN X-ray luminosity and their host galaxies' SFR using a sample of 309 X-ray selected Type 2 AGN with spectroscopic redshifts at $0.2 < z < 1.2$ from the PRIMUS survey. AGN with a wide range of $L_{\rm X}$ reside in both star forming and quiescent galaxies with a wide range of stellar masses, although are mainly found in moderately massive ($\gtrsim 10^{10}{\rm M}_{\odot}$) galaxies. However, we do not find any correlation between stellar mass and $L_{\rm X}$ within our X-ray AGN sample for either the star forming or quiescent populations. We find that AGN luminosity and SFR are not strongly correlated in star-forming galaxies. However, we do find a weak but statistically significant correlation between the average $L_{\rm X}$ of AGN and SFR in star-forming galaxies . This correlation implies an underlying connection that may exist due to a common gas supply but the variability of AGN accretion on relatively short timescales makes it hard to observe. We find that the probability that a galaxy of a given stellar mass and redshift hosts an AGN as a function of specific accretion rate is roughly a power law for both star-forming and quiescent host galaxies. This probability increases with SFR in quiescent galaxies, though within the star forming population there is no

change across the "main sequence" of star formation. This indicates that enhanced star formation does not go hand-in-hand with increased SMBH growth, but as star formation is shut down there is also a reduction of AGN activity in quiescent galaxies.

In Chapter 3, we consider a sample of 55 AGN using the X-ray imaging data from *Chandra*, mid-IR data from IRAC camera on *Spitzer*, and rest-frame optical spectra from MOSDEF survey. We find that AGN identified at any wavelength are biased against low mass host galaxies; this is an observational selection bias. IR AGN identification has an additional bias against the most massive galaxies as in these galaxies the radiation from star formation activity dominates over the AGN light. Comparing the distributions of SFR for IR and optical AGN, we find that IR AGN are primarily identified in galaxies with relatively higher SFR, while optical AGN are identified in galaxies with relatively lower SFR. X-ray selection does not display any bias in star formation. Within the star-forming galaxy population, once stellar mass selection biases are taken into account, we find that AGN reside in galaxies with similar physical properties (SFR, dust content, and stellar age) as inactive galaxies.

The majority of the AGNs in our sample can be identified using optical diagnostics, indicating the reliability of optical AGN selection. However, optical identification is limited by the quality of the spectroscopic data, as optical emission lines in most of the non-optical AGN in our sample at $z \sim 2$ are contaminated by sky lines. Almost half of the IR AGN in our sample are recovered at X-ray or optical wavelengths. IR imaging provides a more uniform depth than X-ray data and is not affected by the quality of optical spectroscopy; thus IR AGN identification can improve the completeness of AGN samples at $z \sim 2$. Overall, we find no evidence of AGN activity in particular types of galaxies, which is consistent with stochastic fueling of AGN in any kind of galaxy, and no strong evidence for AGN feedback. Our investigation shows that in order to obtain a more complete AGN census, complementary identification techniques at multiple wavelengths

are required. To robustly study AGN host galaxy properties, the selection biases from each identification technique should be taken into account.

In Chapter 4 we use a sample of $\sim$200 galaxies and AGN with significant 24 μm detections from MIPS on the *Spitzer* satellite to investigate the nature of so-called "mid-infrared (MIR) excess" galaxies. These are sources that have a SFR inferred from mid-infrared data that is substantially elevated relative to that estimated from UV data, after correcting for dust. We find that the identification of these galaxies is heavily reliant on the SFR estimator used and dust reddening corrections.

Our analysis indicates that commonly-used extrapolations of the total SFR from the observed 24 μm band, using luminosity-dependent templates based on local galaxies, overestimate the total IR luminosity and SFR in $z \sim 2$ galaxies. We find that by including *Herschel* FIR observations, with a stellar mass-dependent, luminosity-independent template we can obtain a more reliable estimate of the SFR, consistent with other star formation tracers. Additionally, while the SFR estimated from reddening-corrected UV observations should be robust, we find that the extinction correction method used plays a critical role in this estimation and in the identification of MIR-excess galaxies. Using multi-wavelength AGN data from the MOSDEF survey, we do not find a higher prevalence for AGN in MIR-excess galaxies relative to MIR-normal galaxies, unlike previous studies. Specifically, our X-ray stacking analysis does not reveal a harder spectrum in MIR-excess galaxies than MIR-normal galaxies. Altogether, our analysis does not indicate that AGN activity contributes to the MIR-excess, which implies that this phenomena may be due primarily to emission from PAH dust molecules.

Living in a golden age of observational astronomy and with the coming generation of telescopes, we can tackle the fundamental questions about galaxy and AGN evolution. Unveiling the physical processes that transform star-forming galaxies to red and dead ellipticals is a key step in understanding galaxy evolution. While AGN feedback is

thought to play an important role in galaxy evolution, the results of this dissertation do not advocate for a widespread, strong impact from AGN on their host galaxies. However, this may not be the case for AGN residing in merging galaxies, which may have a different fueling process and stronger feedback.

Galaxy mergers are an important process in galaxy evolution and may be responsible for triggering starbursts as well as intense periods of AGN activity. Merging galaxies can be observed in different stages of their evolutionary track, from pairs separated by hundreds of kpc to coalesced galaxies. The SMBHs at the center of each of the merging galaxies eventually evolve to a gravitationally-bound SMBH binary. During this transition, either of the two SMBHs might begin accreting. AGN pairs with kpc-scale separation and offset-AGN (with one active and one inactive SMBH) have become a popular target for many studies in the past few years (e.g. **??**) as they can provide a clear picture of merger-driven fueling process.

In galaxy evolution, dual SMBHs are expected to be common. However, only a small number of dual systems have been identified so far, owing to the significant challenges involved in detecting and resolving the two AGN components with separation < 10 kpc. The most reliable dual AGN candidates are those identified spectroscopically with double-peak emission lines. AGN-driven outflows can also result in double-peak narrow lines, and follow-up of these systems to distinguish outflows from dual candidates are required. While studies find that the fraction of dual AGN increases significantly with redshift (e.g. **?**), identification of these sources at $z \sim 2$, where the Universe has been most active, is very challenging. With the new generation of NIR spectrographs on the VLT and Keck telescope the rest-frame optical spectra for large samples of galaxies and AGN at $z \sim 2$ can be obtained, and dual or offset-AGN can be identified at higher redshifts. The preliminary investigations using the MOSDEF survey data indicate that the dual AGN have, on average, higher Eddington ratios than other Type 2 AGN, which may propose

a different fueling mechanism due to the different nature of the host galaxies. Using integral-field spectroscopy, we can perform spatially resolved emission line diagnostics in different regions of the host galaxy, and study spatial distributions and kinematic of ionized gas around the AGN.

Bibliography

Aird, J., Coil, A. L., Georgakakis, A., Nandra, K., Barro, G., & Pérez-González, P. G. 2015, MNRAS, 451, 1892

Aird, J., Coil, A. L., Moustakas, J., Blanton, M. R., Burles, S. M., Cool, R. J., & Eisenstein, D. J. 2012, ApJ, 746, 90

Aird, J., Coil, A. L., Moustakas, J., Diamond-Stanic, A. M., Blanton, M. R., Cool, R. J., & Eisenstein, D. J. 2013, ApJ, 775, 41

Aird, J., Nandra, K., Laird, E., Georgakakis, A., Ashby, M. L., Barmby, P., Coil, A. L., Huang, J. S., Koekemoer, A. M., & Steidel, C. C. 2010, MNRAS, 401, 2531

Akylas, A., & Georgantopoulos, I. 2009, A&A, 500, 999

Alexander, D., & Hickox, R. 2012, NAR, 56, 93

Alexander, D. M., Bauer, F. E., Brandt, W. N., Daddi, E., Hickox, R. C., Lehmer, B. D., Luo, B., Xue, Y. Q., Young, M., Comastri, A., Del Moro, A., Fabian, A. C., Gilli, R., Goulding, A. D., Mainieri, V., Mullaney, J. R., Paolillo, M., Rafferty, D. A., Schneider, D. P., Shemmer, O., & Vignali, C. 2011, ApJ, 738, 44

Alonso-Herrero, A., Pérez-González, P. G., Rieke, G. H., Alexander, D. M., Rigby, J. R., Papovich, C., Donley, J. L., & Rigopoulou, D. 2008, ApJ, 677, 127

Alonso-Herrero, A., Pérez-González, P. G., Alexander, D. M., Rieke, G. H., Rigopoulou, D., Le Floc'h, E., Barmby, P., Papovich, C., Rigby, J. R., Bauer, F. E., Brandt, W. N., Egami, E., Willner, S. P., Dole, H., & Huang, J.-S. 2006, ApJ, 640, 167

Antonucci, R. 1993, ARA&A, 31, 473

Assef, R. J., Kochanek, C. S., Ashby, M. L. N., Brodwin, M., & Brown, M. J. I. 2011, ApJ, 728, 56

Assef, R. J., Kochanek, C. S., Brodwin, M., Cool, R., Forman, W., Gonzalez, A. H., Hickox, R. C., Jones, C., Le Floc'h, E., Moustakas, J., Murray, S. S., & Stern, D. 2010, ApJ, 713, 970

Azadi, M., Aird, J., Coil, A. L., Moustakas, J., Mendez, A. J., Blanton, M. R., Cool, R. J., Eisenstein, D. J., Wong, K. C., & Zhu, G. 2015, ApJ, 806, 187

Azadi, M., Coil, A. L., Aird, J., Reddy, N., Shapley, A., Freeman, W. R., Kriek, M., Leung, G. C. K., Mobasher, B., Price, S. H., Sanders, R. L., Shivaei, I., & Siana, B. 2017, ApJ, 835, 27

Baldry, I. K., Glazebrook, K., Brinkmann, J., Ivezić, Ž., Lupton, R. H., Nichol, R. C., & Szalay, A. S. 2004, ApJ, 600, 681

Baldwin, J. A., Phillips, M. M., & Terlevich, R. 1981, PASP, 93, 5

Barth, A. J., Ho, L. C., Rutledge, R. E., & Sargent, W. L. W. 2004, ApJ, 607, 90

Bastian, N., Covey, K. R., & Meyer, M. R. 2010, ARA&A, 48, 339

Bell, E. F., McIntosh, D. H., Katz, N., & Weinberg, M. D. 2003, ApJS, 149, 289

Bell, E. F., Papovich, C., Wolf, C., Le Floc'h, E., Caldwell, J. A. R., Barden, M., Egami, E., McIntosh, D. H., Meisenheimer, K., Pérez-González, P. G., Rieke, G. H., Rieke, M. J., Rigby, J. R., & Rix, H.-W. 2005, ApJ, 625, 23

Bernhard, E., Mullaney, J. R., Daddi, E., Ciesla, L., & Schreiber, C. 2016, MNRAS, 460, 902

Berta, S., Magnelli, B., Nordon, R., Lutz, D., Wuyts, S., Altieri, B., Andreani, P., Aussel, H., Castañeda, H., Cepa, J., Cimatti, A., Daddi, E., Elbaz, D., Förster Schreiber, N. M., Genzel, R., Le Floc'h, E., Maiolino, R., Pérez-Fournon, I., Poglitsch, A., Popesso, P., Pozzi, F., Riguccini, L., Rodighiero, G., Sanchez-Portal, M., Sturm, E., Tacconi, L. J., & Valtchanov, I. 2011, A&A, 532, A49

Blanton, M. R., Hogg, D. W., Bahcall, N. A., Brinkmann, J., & Britton, M. 2003, ApJ, 592, 819

Bongiorno, A., Merloni, A., Brusa, M., Magnelli, B., Salvato, M., Mignoli, M., Zamorani, G., Fiore, F., Rosario, D., Mainieri, V., Hao, H., Comastri, A., Vignali, C., Balestra, I., Bardelli, S., Berta, S., Civano, F., Kampczyk, P., Le Floc'h, E., Lusso, E., Lutz, D., Pozzetti, L., Pozzi, F., Riguccini, L., Shankar, F., & Silverman, J. 2012, MNRAS, 427,

3103

Bouwens, R. J., Aravena, M., Decarli, R., Walter, F., da Cunha, E., Labbé, I., Bauer, F. E., Bertoldi, F., Carilli, C., Chapman, S., Daddi, E., Hodge, J., Ivison, R. J., Karim, A., Le Fevre, O., Magnelli, B., Ota, K., Riechers, D., Smail, I. R., van der Werf, P., Weiss, A., Cox, P., Elbaz, D., Gonzalez-Lopez, J., Infante, L., Oesch, P., Wagg, J., & Wilkins, S. 2016, ApJ, 833, 72

Boyle, B. J., & Terlevich, R. J. 1998, MNRAS, 293, L49

Brammer, G. B., van Dokkum, P. G., & Coppi, P. 2008, ApJ, 686, 1503

Brammer, G. B., van Dokkum, P. G., Franx, M., Fumagalli, M., Patel, S., Rix, H.-W., Skelton, R. E., Kriek, M., Nelson, E., Schmidt, K. B., Bezanson, R., da Cunha, E., Erb, D. K., Fan, X., Förster Schreiber, N., Illingworth, G. D., Labbé, I., Leja, J., Lundgren, B., Magee, D., Marchesini, D., McCarthy, P., Momcheva, I., Muzzin, A., Quadri, R., Steidel, C. C., Tal, T., Wake, D., Whitaker, K. E., & Williams, A. 2012, ApJS, 200, 13

Brandt, W. N., & Alexander, D. M. 2015, A&A Rv, 23, 1

Brightman, M., Nandra, K., Salvato, M., Hsu, L.-T., Aird, J., & Rangel, C. 2014, MNRAS, 443, 1999

Brinchmann, J., Charlot, S., White, S. D. M., Tremonti, C., Kauffmann, G., Heckman, T., & Brinkmann, J. 2004, MNRAS, 351, 1151

Brusa, M., Zamorani, G., Comastri, A., & Hasinger, G. 2007a, ApJS, 172, 353

—. 2007b, ApJS, 172, 353

Buchner, J., Georgakakis, A., Nandra, K., Brightman, M., Menzel, M.-L., Liu, Z., Hsu, L.-T., Salvato, M., Rangel, C., Aird, J., Merloni, A., & Ross, N. 2015, ApJ, 802, 89

Bundy, K., Ellis, R. S., Conselice, C. J., Taylor, J. E., Cooper, M. C., Willmer, C. N., Weiner, B. J., Coil, A. L., Noeske, K. G., & Eisenhardt, P. R. 2006, The Astrophysical Journal, 651, 120

Calzetti, D. 2013, Star Formation Rate Indicators, ed. J. Falcón-Barroso & J. H. Knapen, 419

Calzetti, D., Armus, L., Bohlin, R. C., Kinney, A. L., Koornneef, J., & Storchi-Bergmann, T. 2000, ApJ, 533, 682

Calzetti, D., Kinney, A. L., & Storchi-Bergmann, T. 1994, ApJ, 429, 582

Calzetti, D., Kennicutt, Jr., R. C., Bianchi, L., Thilker, D. A., Dale, D. A., Engelbracht, C. W., Leitherer, C., Meyer, M. J., Sosey, M. L., Mutchler, M., Regan, M. W., Thornley, M. D., Armus, L., Bendo, G. J., Boissier, S., Boselli, A., Draine, B. T., Gordon, K. D., Helou, G., Hollenbach, D. J., Kewley, L., Madore, B. F., Martin, D. C., Murphy, E. J., Rieke, G. H., Rieke, M. J., Roussel, H., Sheth, K., Smith, J. D., Walter, F., White, B. A., Yi, S., Scoville, N. Z., Polletta, M., & Lindler, D. 2005, ApJ, 633, 871

Cameron, E. 2011, PASA, 28, 128

Canalizo, G., & Stockton, A. 2001, ApJ, 555, 719

Cappellari, M., McDermid, R. M., Alatalo, K., Blitz, L., Bois, M., Bournaud, F., Bureau, M., Crocker, A. F., Davies, R. L., Davis, T. A., de Zeeuw, P. T., Duc, P.-A., Emsellem, E., Khochfar, S., Krajnović, D., Kuntschner, H., Lablanche, P.-Y., Morganti, R., Naab, T., Oosterloo, T., Sarzi, M., Scott, N., Serra, P., Weijmans, A.-M., & Young, L. M. 2012, Nature, 484, 485

Cardamone, C. N., Urry, C. M., Schawinski, K., Treister, E., Brammer, G., & Gawiser, E. 2010, ApJL, 721, L38

Cardelli, J. A., Clayton, G. C., & Mathis, J. S. 1989, ApJ, 345, 245

Chabrier, G. 2003, PASP, 115, 763

Chabrier, G. 2003, PASP, 115, 763

Charlot, S., & Fall, S. 2000, ApJ, 539, 718

Chary, R., & Elbaz, D. 2001, ApJ, 556, 562

Chen, C.-T. J., Hickox, R. C., Alberts, S., Brodwin, M., Jones, C., Murray, S. S., Alexander, D. M., Assef, R. J., Brown, M. J. I., Dey, A., Forman, W. R., Gorjian, V., Goulding, A. D., Le Floc'h, E., Jannuzi, B. T., Mullaney, J. R., & Pope, A. 2013, ApJ, 773, 3

Ciliegi, P., Zamorani, G., Hasinger, G., Lehmann, I., Szokoly, G., & Wilson, G. 2003a, A&A, 398, 901

—. 2003b, A&A, 398, 901

Coil, A. L., Blanton, M. R., Burles, S. M., Cool, R. J., & Eisenstein, D. J. 2011, ApJ, 741, 8

Coil, A. L., Georgakakis, A., Newman, J. A., Cooper, M. C., & Croton, D. 2009, ApJ, 701, 1484

Coil, A. L., Aird, J., Reddy, N., Shapley, A. E., Kriek, M., Siana, B., Mobasher, B., Freeman, W. R., Price, S. H., & Shivaei, I. 2015, ApJ, 801, 35

Comastri, A., Ranalli, P., Iwasawa, K., Vignali, C., Gilli, R., Georgantopoulos, I., Barcons, X., Brandt, W. N., Brunner, H., Brusa, M., Cappelluti, N., Carrera, F. J., Civano, F., Fiore, F., Hasinger, G., Mainieri, V., Merloni, A., Nicastro, F., Paolillo, M., Puccetti, S., Rosati, P., Silverman, J. D., Tozzi, P., Zamorani, G., Balestra, I., Bauer, F. E., Luo, B., & Xue, Y. Q. 2011, A&A, 526, L9

Conroy, C., & Gunn, J. E. 2010, ApJ, 712, 833

Conroy, C., Gunn, J. E., & White, M. 2009, ApJ, 699, 486

Conroy, C., Gunn, J. E., & White, M. 2009, ApJ, 699, 486

Conselice, C. J. 2014, ARA&A, 52, 291

Cool, R. J., Moustakas, J., Blanton, M. R., Burles, S. M., & Coil, A. L. 2013, ApJ, 767, 118

Cowley, M. J., Spitler, L. R., Tran, K.-V. H., Rees, G. A., Labbé, I., Allen, R. J., Brammer, G. B., Glazebrook, K., Hopkins, A. M., Juneau, S., Kacprzak, G. G., Mullaney, J. R., Nanayakkara, T., Papovich, C., Quadri, R. F., Straatman, C. M. S., Tomczak, A. R., & van Dokkum, P. G. 2016, MNRAS, 457, 629

Daddi, E., Alexander, D. M., Dickinson, M., Gilli, R., Renzini, A., Elbaz, D., Cimatti, A., Chary, R., Frayer, D., Bauer, F. E., Brandt, W. N., Giavalisco, M., Grogin, N. A., Huynh, M., Kurk, J., Mignoli, M., Morrison, G., Pope, A., & Ravindranath, S. 2007a, ApJ, 670, 173

—. 2007b, ApJ, 670, 173

—. 2007c, ApJ, 670, 173

Daddi, E., Elbaz, D., Walter, F., Bournaud, F., Salmi, F., Carilli, C., Dannerbauer, H., Dickinson, M., Monaco, P., & Riechers, D. 2010, ApJ, 714, L118

Dai, Y. S., Wilkes, B. J., Bergeron, J., Omont, A., Kuraszkiewicz, J., & Teplitz, H. I. 2015, ArXiv e-prints, arXiv:1511.06761

Dale, D. A., & Helou, G. 2002, ApJ, 576, 159

Dale, D. A., Helou, G., Contursi, A., Silbermann, N. A., & Kolhatkar, S. 2001, ApJ, 549, 215

Della Ceca, R., Severgnini, P., Caccianiga, A., Comastri, A., Gilli, R., Fiore, F., Piconcelli, E., Malaguti, P., & Vignali, C. 2008, Mem. Soc. Astron. Italiana, 79, 65

Di-Matteo, T., Springel, V., & Hernquist, L. 2005, Nature, 433, 604

Diamond-Stanic, A. M., & Rieke, G. 2012, ApJ, 746, 168

Dickinson, M., & FIDEL Team. 2007, in Bulletin of the American Astronomical Society, Vol. 39, American Astronomical Society Meeting Abstracts, 822

Donley, J. L., Rieke, G. H., Pérez-González, P. G., & Barro, G. 2008, ApJ, 687, 111

Donley, J. L., Rieke, G. H., Pérez-González, P. G., Rigby, J. R., & Alonso-Herrero, A. 2007, ApJ, 660, 167

Donley, J. L., Koekemoer, A. M., Brusa, M., Capak, P., Cardamone, C. N., Civano, F., Ilbert, O., Impey, C. D., Kartaltepe, J. S., Miyaji, T., Salvato, M., Sanders, D. B., Trump, J. R., & Zamorani, G. 2012, ApJ, 748, 142

Dunlop, J. S., McLure, R. J., Kukula, M. J., Baum, S. A., O'Dea, C. P., & Hughes, D. H. 2003, MNRAS, 340, 1095

Elbaz, D., Daddi, E., Le Borgne, D., Dickinson, M., Alexander, D. M., Chary, R.-R., Starck, J.-L., Brandt, W. N., Kitzbichler, M., MacDonald, E., Nonino, M., Popesso, P., Stern, D., & Vanzella, E. 2007a, A&A, 468, 33

—. 2007b, A&A, 468, 33

Elbaz, D., Hwang, H. S., Magnelli, B., et al. 2010, A&A, 518, L29

Elbaz, D., Dickinson, M., Hwang, H. S., Díaz-Santos, T., Magdis, G., Magnelli, B., Le Borgne, D., Galliano, F., Pannella, M., Chanial, P., Armus, L., Charmandaris, V., Daddi, E., Aussel, H., Popesso, P., Kartaltepe, J., Altieri, B., Valtchanov, I., Coia, D., Dannerbauer, H., Dasyra, K., Leiton, R., Mazzarella, J., Alexander, D. M., Buat,

V., Burgarella, D., Chary, R.-R., Gilli, R., Ivison, R. J., Juneau, S., Le Floc'h, E., Lutz, D., Morrison, G. E., Mullaney, J. R., Murphy, E., Pope, A., Scott, D., Brodwin, M., Calzetti, D., Cesarsky, C., Charlot, S., Dole, H., Eisenhardt, P., Ferguson, H. C., Förster Schreiber, N., Frayer, D., Giavalisco, M., Huynh, M., Koekemoer, A. M., Papovich, C., Reddy, N., Surace, C., Teplitz, H., Yun, M. S., & Wilson, G. 2011, A&A, 533, A119

Ellison, S. L., Teimoorinia, H., Rosario, D. J., & Mendel, J. T. 2016, MNRAS, 458, L34

Elvis, M., Civano, F., Vignali, C., & Puccetti, S. 2009, ApJS, 184, 158

Engelbracht, C. W., Kundurthy, P., Gordon, K. D., Rieke, G. H., Kennicutt, R. C., Smith, J.-D. T., Regan, M. W., Makovoz, D., Sosey, M., Draine, B. T., Helou, G., Armus, L., Calzetti, D., Meyer, M., Bendo, G. J., Walter, F., Hollenbach, D., Cannon, J. M., Murphy, E. J., Dale, D. A., Buckalew, B. A., & Sheth, K. 2006, ApJ, 642, L127

Fazio, G. G., Hora, J. L., Allen, L. E., Ashby, M. L. N., Barmby, P., Deutsch, L. K., Huang, J.-S., Kleiner, S., Marengo, M., Megeath, S. T., Melnick, G. J., Pahre, M. A., Patten, B. M., Polizotti, J., Smith, H. A., Taylor, R. S., Wang, Z., Willner, S. P., Hoffmann, W. F., Pipher, J. L., Forrest, W. J., McMurty, C. W., McCreight, C. R., McKelvey, M. E., McMurray, R. E., Koch, D. G., Moseley, S. H., Arendt, R. G., Mentzell, J. E., Marx, C. T., Losch, P., Mayman, P., Eichhorn, W., Krebs, D., Jhabvala, M., Gezari, D. Y., Fixsen, D. J., Flores, J., Shakoorzadeh, K., Jungo, R., Hakun, C., Workman, L., Karpati, G., Kichak, R., Whitley, R., Mann, S., Tollestrup, E. V., Eisenhardt, P., Stern, D., Gorjian, V., Bhattacharya, B., Carey, S., Nelson, B. O., Glaccum, W. J., Lacy, M., Lowrance, P. J., Laine, S., Reach, W. T., Stauffer, J. A., Surace, J. A., Wilson, G., Wright, E. L., Hoffman, A., Domingo, G., & Cohen, M. 2004, ApJS, 154, 10

Ferrarese, L., & Merritt, D. 2000, ApJL, 539, L9

Fiore, F., Grazian, A., Santini, P., Puccetti, S., Brusa, M., Feruglio, C., Fontana, A., Giallongo, E., Comastri, A., Gruppioni, C., Pozzi, F., Zamorani, G., & Vignali, C. 2008, ApJ, 672, 94

Floyd, D. J. E., Dunlop, J. S., Kukula, M. J., Brown, M. J. I., McLure, R. J., Baum, S. A., & O'Dea, C. P. 2013, MNRAS, 429, 2

Floyd, D. J. E., Kukula, M. J., Dunlop, J. S., McLure, R. J., Miller, L., Percival, W. J., Baum, S. A., & O'Dea, C. P. 2004, MNRAS, 355, 196

Gebhardt, K., Bender, R., Bower, G., & Dressler, A. 2000, ApJL, 539, L13

Gehrels, N. 1986, ApJ, 303, 336

Genzel, R., Förster Schreiber, N. M., Rosario, D., Lang, P., Lutz, D., Wisnioski, E., Wuyts, E., Wuyts, S., Bandara, K., Bender, R., Berta, S., Kurk, J., Mendel, J. T., Tacconi, L. J., Wilman, D., Beifiori, A., Brammer, G., Burkert, A., Buschkamp, P., Chan, J., Carollo, C. M., Davies, R., Eisenhauer, F., Fabricius, M., Fossati, M., Kriek, M., Kulkarni, S., Lilly, S. J., Mancini, C., Momcheva, I., Naab, T., Nelson, E. J., Renzini, A., Saglia, R., Sharples, R. M., Sternberg, A., Tacchella, S., & van Dokkum, P. 2014, ApJ, 796, 7

Georgakakis, A., & Nandra, K. 2011, MNRAS, 414, 992

Georgakakis, A., Pérez-González, P. G., Fanidakis, N., Salvato, M., Aird, J., Messias, H., Lotz, J. M., Barro, G., Hsu, L.-T., Nandra, K., Rosario, D., Cooper, M. C., Kocevski, D. D., & Newman, J. A. 2014a, MNRAS, 440, 339

—. 2014b, MNRAS, 440, 339

—. 2014c, MNRAS, 440, 339

Georgantopoulos, I., Georgakakis, A., Rowan-Robinson, M., & Rovilos, E. 2008, A&A, 484, 671

Gilli, R., Comastri, A., & Hasinger, G. 2007, A&A, 463, 79

Goldader, J. D., Meurer, G., Heckman, T. M., Seibert, M., Sanders, D. B., Calzetti, D., & Steidel, C. C. 2002, ApJ, 568, 651

Goulding, A. D., & Alexander, D. M. 2009, MNRAS, 398, 1165

Goulding, A. D., Forman, W. R., Hickox, R. C., Jones, C., Murray, S. S., Paggi, A., Ashby, M. L. N., Coil, A. L., Cooper, M. C., Huang, J.-S., Kraft, R., Newman, J. A., Weiner, B. J., & Willner, S. P. 2014, ApJ, 783, 40

Grogin, N. A., Kocevski, D. D., Faber, S. M., et al. 2011, ApJS, 197, arXiv:1105.3753

Groves, B. A., Heckman, T. M., & Kauffmann, G. 2006, MNRAS, 371, 1559

Guth, A. H. 1981, Phys Rev D, 23, 347

Hainline, K. N., Shapley, A. E., Greene, J. E., Steidel, C. C., Reddy, N. A., & Erb, D. K. 2012, ApJ, 760, 74

Hao, H., Elvis, M., Civano, F., & Lawrence, A. 2011, ApJ, 733, 108

Harrison, C. M., Alexander, D. M., Mullaney, J. R., & Altieri, B. 2012, ApJL, 760, L15

Harrison, C. M., Alexander, D. M., Mullaney, J. R., Stott, J. P., Swinbank, A. M., Arumugam, V., Bauer, F. E., Bower, R. G., Bunker, A. J., & Sharples, R. M. 2016, MNRAS, 456, 1195

Hasinger, G., Cappelluti, N., Brunner, H., & Brusa, M. 2007, ApJS, 172, 29

Heckman, T. M., & Best, P. N. 2014, ARA&A, 52, 589

Heckman, T. M., & Kauffmann, G. 2006, NAR, 50, 677

Heckman, T. M., Kauffmann, G., Brinchmann, J., Charlot, S., Tremonti, C., & White, S. D. M. 2004, ApJ, 613, 109

Heckman, T. M., Ptak, A., Hornschemeier, A., & Kauffmann, G. 2005, ApJ, 634, 161

Hernán-Caballero, A., Alonso-Herrero, A., Pérez-González, P. G., Barro, G., Aird, J., Ferreras, I., Cava, A., Cardiel, N., Esquej, P., Gallego, J., Nandra, K., & Rodríguez-Zaurín, J. 2014a, ArXiv e-prints, arXiv:1404.2056

—. 2014b, MNRAS, 443, 3538

Hickox, R., Wardlow, J., Smail, I., Myers, A., & Alexander, D. 2012, MNRAS, 421, 284

Hickox, R. C., Jones, C., Forman, W. R., Murray, S. S., Kochanek, C. S., & Eisenstein, D. 2009, ApJ, 696, 891

Hickox, R. C., Mullaney, J. R., Alexander, D. M., Chen, C.-T. J., Civano, F. M., Goulding, A. D., & Hainline, K. N. 2014, ApJ, 782, 9

Hopkins, P., Richards, G., & Hernquist, L. 2007, ApJ, 654, 731

Hopkins, P. F., Hernquist, L., Cox, T. J., & Kereš, D. 2008, ApJS, 175, 356

Hopkins, P. F., Richards, G. T., & Hernquist, L. 2007, ApJ, 654, 731

Hopkins, P. F., Somerville, R. S., Hernquist, L., Cox, T. J., Robertson, B., & Li, Y. 2006, ApJ, 652, 864

Hubble, E., & Humason, M. L. 1931, ApJ, 74, 43

Hunt, A. M. L. K. 2003, ApJL, 589, L21

Ivezić, Ž., Menou, K., Knapp, G. R., Strauss, M. A., Lupton, R. H., Vanden Berk, D. E., Richards, G. T., Tremonti, C., Weinstein, M. A., Anderson, S., Bahcall, N. A., Becker, R. H., Bernardi, M., Blanton, M., Eisenstein, D., Fan, X., Finkbeiner, D., Finlator, K., Frieman, J., Gunn, J. E., Hall, P. B., Kim, R. S. J., Kinkhabwala, A., Narayanan, V. K., Rockosi, C. M., Schlegel, D., Schneider, D. P., Strateva, I., SubbaRao, M., Thakar, A. R., Voges, W., White, R. L., Yanny, B., Brinkmann, J., Doi, M., Fukugita, M., Hennessy, G. S., Munn, J. A., Nichol, R. C., & York, D. G. 2002, AJ, 124, 2364

Ivison, R. J., Smail, I., Papadopoulos, P. P., Wold, I., Richard, J., Swinbank, A. M., Kneib, J.-P., & Owen, F. N. 2010, MNRAS, 404, 198

Iwasawa, K., Sanders, D. B., Teng, S. H., U, V., Armus, L., Evans, A. S., Howell, J. H., Komossa, S., Mazzarella, J. M., Petric, A. O., Surace, J. A., Vavilkin, T., Veilleux, S., & Trentham, N. 2011, A&A, 529, A106

Jahnke, K., & Macciò, A. 2011, ApJ, 734, 92

Jogee, S. 2006, in Lecture Notes in Physics, Berlin Springer Verlag, Vol. 693, Physics of Active Galactic Nuclei at all Scales, ed. D. Alloin, 143

Juneau, S., Dickinson, M., Alexander, D. M., & Salim, S. 2011, ApJ, 736, 104

Juneau, S., Bournaud, F., Charlot, S., Daddi, E., Elbaz, D., Trump, J. R., Brinchmann, J., Dickinson, M., Duc, P.-A., Gobat, R., Jean-Baptiste, I., Le Floc'h, É., Lehnert, M. D., Pacifici, C., Pannella, M., & Schreiber, C. 2014, ApJ, 788, 88

Karim, A., Schinnerer, E., Martínez-Sansigre, A., Sargent, M. T., & van der Wel, A. 2011, ApJ, 730, 61

Kartaltepe, J. S., Dickinson, M., Alexander, D. M., & Bell, E. F. 2012, ApJ, 757, 23

Kartaltepe, J. S., Sanders, D., Floch, E. L., & Frayer, D. 2010, ApJ, 721, 98

Kauffmann, G., & Heckman, T. M. 2009a, MNRAS, 397, 135

—. 2009b, MNRAS, 397, 135

Kauffmann, G., Heckman, T. M., Tremonti, C., Brinchmann, J., & Charlot, S. 2003a,

MNRAS, 346, 1055

—. 2003b, MNRAS, 346, 1055

Keel, W., Chojnowski, D., Bennert, V., & Schawinski, K. 2012a, MNRAS, 420, 878

Keel, W., Lintott, C., & Bennert, K. S. V. 2012b, AJ, 144, 66

Keel, W. C., de Grijp, M. H. K., Miley, G. K., & Zheng, W. 1994, A&A, 283, 791

Kennicutt, Jr., R. C. 1998, ARA&A, 36, 189

Kennicutt, Jr., R. C., Hao, C.-N., Calzetti, D., Moustakas, J., Dale, D. A., Bendo, G., Engelbracht, C. W., Johnson, B. D., & Lee, J. C. 2009, ApJ, 703, 1672

Keres, D., Katz, N., Weinberg, D. H., & Davé, R. 2005, Monthly Notices of the Royal Astronomical Society, 363, 2. +http://dx.doi.org/10.1111/j.1365-2966.2005.09451.x

Kessler, M. F., Steinz, J. A., Anderegg, M. E., Clavel, J., Drechsel, G., Estaria, P., Faelker, J., Riedinger, J. R., Robson, A., Taylor, B. G., & Ximénez de Ferrán, S. 1996, A&A, 315, L27

Kewley, L. J. 2013, ApJ, 774, 100

Kewley, L. J., Dopita, M. A., Sutherland, R. S., Heisler, C. A., & Trevena, J. 2001, ApJ, 556, 121

Kewley, L. J., Geller, M. J., & Barton, E. J. 2006, AJ, 131, 2004

Klesman, A. J., & Sarajedini, V. L. 2012, MNRAS, 425, 1215

Kocevski, D. D., Faber, S. M., Mozena, M., Koekemoer, A. M., & Nandra, K. 2012, ApJ, 744, 148

Koekemoer, A. M., Faber, S. M., Ferguson, H. C., Grogin, N. A., Kocevski, D. D., Koo, D. C., Lai, K., Lotz, J. M., Lucas, R. A., McGrath, E. J., Ogaz, S., Rajan, A., Riess, A. G., Rodney, S. A., Strolger, L., Casertano, S., Castellano, M., Dahlen, T., Dickinson, M., Dolch, T., Fontana, A., Giavalisco, M., Grazian, A., Guo, Y., Hathi, N. P., Huang, K.-H., van der Wel, A., Yan, H.-J., Acquaviva, V., Alexander, D. M., Almaini, O., Ashby, M. L. N., Barden, M., Bell, E. F., Bournaud, F., Brown, T. M., Caputi, K. I., Cassata, P., Challis, P. J., Chary, R.-R., Cheung, E., Cirasuolo, M., Conselice, C. J., Roshan Cooray, A., Croton, D. J., Daddi, E., Davé, R., de Mello, D. F., & de Ravel, L.

2011, ApJS, 197, 36

Kormendy, J., Bender, R., & Cornell, M. 2011, Nature, 469, 374

Kormendy, J., & Richstone, D. 1995, ARA&A, 33, 581

Kriek, M., van Dokkum, P. G., Labbé, I., Franx, M., Illingworth, G. D., Marchesini, D., & Quadri, R. F. 2009, ApJ, 700, 221

Kriek, M., Shapley, A. E., Reddy, N. A., Siana, B., Coil, A. L., Mobasher, B., Freeman, W. R., de Groot, L., Price, S. H., Sanders, R., Shivaei, I., Brammer, G. B., Momcheva, I. G., Skelton, R. E., van Dokkum, P. G., Whitaker, K. E., Aird, J., Azadi, M., Kassis, M., Bullock, J. S., Conroy, C., Davé, R., Kereš, D., & Krumholz, M. 2015, ApJS, 218, 15

Lacy, M., Storrie-Lombardi, L. J., Sajina, A., Appleton, P. N., Armus, L., Chapman, S. C., Choi, P. I., Fadda, D., Fang, F., Frayer, D. T., Heinrichsen, I., Helou, G., Im, M., Marleau, F. R., Masci, F., Shupe, D. L., Soifer, B. T., Surace, J., Teplitz, H. I., Wilson, G., & Yan, L. 2004, ApJS, 154, 166

Laird, E., Nandra, K., Georgakakis, A., & Aird, J. 2009, ApJS, 180, 102

Laird, E. S., Nandra, K., Georgakakis, A., Aird, J. A., Barmby, P., Conselice, C. J., Coil, A. L., Davis, M., Faber, S. M., Fazio, G. G., Guhathakurta, P., Koo, D. C., Sarajedini, V., & Willmer, C. N. A. 2009, ApJS, 180, 102

LaMassa, S. M., Heckman, T. M., Ptak, A., Martins, L., Wild, V., & Sonnentrucker, P. 2010, ApJ, 720, 786

LaMassa, S. M., Heckman, T. M., Ptak, A., & Urry, C. M. 2013, ApJ, 765, L33

Lanzuisi, G., Ranalli, P., Georgantopoulos, I., Georgakakis, A., Delvecchio, I., Akylas, T., Berta, S., Bongiorno, A., Brusa, M., Cappelluti, N., Civano, F., Comastri, A., Gilli, R., Gruppioni, C., Hasinger, G., Iwasawa, K., Koekemoer, A., Lusso, E., Marchesi, S., Mainieri, V., Merloni, A., Mignoli, M., Piconcelli, E., Pozzi, F., Rosario, D. J., Salvato, M., Silverman, J., Trakhtenbrot, B., Vignali, C., & Zamorani, G. 2015, A&A, 573, A137

Lehmer, B. D., Brandt, W. N., Alexander, D., & Bauer, F. E. 2005, ApJS, 161, 21

Leung, G. C. K., Coil, A., Azadi, M., Aird, J., Shapley, A., Kriek, M., Mobasher, B., Reddy, N., Siana, B., Freeman, W., Price, S., Sanders, R., & Shivaei, I. 2017, ArXiv

e-prints, arXiv:1703.10255

Linde, A. D. 1982, Physics Letters B, 108, 389

Luo, B., Bauer, F. E., Brandt, W. N., & Alexander, D. 2008, ApJS, 179, 19

Lusso, E., Comastri, A., Simmons, B. D., Mignoli, M., Zamorani, G., Vignali, C., Brusa, M., Shankar, F., Lutz, D., Trump, J. R., Maiolino, R., Gilli, R., Bolzonella, M., Puccetti, S., Salvato, M., Impey, C. D., Civano, F., Elvis, M., Mainieri, V., Silverman, J. D., Koekemoer, A. M., Bongiorno, A., Merloni, A., Berta, S., Le Floc'h, E., Magnelli, B., Pozzi, F., & Riguccini, L. 2012, MNRAS, 425, 623

Lutz, D., Poglitsch, A., Altieri, B., Andreani, P., Aussel, H., Berta, S., Bongiovanni, A., Brisbin, D., Cava, A., Cepa, J., Cimatti, A., Daddi, E., Dominguez-Sanchez, H., Elbaz, D., Förster Schreiber, N. M., Genzel, R., Grazian, A., Gruppioni, C., Harwit, M., Le Floc'h, E., Magdis, G., Magnelli, B., Maiolino, R., Nordon, R., Pérez García, A. M., Popesso, P., Pozzi, F., Riguccini, L., Rodighiero, G., Saintonge, A., Sanchez Portal, M., Santini, P., Shao, L., Sturm, E., Tacconi, L. J., Valtchanov, I., Wetzstein, M., & Wieprecht, E. 2011, A&A, 532, A90

Magnelli, B., Popesso, P., Berta, S., Pozzi, F., Elbaz, D., Lutz, D., Dickinson, M., Altieri, B., Andreani, P., Aussel, H., Béthermin, M., Bongiovanni, A., Cepa, J., Charmandaris, V., Chary, R.-R., Cimatti, A., Daddi, E., Förster Schreiber, N. M., Genzel, R., Gruppioni, C., Harwit, M., Hwang, H. S., Ivison, R. J., Magdis, G., Maiolino, R., Murphy, E., Nordon, R., Pannella, M., Pérez García, A., Poglitsch, A., Rosario, D., Sanchez-Portal, M., Santini, P., Scott, D., Sturm, E., Tacconi, L. J., & Valtchanov, I. 2013, A&A, 553, A132

Magorrian, J., Tremaine, S., Richstone, D., Bender, R., Bower, G., Dressler, A., Faber, S., Gebhardt, K., Green, R., & Grillmair, C. 1998, AJ, 115, 2285

Marcillac, D., Elbaz, D., Chary, R. R., Dickinson, M., Galliano, F., & Morrison, G. 2006, A&A, 451, 57

Markwardt, C. B. 2009, arXiv preprint arXiv:0902.2850

Masters, D., McCarthy, P., Siana, B., Malkan, M., Mobasher, B., Atek, H., Henry, A., Martin, C. L., Rafelski, M., Hathi, N. P., Scarlata, C., Ross, N. R., Bunker, A. J., Blanc, G., Bedregal, A. G., Domínguez, A., Colbert, J., Teplitz, H., & Dressler, A. 2014, ApJ, 785, 153

Mateos, S., Alonso-Herrero, A., Carrera, F. J., Blain, A., Watson, M. G., Barcons, X.,

Braito, V., Severgnini, P., Donley, J. L., & Stern, D. 2012, MNRAS, 426, 3271

McLean, I. S., Steidel, C. C., Epps, H. W., Konidaris, N., Matthews, K. Y., Adkins, S., Aliado, T., Brims, G., Canfield, J. M., Cromer, J. L., Fucik, J., Kulas, K., Mace, G., Magnone, K., Rodriguez, H., Rudie, G., Trainor, R., Wang, E., Weber, B., & Weiss, J. 2012, 8446, 84460J

Mehta, V., Scarlata, C., Colbert, J. W., Dai, Y. S., Dressler, A., Henry, A., Malkan, M., Rafelski, M., Siana, B., Teplitz, H. I., Bagley, M., Beck, M., Ross, N. R., Rutkowski, M., & Wang, Y. 2015, ApJ, 811, 141

Meléndez, M., Heckman, T., Martínez-Paredes, M., Kraemer, S., & Mendoza, C. 2014, MNRAS, 443, 1358

Mendez, A. J., Coil, A. L., Aird, J., Diamond-Stanic, A. M., & Moustakas, J. 2013, ApJ, 770, 40

Mendez, A. J., Coil, A. L., Lotz, J., Salim, S., Moustakas, J., & Simard, L. 2011, ApJ, 736, 110

Messias, H., Afonso, J., Salvato, M., Mobasher, B., & Hopkins, A. M. 2012, ApJ, 754, 120

Miyaji, T., Hasinger, G., & Schmidt, M. 2001, A&A, 369, 49

Moran, E. C., Filippenko, A. V., Ho, L. C., Shields, J. C., Belloni, T., Comastri, A., Snowden, S. L., & Sramek, R. A. 1999, PASP, 111, 801

Moustakas, J., Coil, A. L., Aird, J., Blanton, M. R., & Cool, R. J. 2013, ApJ, 767, 50

Mullaney, J. R., Daddi, E., Béthermin, M., & Elbaz, D. 2012a, ApJL, 753, L30

Mullaney, J. R., Pannella, M., Daddi, E., Alexander, D., Elbaz, D., & Hickox, R. C. 2012b, MNRAS, 419, 95

Mullaney, J. R., Alexander, D. M., Aird, J., Bernhard, E., Daddi, E., Del Moro, A., Dickinson, M., Elbaz, D., Harrison, C. M., Juneau, S., Liu, D., Pannella, M., Rosario, D., Santini, P., Sargent, M., Schreiber, C., Simpson, J., & Stanley, F. 2015, MNRAS, 453, L83

Muzzin, A., van Dokkum, P., Kriek, M., Labbé, I., Cury, I., Marchesini, D., & Franx, M. 2010, ApJ, 725, 742

Muzzin, A., Marchesini, D., Stefanon, M., Franx, M., McCracken, H. J., Milvang-Jensen, B., Dunlop, J. S., Fynbo, J. P. U., Brammer, G., Labbé, I., & van Dokkum, P. G. 2013, ApJ, 777, 18

Nandra, K., Georgakakis, A., Willmer, C., & Cooper, M. 2007, ApJL, 660, L11

Nandra, K., Laird, E. S., Aird, J. A., Salvato, M., Georgakakis, A., Barro, G., Perez-Gonzalez, P. G., Barmby, P., Chary, R.-R., Coil, A., Cooper, M. C., Davis, M., Dickinson, M., Faber, S. M., Fazio, G. G., Guhathakurta, P., Gwyn, S., Hsu, L.-T., Huang, J.-S., Ivison, R. J., Koo, D. C., Newman, J. A., Rangel, C., Yamada, T., & Willmer, C. 2015, ApJS, 220, 10

Netzer, H. 1990, in Active Galactic Nuclei, ed. R. D. Blandford, H. Netzer, L. Woltjer, T. J.-L. Courvoisier, & M. Mayor, 57–160

Netzer, H. 2009, MNRAS, 399, 1907

Netzer, H., Mor, R., Trakhtenbrot, B., Shemmer, O., & Lira, P. 2013, ArXiv e-prints, arXiv:1308.0012

Neugebauer, G., Oke, J. B., Becklin, E. E., & Matthews, K. 1979, ApJ, 230, 79

Neugebauer, G., Habing, H. J., van Duinen, R., Aumann, H. H., Baud, B., Beichman, C. A., Beintema, D. A., Boggess, N., Clegg, P. E., de Jong, T., Emerson, J. P., Gautier, T. N., Gillett, F. C., Harris, S., Hauser, M. G., Houck, J. R., Jennings, R. E., Low, F. J., Marsden, P. L., Miley, G., Olnon, F. M., Pottasch, S. R., Raimond, E., Rowan-Robinson, M., Soifer, B. T., Walker, R. G., Wesselius, P. R., & Young, E. 1984, ApJ, 278, L1

Newman, J. A., Cooper, M. C., Davis, M., Faber, S. M., Coil, A. L., Guhathakurta, P., Koo, D. C., Phillips, A. C., Conroy, C., Dutton, A. A., Finkbeiner, D. P., Gerke, B. F., Rosario, D. J., Weiner, B. J., Willmer, C. N. A., Yan, R., Harker, J. J., Kassin, S. A., Konidaris, N. P., Lai, K., Madgwick, D. S., Noeske, K. G., Wirth, G. D., Connolly, A. J., Kaiser, N., Kirby, E. N., Lemaux, B. C., Lin, L., Lotz, J. M., Luppino, G. A., Marinoni, C., Matthews, D. J., Metevier, A., & Schiavon, R. P. 2013, ApJS, 208, 5

Newman, S. F. 2014, ApJ, 781, 21

Noeske, K. G., Weiner, B. J., Faber, S. M., & Papovich, C. 2007a, ApJL, 660, L43

—. 2007b, ApJL, 660, L43

Nordon, R., Lutz, D., Shao, L., Magnelli, B., Berta, S., Altieri, B., Andreani, P., Aussel, H., Bongiovanni, A., Cava, A., Cepa, J., Cimatti, A., Daddi, E., Dominguez, H., Elbaz, D., Förster Schreiber, N. M., Genzel, R., Grazian, A., Magdis, G., Maiolino, R., Pérez García, A. M., Poglitsch, A., Popesso, P., Pozzi, F., Riguccini, L., Rodighiero, G., Saintonge, A., Sanchez-Portal, M., Santini, P., Sturm, E., Tacconi, L., Valtchanov, I., Wetzstein, M., & Wieprecht, E. 2010, A&A, 518, L24

Nordon, R., Lutz, D., Genzel, R., Berta, S., Wuyts, S., Magnelli, B., Altieri, B., Andreani, P., Aussel, H., Bongiovanni, A., Cepa, J., Cimatti, A., Daddi, E., Fadda, D., Förster Schreiber, N. M., Lagache, G., Maiolino, R., Pérez García, A. M., Poglitsch, A., Popesso, P., Pozzi, F., Rodighiero, G., Rosario, D., Saintonge, A., Sanchez-Portal, M., Santini, P., Sturm, E., Tacconi, L. J., Valtchanov, I., & Yan, L. 2012, ApJ, 745, 182

Osterbrock, D. E. 1989, Astrophysics of gaseous nebulae and active galactic nuclei

Pagani, C., Falomo, R., & Treves, A. 2003, ApJ, 596, 830

Page, M. J., Symeonidis, M., Vieira, J. D., & Altieri, B. 2012, Nature, 485, 213

Papovich, C., Rudnick, G., Le Floc'h, E., van Dokkum, P. G., Rieke, G. H., Taylor, E. N., Armus, L., Gawiser, E., Huang, J., Marcillac, D., & Franx, M. 2007, ApJ, 668, 45

Peng, C. 2007, ApJ, 671, 1098

Peterson, B. M. 2001, 3

Pierre, M., Chiappetti, L., Pacaud, F., & Gueguen, A. 2007, MNRAS, 382, 279

Pilbratt, G. L., Riedinger, J. R., Passvogel, T., Crone, G., Doyle, D., Gageur, U., Heras, A. M., Jewell, C., Metcalfe, L., Ott, S., & Schmidt, M. 2010, A&A, 518, L1

Planck Collaboration, Ade, P. A. R., Aghanim, N., Armitage-Caplan, C., Arnaud, M., Ashdown, M., Atrio-Barandela, F., Aumont, J., Baccigalupi, C., Banday, A. J., & et al. 2014, A&A, 571, A16

Pope, A., Chary, R.-R., Alexander, D. M., Armus, L., Dickinson, M., Elbaz, D., Frayer, D., Scott, D., & Teplitz, H. 2008, ApJ, 675, 1171

Puccetti, S., Fiore, F., D'Elia, V., Pillitteri, I., Feruglio, C., Grazian, A., Brusa, M., Ciliegi, P., Comastri, A., Gruppioni, C., Mignoli, M., Vignali, C., Zamorani, G., La Franca, F., Sacchi, N., Franceschini, A., Berta, S., Buttery, H., & Dias, J. E. 2006, A&A, 457, 501

Ranalli, P., Comastri, A., & Setti, G. 2003, A&A, 399, 39

Rangel, C., Nandra, K., Laird, E. S., & Orange, P. 2013, MNRAS, 428, 3089

Reddy, N., Dickinson, M., Elbaz, D., Morrison, G., Giavalisco, M., Ivison, R., Papovich, C., Scott, D., Buat, V., Burgarella, D., Charmandaris, V., Daddi, E., Magdis, G., Murphy, E., Altieri, B., Aussel, H., Dannerbauer, H., Dasyra, K., Hwang, H. S., Kartaltepe, J., Leiton, R., Magnelli, B., & Popesso, P. 2012, ApJ, 744, 154

Reddy, N. A., Erb, D. K., Pettini, M., Steidel, C. C., & Shapley, A. E. 2010, ApJ, 712, 1070

Reddy, N. A., Kriek, M., Shapley, A. E., Freeman, W. R., Siana, B., Coil, A. L., Mobasher, B., Price, S. H., Sanders, R. L., & Shivaei, I. 2015, ApJ, 806, 259

Rees, M. J., & Ostriker, J. P. 1977, MNRAS, 179, 541

Reines, A. E., Greene, J. E., & Geha, M. 2013, ApJ, 775, 116

Reines, A. E., Sivakoff, G. R., Johnson, K. E., & Brogan, C. L. 2011, Nature, 470, 66

Richards, G. T., Lacy, M., Storrie-Lombardi, L. J., Hall, P. B., Gallagher, S. C., Hines, D. C., Fan, X., Papovich, C., Vanden Berk, D. E., Trammell, G. B., Schneider, D. P., Vestergaard, M., York, D. G., Jester, S., Anderson, S. F., Budavári, T., & Szalay, A. S. 2006, ApJS, 166, 470

Rieke, G. H., Alonso-Herrero, A., Weiner, B. J., Pérez-González, P. G., Blaylock, M., Donley, J. L., & Marcillac, D. 2009, ApJ, 692, 556

Rieke, G. H., & Lebofsky, M. J. 1981, ApJ, 250, 87

Rieke, G. H., Young, E. T., Engelbracht, C. W., Kelly, D. M., Low, F. J., Haller, E. E., Beeman, J. W., Gordon, K. D., Stansberry, J. A., Misselt, K. A., Cadien, J., Morrison, J. E., Rivlis, G., Latter, W. B., Noriega-Crespo, A., Padgett, D. L., Stapelfeldt, K. R., Hines, D. C., Egami, E., Muzerolle, J., Alonso-Herrero, A., Blaylock, M., Dole, H., Hinz, J. L., Le Floc'h, E., Papovich, C., Pérez-González, P. G., Smith, P. S., Su, K. Y. L., Bennett, L., Frayer, D. T., Henderson, D., Lu, N., Masci, F., Pesenson, M., Rebull, L., Rho, J., Keene, J., Stolovy, S., Wachter, S., Wheaton, W., Werner, M. W., & Richards, P. L. 2004, ApJS, 154, 25

Rosario, D. J., Santini, P., Lutz, D., Shao, L., Maiolino, R., Alexander, D. M., Altieri, B., Andreani, P., Aussel, H., Bauer, F. E., Berta, S., Bongiovanni, A., Brandt, W. N.,

Brusa, M., Cepa, J., Cimatti, A., Cox, T. J., Daddi, E., Elbaz, D., Fontana, A., Förster Schreiber, N. M., Genzel, R., Grazian, A., Le Floch, E., Magnelli, B., Mainieri, V., Netzer, H., Nordon, R., Pérez Garcia, I., Poglitsch, A., Popesso, P., Pozzi, F., Riguccini, L., Rodighiero, G., Salvato, M., Sanchez-Portal, M., Sturm, E., Tacconi, L. J., Valtchanov, I., & Wuyts, S. 2012, A&A, 545, A45

Rosario, D. J., Santini, P., Lutz, D., Netzer, H., Bauer, F. E., Berta, S., Magnelli, B., Popesso, P., Alexander, D. M., Brandt, W. N., Genzel, R., Maiolino, R., Mullaney, J. R., Nordon, R., Saintonge, A., Tacconi, L., & Wuyts, S. 2013, ApJ, 771, 63

Rosario, D. J., McIntosh, D. H., van der Wel, A., Kartaltepe, J., Lang, P., Santini, P., Wuyts, S., Lutz, D., Rafelski, M., Villforth, C., Alexander, D. M., Bauer, F. E., Bell, E. F., Berta, S., Brandt, W. N., Conselice, C. J., Dekel, A., Faber, S. M., Ferguson, H. C., Genzel, R., Grogin, N. A., Kocevski, D. D., Koekemoer, A. M., Koo, D. C., Lotz, J. M., Magnelli, B., Maiolino, R., Mozena, M., Mullaney, J. R., Papovich, C. J., Popesso, P., Tacconi, L. J., Trump, J. R., Avadhuta, S., Bassett, R., Bell, A., Bernyk, M., Bournaud, F., Cassata, P., Cheung, E., Croton, D., Donley, J., DeGroot, L., Guedes, J., Hathi, N., Herrington, J., Hilton, M., Lai, K., Lani, C., Martig, M., McGrath, E., Mutch, S., Mortlock, A., McPartland, C., O'Leary, E., Peth, M., Pillepich, A., Poole, G., Snyder, D., Straughn, A., Telford, O., Tonini, C., & Wandro, P. 2015, A&A, 573, A85

Rovilos, E., Comastri, A., Gilli, R., Georgantopoulos, I., Ranalli, P., Vignali, C., Lusso, E., Cappelluti, N., Zamorani, G., Elbaz, D., Dickinson, M., Hwang, H. S., Charmandaris, V., Ivison, R. J., Merloni, A., Daddi, E., Carrera, F. J., Brandt, W. N., Mullaney, J. R., Scott, D., Alexander, D. M., Del Moro, A., Morrison, G., Murphy, E. J., Altieri, B., Aussel, H., Dannerbauer, H., Kartaltepe, J., Leiton, R., Magdis, G., Magnelli, B., Popesso, P., & Valtchanov, I. 2012, A&A, 546, A58

Salim, S., Dickinson, M., Michael Rich, R., Charlot, S., Lee, J. C., Schiminovich, D., Pérez-González, P. G., Ashby, M. L. N., Papovich, C., Faber, S. M., Ivison, R. J., Frayer, D. T., Walton, J. M., Weiner, B. J., Chary, R.-R., Bundy, K., Noeske, K., & Koekemoer, A. M. 2009, ApJ, 700, 161

Salpeter, E. E. 1955, ApJ, 121, 161

Sanders, D. B., Mazzarella, J. M., Kim, D.-C., Surace, J. A., & Soifer, B. T. 2003, AJ, 126, 1607

Sanders, D. B., & Mirabel, I. F. 1996, ARA&A, 34, 749

Sanders, R. L., Shapley, A. E., Kriek, M., Reddy, N. A., Freeman, W. R., Coil, A. L.,

Siana, B., Mobasher, B., Shivaei, I., Price, S. H., & de Groot, L. 2016, ApJ, 816, 23

Santini, P., Rosario, D. J., Shao, L., Lutz, D., Maiolino, R., Alexander, D. M., Altieri, B., Andreani, P., Aussel, H., Bauer, F. E., Berta, S., Bongiovanni, A., Brandt, W. N., Brusa, M., Cepa, J., Cimatti, A., Daddi, E., Elbaz, D., Fontana, A., Förster Schreiber, N. M., Genzel, R., Grazian, A., Le Floc'h, E., Magnelli, B., Mainieri, V., Nordon, R., Pérez Garcia, A. M., Poglitsch, A., Popesso, P., Pozzi, F., Riguccini, L., Rodighiero, G., Salvato, M., Sanchez-Portal, M., Sturm, E., Tacconi, L. J., Valtchanov, I., & Wuyts, S. 2012, A&A, 540, A109

Sartori, L. F., Schawinski, K., Treister, E., Trakhtenbrot, B., Koss, M., Shirazi, M., & Oh, K. 2015, MNRAS, 454, 3722

Schade, D. J., Boyle, B. J., & Letawsky, M. 2000, MNRAS, 315, 498

Schawinski, K., Simmons, B. D., Urry, C. M., Treister, E., & Glikman, E. 2012, MNRAS, 425, L61

Schawinski, K., Treister, E., Urry, C. M., Cardamone, C. N., Simmons, B., & Sukyoung, K. Y. 2011, ApJL, 727, L31

Schawinski, K., Urry, M., Virani, S., & Coppi, P. 2010, ApJ, 711, 284

Secrest, N. J., Satyapal, S., Gliozzi, M., Rothberg, B., Ellison, S. L., Mowry, W. S., Rosenberg, J. L., Fischer, J., & Schmitt, H. 2015, ApJ, 798, 38

Seyfert. 1943, ApJ, 97, 28

Shapley, A. E., Reddy, N. A., Kriek, M., Freeman, W. R., Sanders, R. L., Siana, B., Coil, A. L., Mobasher, B., Shivaei, I., Price, S. H., & de Groot, L. 2015, ApJ, 801, 88

Sharples, R., Bender, R., Agudo Berbel, A., Bezawada, N., Castillo, R., Cirasuolo, M., Davidson, G., Davies, R., Dubbeldam, M., Fairley, A., Finger, G., Förster Schreiber, N., Gonte, F., Hess, A., Jung, I., Lewis, I., Lizon, J.-L., Muschielok, B., Pasquini, L., Pirard, J., Popovic, D., Ramsay, S., Rees, P., Richter, J., Riquelme, M., Rodrigues, M., Saviane, I., Schlichter, J., Schmidtobreick, L., Segovia, A., Smette, A., Szeifert, T., van Kesteren, A., Wegner, M., & Wiezorrek, E. 2013, The Messenger, 151, 21

Shi, Y., Rieke, G., Lotz, J., & Perez-Gonzalez, P. G. 2009, ApJ, 697, 1764

Shivaei, I., Reddy, N. A., Shapley, A. E., Kriek, M., Siana, B., Mobasher, B., Coil, A. L., Freeman, W. R., Sanders, R., Price, S. H., de Groot, L., & Azadi, M. 2015, ApJ, 815,

98

Shivaei, I., Reddy, N. A., Shapley, A. E., Siana, B., Kriek, M., Mobasher, B., Coil, A. L., Freeman, W. R., Sanders, R. L., Price, S. H., Azadi, M., & Zick, T. 2017, ApJ, 837, 157

Silverman, J. D., Green, P. J., Barkhouse, W., Kim, D.-W., & Kim, M. 2008, ApJ, 679, 118

Silverman, J. D., Katarina Kovač, K., Knobel, C., Lilly, S. J., & Bolzonella, M. 2009, ApJ, 695, 171

Skelton, R. E., Whitaker, K. E., Momcheva, I. G., Brammer, G. B., van Dokkum, P. G., Labbé, I., Franx, M., van der Wel, A., Bezanson, R., Da Cunha, E., Fumagalli, M., Förster Schreiber, N., Kriek, M., Leja, J., Lundgren, B. F., Magee, D., Marchesini, D., Maseda, M. V., Nelson, E. J., Oesch, P., Pacifici, C., Patel, S. G., Price, S., Rix, H.-W., Tal, T., Wake, D. A., & Wuyts, S. 2014, ApJS, 214, 24

Smith, J. D. T., Draine, B. T., Dale, D. A., Moustakas, J., Kennicutt, Jr., R. C., Helou, G., Armus, L., Roussel, H., Sheth, K., Bendo, G. J., Buckalew, B. A., Calzetti, D., Engelbracht, C. W., Gordon, K. D., Hollenbach, D. J., Li, A., Malhotra, S., Murphy, E. J., & Walter, F. 2007, ApJ, 656, 770

Somerville, R. S., Hopkins, P. F., Cox, T. J., Robertson, B. E., & Hernquist, L. 2008, MNRAS, 391, 481

Stanley, F., Harrison, C. M., Alexander, D. M., Swinbank, A. M., Aird, J. A., Del Moro, A., Hickox, R. C., & Mullaney, J. R. 2015, MNRAS, 453, 591

Steidel, C. C., Rudie, G. C., Strom, A. L., Pettini, M., Reddy, N. A., Shapley, A. E., Trainor, R. F., Erb, D. K., Turner, M. L., Konidaris, N. P., Kulas, K. R., Mace, G., Matthews, K., & McLean, I. S. 2014, ApJ, 795, 165

Stern, D., Eisenhardt, P., Gorjian, V., Kochanek, C. S., Caldwell, N., Eisenstein, D., Brodwin, M., Brown, M. J. I., Cool, R., Dey, A., Green, P., Jannuzi, B. T., Murray, S. S., Pahre, M. A., & Willner, S. P. 2005, ApJ, 631, 163

Stott, J. P., Hickox, R. C., Edge, A. C., Collins, C. A., Hilton, M., Harrison, C. D., & Romer, A. K. 2012, MNRAS, 422, 2213

Sutherland, W., & Saunders, W. 1992a, MNRAS, 259, 413

—. 1992b, MNRAS, 259, 413

Symeonidis, M., Georgakakis, A., Seymour, N., Auld, R., & Bock, J. 2011a, MNRAS, 417, 2239

Symeonidis, M., Page, M. J., & Seymour, N. 2011b, Monthly Notices of the Royal Astronomical Society, 411, 983. +http://dx.doi.org/10.1111/j.1365-2966.2010.17735.x

Tanaka, M. 2012, PASJ, 64, arXiv:1111.0132

Treister, E., Schawinski, K., Urry, C. M., & Simmons, B. D. 2012, ApJ, 758, L39

Trouille, L., & Barger, A. J. 2010, ApJ, 722, 212

Trump, J. R., Konidaris, N. P., Barro, G., Koo, D. C., Kocevski, D. D., Juneau, S., Weiner, B. J., Faber, S. M., McLean, I. S., Yan, R., Pérez-González, P. G., & Villar, V. 2013, ApJ, 763, L6

Trump, J. R., Sun, M., Zeimann, G. R., Luck, C., Bridge, J. S., Grier, C. J., Hagen, A., Juneau, S., Montero-Dorta, A., Rosario, D. J., Brandt, W. N., Ciardullo, R., & Schneider, D. P. 2015, ApJ, 811, 26

Ueda, Y., Watson, M. G., Stewart, I. M., Akiyama, M., & Schwope, A. D. 2008, ApJS, 179, 124

Ulrich, M. H., Maraschi, L., & Urry, M. 1997, ARA&A, 35, 445

Vasudevan, R. V., & Fabian, A. C. 2007, MNRAS, 381, 1235

Veilleux, S., & Osterbrock, D. E. 1987, ApJS, 63, 295

Vignali, C., Alexander, D. M., Gilli, R., & Pozzi, F. 2010, MNRAS, 404, 48

Volonteri, M. 2010, A&A Rv, 18, 279

Werner, M. W., Roellig, T. L., Low, F. J., Rieke, G. H., Rieke, M., Hoffmann, W. F., Young, E., Houck, J. R., Brandl, B., Fazio, G. G., Hora, J. L., Gehrz, R. D., Helou, G., Soifer, B. T., Stauffer, J., Keene, J., Eisenhardt, P., Gallagher, D., Gautier, T. N., Irace, W., Lawrence, C. R., Simmons, L., Van Cleve, J. E., Jura, M., Wright, E. L., & Cruikshank, D. P. 2004, ApJS, 154, 1

Whitaker, K. E., van Dokkum, P. G., Brammer, G., & Franx, M. 2012, ApJ, 754, L29

Whitaker, K. E., Van Dokkum, P. G., Brammer, G., Kriek, M., Franx, M., Labbé, I., Marchesini, D., Quadri, R. F., Bezanson, R., Illingworth, G. D., et al. 2010, The Astrophysical Journal, 719, 1715

Whitaker, K. E., Labbé, I., van Dokkum, P. G., Brammer, G., Kriek, M., Marchesini, D., Quadri, R. F., Franx, M., Muzzin, A., Williams, R. J., Bezanson, R., Illingworth, G. D., Lee, K.-S., Lundgren, B., Nelson, E. J., Rudnick, G., Tal, T., & Wake, D. A. 2011, ApJ, 735, 86

Wild, V., Charlot, S., Brinchmann, J., & Heckman, T. 2011, MNRAS, 417, 1760

Wild, V., Heckman, T., & Charlot, S. 2010, MNRAS, 405, 933

Wilkins, S. M., Hopkins, A. M., Trentham, N., & Tojeiro, R. 2008, MNRAS, 391, 363

Williams, R. J., Quadri, R. F., Franx, M., van Dokkum, P., & Labbé, I. 2009, ApJ, 691, 1879

Williams, R. J., Quadri, R. F., Franx, M., van Dokkum, P., Toft, S., Kriek, M., & Labbé, I. 2010, ApJ, 713, 738

Wong, T. 2009, ApJ, 705, 650

Wright, E. L., Eisenhardt, P. R. M., Mainzer, A. K., Ressler, M. E., Cutri, R. M., Jarrett, T., Kirkpatrick, J. D., Padgett, D., McMillan, R. S., Skrutskie, M., Stanford, S. A., Cohen, M., Walker, R. G., Mather, J. C., Leisawitz, D., Gautier, III, T. N., McLean, I., Benford, D., Lonsdale, C. J., Blain, A., Mendez, B., Irace, W. R., Duval, V., Liu, F., Royer, D., Heinrichsen, I., Howard, J., Shannon, M., Kendall, M., Walsh, A. L., Larsen, M., Cardon, J. G., Schick, S., Schwalm, M., Abid, M., Fabinsky, B., Naes, L., & Tsai, C.-W. 2010, AJ, 140, 1868

Wuyts, S., Labbé, I., Förster Schreiber, N. M., Franx, M., Rudnick, G., Brammer, G. B., & van Dokkum, P. G. 2008, ApJ, 682, 985

Wuyts, S., Förster Schreiber, N. M., Lutz, D., Nordon, R., Berta, S., Altieri, B., Andreani, P., Aussel, H., Bongiovanni, A., Cepa, J., Cimatti, A., Daddi, E., Elbaz, D., Genzel, R., Koekemoer, A. M., Magnelli, B., Maiolino, R., McGrath, E. J., Pérez García, A., Poglitsch, A., Popesso, P., Pozzi, F., Sanchez-Portal, M., Sturm, E., Tacconi, L., & Valtchanov, I. 2011, ApJ, 738, 106

Xue, Y. Q., Brandt, W. N., Luo, B., & Rafferty, D. 2010, ApJ, 720, 368

Yabe, K., Ohta, K., Iwamuro, F., Yuma, S., Akiyama, M., Tamura, N., Kimura, M., Takato, N., Moritani, Y., Sumiyoshi, M., Maihara, T., Silverman, J., Dalton, G., Lewis, I., Bonfield, D., Lee, H., Curtis Lake, E., Macaulay, E., & Clarke, F. 2012, PASJ, 64, 60

York, D. G., Adelman, J., Anderson, Jr., J. E., et al. 2000, AJ, 120, 1579